The Effects of Disruption of Synaptic Signaling on Neuronal Networks

by

Maral Budak

A dissertation submitted in partial fulfillment
of the requirements for the degree of
Doctor of Philosophy
(Biophysics)
in the University of Michigan
2020

Doctoral Committee:

       Professor Victoria Booth, Co-Chair
       Professor Michal Zochowski, Co-Chair
       Professor Gabriel Corfas
       Professor Karl Grosh
       Assistant Professor Kevin Wood
       Assistant Professor Qiong Yang

Maral Budak

mbudak@umich.edu

ORCID iD: 0000-0001-7565-1332

To Gary, for his endless support and love

Acknowledgements

Since my childhood, I have always been dreaming about being a scientist and contributing to human knowledge, as I was always fascinated by science and curious to learn more. However, my main motivation for pursuing science was the urge to help hopeless people, whose problems cannot be solved by current knowledge in medicine. Seeing those people suffer has always been mentally overwhelming to me, especially if they are beloved ones. I noticed how important scientific advancements would be after witnessing that my grandpa couldn't help himself as a medical doctor, and this experience boosted my passion for science. And this passion drove me to take this big step in my life without any hesitation. Even though I needed to leave my family, my friends and my whole life behind, I feel like doing a PhD at the University of Michigan was the best decision I have ever made in my life. I am thankful to all of the people who played a role in fulfilling my dream.

First of all, I couldn't have accomplished this without my co-advisors, Michal Zochowski and Victoria Booth, whom I have learned everything from. I started working with them with no prior knowledge in this field, which scared me many times. Thanks to their courage and support, I overcame my fears and became more self-confident over time. Feeling less and less stupid at our weekly meetings was great evidence to me that I was on the right track. I am grateful to them for teaching me how to be a good scientist, and also for creating a fun and friendly working atmosphere, which is actually almost as important as the research. I am also thankful to our collaborators Gabriel Corfas and Karl Grosh for all the input they provided for the studies on

iii

and the oceans between us couldn't impair our 25-year-old friendship. I would also like to acknowledge the most recent friend I have had, our cat Mosaic, who is the best cat I have ever met. Thank you for being patient with me and still loving me even though I've been treating you as my stress ball for the past few months. Thank you for accompanying me over the sleepless nights and keeping me awake with your meows.

Apart from the academic advantages, moving to Michigan gave me the opportunity to meet my fiancé Gary, and I don't know how to express my gratefulness to him. Thank you for listening to the same talk a thousand times until I was ready, for sometimes taking the problems related to my research even more seriously than I did, for calming me down and encouraging me whenever I felt hopeless. Thank you for being my best friend and the biggest supporter in my life.

Table of Contents

List of Tables

List of Figures

Abstract

The brain is an organ that acts as the conductor of an orchestra – it governs all vital body functions and assures that all organs operate in harmony. Moreover, it plays a crucial role in various tasks such as memory formation, sensory processing and movement control. The performance of the brain in these tasks requires spatiotemporal patterns formed by the activity of different parts of the brain. The formation of the spatiotemporal patterns in the brain is facilitated by the connections between neurons, also known as synapses. Therefore, transmission failure in synapses may lead to disruption in these patterns and may impair the proper functioning of the brain. The aim of this dissertation is to explore the outcomes when synaptic transmission is disrupted. First, we investigated the universal effect of synaptic failure in neuronal networks having heterogeneous connectivity. Even though human studies on anesthetics claimed that failure in signal transmission in the brain results in loss of coherence in brain activity, we provided evidence that this may not always be true. On the contrary, synaptic failure may facilitate the emergence of coherent neuronal network activity due to more balanced input levels across the neuronal network.

The second part of this dissertation focuses on a specific case which arises from disruption in synaptic signaling in the peripheral auditory system, namely hidden hearing loss (HHL). We built a computational model to simulate two mechanisms that give rise to HHL: 1) loss of synapses between inner hair cells (IHCs) and spiral ganglion neurons (SGNs) and 2) myelin defects at the peripheral SGN axons. We concluded that both mechanisms decrease the cumulative SGN activity,

whereas only myelin defects desynchronize it, confirming the experimental observations. Finally, we investigated the effect of SGN myelin defects on sound localization, as patients with HHL were shown to have binaural processing deficits. We provided evidence that the activity of the neurons in the downstream cochlear nucleus circuit that is responsible for sound localization is severely impaired as a result of myelin defects in SGN fibers. This result possibly elucidates the mechanism that gives rise to sound localization deficiencies in HHL patients.

Chapter I

Introduction

The brain is one of the most important organs of the human body where vital life functions are controlled and all emotions, senses, thoughts and memories are formed. It performs a diverse set of tasks owing to its ability to execute extensive computations, which is crucial for processing and transmitting sensory information. How these tasks are performed by the brain still needs to be largely discovered, and many studies focus on understanding the brain's mechanisms from various perspectives. So far, the interplay between experimental studies, computational modeling and data analysis methods has been very powerful in shedding light on the events underlying the brain's function.

The basic unit of the brain is the neuron. The neuron itself is a rather simple computational unit as it, in simplest terms, receives inputs from other cells, and based on its (often complex and nonlinear) processing emits a binary signal itself – an action potential. Neurons are connected by synapses, forming a complex neuronal network structure within the brain. The communication between neurons is primarily maintained by synapses, which play a crucial role in the functioning of the brain. Due to the complex connectivity in the brain, the neurons from its separate modalities are able to cross-talk, and various spatiotemporal patterns of neuronal activity emerge. Therefore, proper synaptic transmission is necessary to maintain the formation of these patterns, which are required to maintain the performance of the brain. Humans, in particular, with

the highest number of synapses ($\sim 10^{14}$) across all animals, owe their higher intelligence and ability to perform many complex tasks to these spatiotemporal patterns. Thus, the disruption of synaptic transmission critically impairs information processing in the brain and may underlie many neurodegenerative diseases. This work is aimed at understanding, in a universal case, effects of disruption of synaptic signaling on neuronal network activity, and, in a specific case, how this disruption contributes to hidden hearing loss.

1.1 Neurons: main signaling units in the nervous system

Neurons are the basic units of the nervous system, where information processing occurs via extensive computations. Even though there are morphologically distinct types of neurons, they typically consist of a cell body, an axon, dendrites and presynaptic terminals. Incoming signals from other neurons are received by the dendritic branches that are connected to the cell body, where all signals integrate. The integrated signal is then conveyed via the axon to the presynaptic terminals and is transmitted to other neurons via synapses.

1.1.1 Basic physical mechanisms underlying function of individual neurons

A potential difference is maintained between the inside and outside of neurons due to properties of their lipid bilayer membrane which restricts the flow of ions into and out of the cell. The capacitance property of the membrane stems from this ability to separate charges, where the lipid bilayer acts as an insulator that enables the storage of charge on its opposite sides. However, the membrane includes voltage-gated ion channels selectively permeable to different types of ions. These ion channels can switch between open and closed states, and the rate of transition between these states depends on the membrane potential due to the voltage sensitivity of ion channels. The ability of neural membrane to regulate the flow of ions via these channels represents its

conductance property. Additionally, due to the separation of ionic charges, there is a concentration gradient for each ion across the membrane. The standard way to model a neuron represents a patch of neural membrane as an equivalent electrical circuit consisting of a capacitor, conductors for each type of ion channel and batteries for each type of ion gradient (Figure I.1).
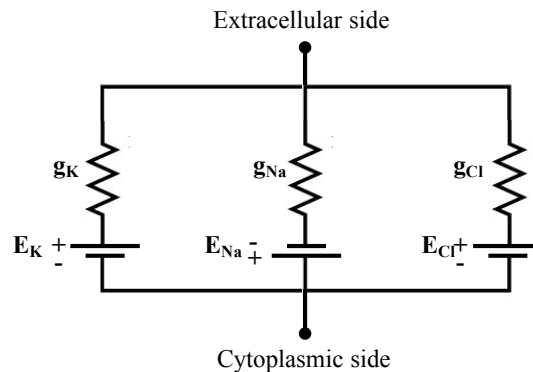
Figure I.1 The equivalent circuit of the membrane of a neuron.

In the neuron's resting state, Na^+ and Cl^- ions are more concentrated in the extracellular space outside of the membrane, whereas K^+ and organic anions are more concentrated inside the cell. The maintenance of the concentration gradients of these ions is facilitated by Na^+-K^+ pumps, which balance out the passive movement of these ions by transporting them against their concentration gradients, i.e. they pump Na^+ outside of the cell and K^+ inside of the cell with the usage of ATP. In an equilibrium state, the potential difference between the inside and the outside of the membrane, also known as the resting potential, is around -65mV.

1.1.2 Generation of action potentials

Action potentials are fast and transient electrical signals generated by neurons in response to input signals received from their presynaptic connections. They are sources of information conveyed to and processed by the brain. The generation of action potentials requires the input signal to cause membrane voltage to exceed a certain threshold value. Once the membrane

3

potential of a neuron reaches the threshold, the amplitude and the duration of the resulting action potential is the same independent from the strength of the received signal. This phenomenon of the neurons is called the 'all-or-none law', and it stems from the nonlinear, voltage dependent dynamics of the ion channels. The rate of the transition between open and closed states of these channels depends on the membrane potential. At the resting state, voltage-gated Na^+ and K^+ channels are in a closed state. The transient increase in the membrane potential, also called depolarization, due to the received signals opens Na^+ channels, which results in the influx of the Na^+ ions down their concentration gradients. If the membrane potential reaches the threshold voltage, a large Na^+ influx depolarizes the neuron rapidly, generating an action potential. Due to the high membrane potential as a result of this influx, Na^+ channels close and consecutively K^+ channels open, resulting in the outflow of the K^+ ions and a sharp decrease of the membrane potential. The rapid increase followed by a sharp decrease in the membrane potential is called an action potential or spike.

1.1.3 Propagation of action potential down the axon

Neuronal processes, like axons or dendrites, transmit voltage signals received from presynaptic connections for significant distances through the interior of their membranes. The processes underlying this propagation, especially in case of myelinated axons can be quite complex. To be able to model how signals propagate along the axon and dendrites, it's been assumed that axons or dendrites are cylindrical membranes, or 'cables' in which electrical conduction takes place [1]. To calculate how the voltage changes along the cable, it is commonly discretized into sub-cylinders with infinitesimal lengths. The voltage needs to be calculated at each discrete region, which can be considered as a point neuron with a capacitance (c_m) and a resistance (r_m) connected in parallel, as described in Section 1.1.1. Each compartment is connected through

the cytoplasm and the extracellular fluid. Due to the intrinsic resistive properties of the cytoplasm, the current flowing between compartments through the cytoplasm encounters a resistance, called an axial resistance (r_a). However, the distinct regions are also connected with a short circuit representing the extracellular fluid, since the potential difference outside of the membrane is assumed to be the same everywhere (Figure I.2). By using Ohm's Law and Kirchhoff's Law, the following equation can be derived to represent the membrane potential as a function of space x and time t:

$$-\frac{1}{r_a}\frac{\partial^2 V_m(x,t)}{\partial x^2} + c_m \frac{\partial V_m(x,t)}{\partial t} + \frac{V_m(x,t)-E_{rest}}{r_m} = I_{app}(x,t). \tag{1.1}$$

Here, E_{rest} is the resting membrane potential and I_{app} is the current generated by the received signal.
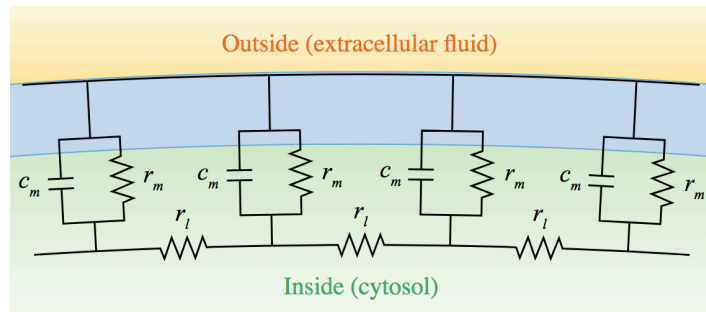
Figure I.2 The equivalent circuit of a neuronal process.

The ability of the membrane to resist the flow of the ions is determined by the membrane resistance, which can be expressed as

$$r_m = R_m/2\pi a, \tag{1.2}$$

where R_m stands for the specific resistance of a unit area of the membrane and a is the radius. Here, $2\pi a$ is the circumference of an axon, which is related to the membrane surface area of unit length, and thus the total number of ion channels per unit length. Since more ion channels mean lower resistance, the radius a is inversely proportional to the membrane resistance.

The axial resistance depends on the cross-sectional area of the axon, i.e. its radius a, and the specific resistance of a $1cm^3$ volume of the cytoplasm (ρ). Thus, it can be expressed as

$$r_a = \rho/\pi a^2. \tag{1.3}$$

Here, the cross-sectional area is inversely proportional to the axial resistance, since bigger cross-sectional area allows more charge (ions) to flow per unit length.

Equation 1.1 governs the change in the membrane potential along the axon in response to the received signals. If the input signal is applied to the axon at a point (i.e. at x = 0), the resulting membrane voltage depends on the distance from the site of application. Specifically, the amplitude of membrane voltage decreases with increasing distance from the application site, and the signal eventually dies out. This decrease is exponential with distance, and given by

$$\Delta V(x) = \Delta V_0 e^{-x/\lambda}, \tag{1.4}$$

where $\Delta V(x)$ is the membrane potential difference with a distance x away from the application site, ΔV_0 is the membrane potential difference at application site x=0 and λ is the membrane length constant, defined as the distance where the membrane potential is decreased to 1/e of its original value and expressed by

$$\lambda = \sqrt{(r_m/r_a)} = \sqrt{\frac{R_m a}{2\rho}}. \tag{1.5}$$

This parameter indicates that how efficient a voltage change propagates along an axon is proportional to the radius a and specific membrane resistance of the axon R_m and is inversely proportional to the specific resistance of the cytoplasm ρ.

1.1.4 Strategies to optimize the conduction velocity

An action potential needs to propagate with a certain velocity, so that the nervous system can function properly. The conduction velocity of an action potential depends on the length constant λ: For higher length constants, the spike propagates more rapidly, and vice versa.

Several strategies have evolved to increase the length constant in order to optimize the conduction velocity of action potentials. One of these mechanisms is increasing the diameter of axons, which decreases the axial resistance and consequently increases the conduction velocity. This might be the reason why many invertebrates like squids have giant axons and why axons with higher conduction velocities generally tend to have larger diameters.

Another strategy to increase the conduction velocity is insulating the axonal membrane, which reduces the current leaking out. The axonal membranes are wrapped with a lipid-rich substance called myelin, generated by oligodendrocytes in the central nervous system and Schwann cells in the peripheral nervous system. As a result, insulation of the membrane increases the membrane resistance r_m as well as the length constant λ, allowing the spike to propagate passively along the axon for longer distances. Moreover, the thickness of the axonal membrane is increased if wrapped by myelin, leading to lower capacitance values, which means that the charge needed to change the potential across the membrane is decreased, making the generation of a spike easier. Thus, lower capacitance contributes to higher conduction velocities as well.

However, insulating the whole axon does not generate the highest conduction velocities, since the action potential would die out eventually. To prevent this, in many axons ~2 μm long unmyelinated axonal membrane segments which are densely populated with voltage-gated ion channels (nodes of Ranvier) appear between segments that are wrapped in a myelin sheath. In such a myelinated axon, an action potential is generated at each unmyelinated part followed by a passive propagation along the myelin sheathed segment. This is a very effective mechanism to speed up the propagation of a spike. The conduction velocity of a spike along an unmyelinated axon is 0.5-10m/s, while a myelinated axon can conduct a spike with up to 150 m/s of speed[2].

Since myelination is crucial to increase the conduction velocity, neurodegenerative diseases causing demyelination, such as multiple sclerosis, Guillain-Barre syndrome and Charcot-Marie-Tooth disease have devastating outcomes, including motor weakness, paralysis or abnormal somatic sensations [3-5].

1.2 Synaptic transmission

Once the action potential propagates along the axon to the presynaptic terminal of a neuron, signals are transmitted through specialized structures, called synapses, to the other neurons they are connected to. In human brain, each neuron branches out and synapses with ~1000 postsynaptic neurons, and receives signals from even more neurons, ~10000 on average via synapses. Synaptic transmission is essential for the brain's activity, since the communication of different parts of the brain is required for complex processes, such as learning, memory and perception.

1.2.1 Electrical synapses

One of the main types of synapses are electrical synapses, which connect pre- and postsynaptic neurons via gap junctions, specialized channels providing direct cytoplasmic connection between two neurons. The electrical current can flow easily bi-directionally through these channels between neurons, maintaining a low ionic resistance. Therefore, the transmission is highly rapid, resulting in the synchronous firing of connected cells.

1.2.2 Chemical synapses

Unlike electrical synapses, chemical synapses are slower, since the neurons are not physically connected via structures like gap junctions. Instead, there is a 20-40nm gap between pre- and postsynaptic neuron, called the synaptic cleft. The transmission of the signal depends on the diffusion of signaling molecules, called neurotransmitters, through the synaptic cleft to relay

the signal from pre- to postsynaptic neuron. These neurotransmitters are confined in synaptic vesicles, which are concentrated in the presynaptic terminals. Once the action potential reaches the presynaptic terminal, the potential change leads to the opening of Ca^{2+} channels, resulting in the increase of Ca^{2+} concentration at the terminal. These ions facilitate the exocytosis of the synaptic vesicles into the synaptic cleft, allowing the neurotransmitters to be released in the cleft. The neurotransmitters then diffuse through the synaptic cleft and bind to postsynaptic membrane receptors, causing the opening or closing of membrane channels and changing the postsynaptic membrane potential. All of these steps decrease the speed of signal transmission in chemical synapses, resulting in delays of approximately 0.3ms to several milliseconds. However, chemical synapses are advantageous in that they can amplify pre-synaptic signals, since each synaptic vesicle contains thousands of neurotransmitters leading to the activation of thousands of ion channels in the postsynaptic neuron.

Many different molecules can act as neurotransmitters, such as small molecules and peptides. However, the response of the postsynaptic neuron does not depend directly on the chemical structure of the neurotransmitters. Instead, the properties of the postsynaptic receptors that neurotransmitters bind to determine the voltage changes in the postsynaptic neuron. Based on the type of the ion channels and the action caused by the binding neurotransmitter, the postsynaptic neuron can be either depolarized (increase in voltage) or hyperpolarized (decrease in voltage). For instance, the opening of Cl^- channels would cause rapid inflow of Cl^- and subsequently lead to the hyperpolarization of the postsynaptic neuron, but the opening of Na^+ channels would lead to inflow of sodium causing neuronal depolarization.

9

1.3 Neuronal networks

The human brain consists of 10^{11} neurons connected by 10^{14} synapses giving rise to a network organization in the brain [6]. This network structure is essential for the communication among different brain regions and for the integration of neural information. As a result, coherent mental and cognitive states emerge, such as visual recognition, language, emotion and social cognition.

Connectivity in the brain can be analyzed from different perspectives. The structural (neuroanatomical) connectivity refers to the physical connections in the brain [7]. On the macroscopic level, they can be characterized by imaging techniques like diffusion tensor imaging (DTI), which is based on tracing water diffusion through the neurons [8], or other direct labeling techniques [9]. The functional connectivity, on the other hand, is defined as the temporal correlation between the activities of distinct brain regions, provided by synaptic transmission [7]. To determine this temporal correlation, functional connectivity at a macroscopic level can be studied by using several types of brain data, such as electroencephalogram (EEG) and magnetoencephalogram (MEG) [10], local field potentials (LFP) [11], functional magnetic resonance imaging (fMRI) [12] or positron emission tomography (PET) recordings [13].

Up keep of neural processes through which action potentials are transmitted, as well as that of synapses themselves is energetically costly. Therefore, the network structure in the brain is organized in a way to minimize the energy cost of synapses without compromising on its functioning [7]. This is facilitated by the modular structure of the brain. Namely, the brain has highly connected, specialized modules consisting of spatially close neurons [14]. However, distinct modules are sparsely connected, enabling integration of information between modules.

This gives rise to neurons with high degree of connectivity, also known as hubs, in the brain networks [7, 15].

Due to the complex network organization of the brain, graph theory analysis has been applied to neuronal networks, where neurons represent the nodes of the networks and synapses represent the connections between the nodes. Graph measures on human fMRI and DTI data enabled the identification of many potential structural and functional hub regions, respectively. For instance, functional hubs are found in precuneus, cingulate gyrus, ventromedial frontal cortex and inferior parietal brain regions [7, 16, 17], whereas high-degree regions in the parietal, frontal and insular cortices are shown to contain many structural hubs [18-21]. Since chemical synapses are unidirectional, it is reasonable to claim that structural connectivity has a directionality, which is studied with tract tracing and other invasive methods in non-human species [14, 22, 23]. These studies suggest that hub regions can be characterized as 'sources', if they have predominantly outgoing connections, including hubs in the cingulate, entorhinal and insular cortices. On the other hand, hubs with predominantly incoming connections are defined as 'sinks', such as portions of frontal and paracingulate cortices [14, 22, 23]. In addition, many studies with fMRI coupled with graph theoretical analyses suggest that functional networks of humans exhibit scale-free organization, described as networks with power-law degree distribution, having a lot of neurons with a few connections and a few 'hubs' with a lot of connections [24-26].

Many studies provided evidence that abnormalities of structural connectivity or functioning of hub regions correlate with behavioral and cognitive impairments, which lead to many neurological and psychiatric diseases [27-31]. For instance, disrupted structural and functional connectivity at frontal hub regions and at multimodal association cortex are shown to result in schizophrenia [28, 29]. Moreover, studies with children with autism indicated that

intramodular and intermodular connections were impaired at densely connected limbic, temporal and frontal regions [32]. In addition, medial parietal and frontal regions, where network hubs are densely located, have disturbed connectivity in Alzheimer's disease (AD) [33] and frontotemporal dementia [34], respectively. Such evidence proves the significance of proper organization of hub regions, which relies on proper synaptic transmission.

1.4 Failure in synaptic transmission

As described above, synaptic transmission is a multi-step process, and a problem at any one of these steps may lead to its failure. The chemical synapses may fail to transmit signals due to the depletion of neurotransmitters or external changes in membrane/ion channel activity. Examples of the latter that occur in AD include interaction of oligomeric Aß or misfolded tau with cell surface receptors, intracellular signaling molecules or scaffold proteins, which leads to the deterioration of synaptic structure and function [35]. Another example is an interaction of anesthetics with $GABA_A$ or NMDA receptors, or K^+ channels, causing hyperpolarization, glutamate desensitization or increase in K^+ conductance at the postsynaptic neuron, respectively [36].

Subsequently it is no surprise that synaptic failure can change functional network connectivity and, consequently information processing leading to potentially devastating outcomes. For instance, synaptic failure is suggested to be part of the cause of most neurodegenerative diseases including AD, Huntington, ALS, and ischemic cerebral damage. In fact, it may be the first pathologic event to occur in these diseases, even before the loss of neurons [37]. However, synaptic transmission failure may target different components of the network and lead to different consequences in terms of changes of spatio-temporal patterning in the network. Buckner et al. (2009) provided evidence that cortical hubs (i.e., regions that integrate and transmit

information from/to many other parts of the brain) in humans are the most vulnerable areas to amyloid deposition, which results in atrophy and eventually AD [30]. Moreover, another study on mice showed that amyloid deposition is caused by excessive neuronal and synaptic activity in vivo [38]. In another study, de Haan et al. (2012) hypothesized that hubs are the most active regions in the brain, which can result in "activity dependent degeneration" [39]. Their results verified this hypothesis and identified that activity dependent degeneration results in hub vulnerability as well as macro-scale disruption of brain connectivity, as observed in AD.

Anesthetics represent another scenario where synaptic failure, in this case more of a controlled synaptic suppression, causes a significant disruption of brain functioning, i.e. loss of consciousness. Anesthetics are thought to act through ion channel blockage and/or changes in cellular membrane dynamics which lead to synaptic failure [40]. One of the observed outcomes of anesthetics on a macro-network scale is a decrease in the large-scale functional connectivity between different parts of the brain. In particular, it was postulated that the hub regions of the brain are primarily affected by anesthetics and lead to the loss of global functional connectivity which is followed by loss of consciousness [41]. In a similar spirit, another study investigated directionality of information flow across brain networks by simulating simple oscillatory models at the nodes of a human anatomical brain network. They found the directionality of a network is determined by its topology [42]. Based on their finding that hub nodes phase lag while peripheral nodes phase lead, they concluded that connections are directed from lower to higher degree nodes. Further, they perturbed the hub structure to simulate an unconscious state, leading to the elimination of the directionality in the neuroanatomical network, which is consistent with data from anesthetic administered in humans, where anterior (less hubs)- to-posterior (more hubs) directionality was lost. In the first project of this thesis, I will show, however, that targeted

elimination of connectivity in scale-free networks may lead to more complex and unexpected changes in spatiotemporal patterns of their activity (Chapter II).

1.5 Auditory system

In the second part of my thesis, I investigated the role of specific experimentally measured pathologies in myelination patterns of auditory axons on spike propagation and their possible cognitive consequences.

Hearing and distinguishing a wide range of sounds are facilitated by the auditory system, where mechanical sound waves are transduced into electrical signals in the ear. These electrical signals are transmitted to the brain, which processes the auditory information and enables the recognition of the sound. Many studies suggested that disruption in the signal transmission in the auditory system due to damaged synapses results in many types of hearing deficits [43-45]. Therefore, an undisturbed flow of information through auditory pathways is necessary for a proper hearing.

1.5.1 Sound waves

Sound can be defined as vibrations propagating in a medium (e.g. air, water) and causing pressure differences in the medium they propagate. The perception of sound requires the propagation of the sound into the ear. The pressure differences that a pure tone sound generates can be represented by a sinusoidal wave. The frequency of this wave indicates the pitch of the sound. Humans can perceive frequencies between 20Hz-20kHz, although some animals can distinguish frequencies out of this range [46].

The amplitude of the sound wave P relates to the sound intensity L, which can be defined as:

$$L = 20 \log_{10}\left(\frac{P}{P_{ref}}\right), \qquad (1.6)$$

where the sound intensity L is in decibels sound pressure level (dB SPL), P is the magnitude of the stimulus described as the root mean square of the sound pressure in pascals, and P_{ref} is $20\mu Pa$ corresponding to the pressure generated by 0 dB SPL [47]. This implies that doubling the loudness requires ten times more sound pressure.

1.5.2 The propagation of the sound waves in the ear

The ear, as the primary auditory sensory organ, contains the auditory receptor called the organ of Corti, where mechanoelectrical transduction of sound waves takes place. The ear consists of three functional parts: external ear, middle ear and inner ear (Figure I.3).
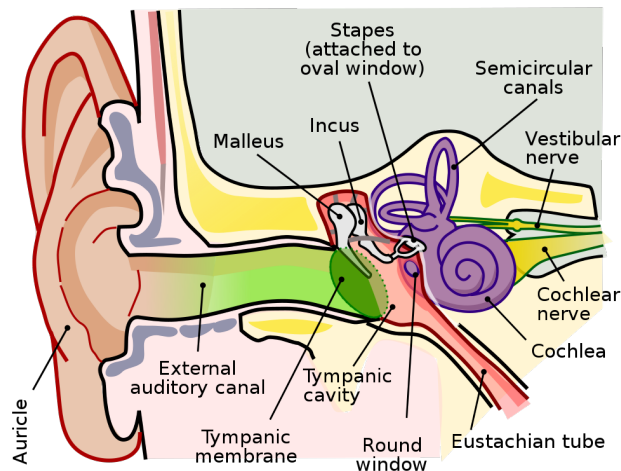
Figure I.3   **The structure of the human ear.** The ear consists of auricle and the external auditory meatus in the external ear, tympanium and the ossicles in the middle ear, and cochlea in the inner ear.

The external ear is composed of the auricle and the ear canal (external auditory meatus). The auricle, the cartilage-based, folded structure, is the visible part of the ear and plays a role in collecting the sound from the surroundings like an antenna and transferring it to the ear canal. Sound waves travel through the ear canal which ends at the eardrum (tympanum), a thin membrane with 9mm diameter separating the external ear from the middle ear [48].

15

The middle ear is responsible for transmitting sound waves to the inner ear, where the organ of Corti resides. The arrival of sound waves to the eardrum results in its vibration. There are three ossicles (bones) in the middle ear: malleus, incus and stapes. The eardrum is connected to the malleus, which is attached to the incus, and the incus connects with stapes. The vibration of the eardrum is transferred through these bones to the oval window, the starting point of the inner ear. Since the surface area of the eardrum is larger than the surface area of the stapes, where it connects with the oval window, the pressure of the vibration is amplified when it is transferred into the inner ear.

The cochlea, a conical structure shaped like a snail's shell, resides in the inner ear. It consists of three tubes filled with fluid: the scala vestibuli, the scala tympani and the scala media. The scala vestibuli is the tube at the top, which has the oval window at its base. It is connected to the scala tympani at the helicotrema at the most apex part of the cochlea. The scala tympani opens to the middle ear via the round window at its base, which is covered by a thin membrane. The scala media is between the scala tympani and the scala vestibule, where the organ of Corti is embedded. Due to sound vibration, the stapes pushes inward through the oval window. This movement creates pressure changes in the scala vestibule that displaces the fluid in it. The motion of the fluid due to the movement of the stapes leads to a deflection of the basilar membrane, a membrane between the scala tympani and scala media [47]. This movement activates the organ of Corti and the sound wave is transduced to an electrical signal (Figure I.4).
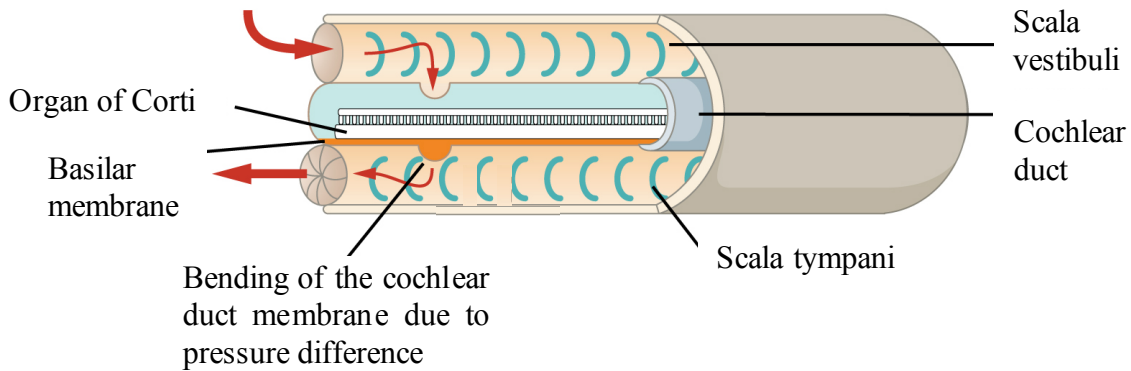
Figure I.4 **The propagation of the sound vibration through the cochlea.** For a better intuition, the cochlea is drawn as unfolded.

1.5.3 Mechanoelectrical transduction in the cochlea

The organ of Corti is the auditory receptor organ responsible for translating mechanical sound waves into electrical signals. It consists of hair cells and a variety of supporting cells. Hair cells are aligned along the basilar membrane and their cilia face towards the tectorial membrane, which lies over the hair cells. The movement of the basilar membrane as a result of sound waves traveling through the cochlea tilts the cilia of the hair cells, opening the mechanosensitive K^+ channels and depolarizing the hair cell. There are two types of hair cells: inner hair cells (IHC) and outer hair cells (OHC). The OHCs are mainly responsible for the amplification of low-intensity sounds, whereas IHCs play a role in signal transduction. Each IHC forms synapses with the peripheral axons of the bipolar spiral ganglion neurons (SGNs), also known as auditory nerves, which send the signals coming from hair cells to the cochlear nucleus in the brain. Changes in the membrane potential of the IHC trigger the opening of Ca^{2+} channels in the vicinity of IHC-SGN synapses, facilitating the exocytosis of the neurotransmitters [47, 49].

1.5.4 Tonotopic organization in the auditory system

The frequency information of sounds is encoded in the cochlea by the activation of distinct IHCs for different frequencies. This mechanism is facilitated by the non-uniform structure of the

17

basilar membrane. From the base to the apex, the basilar membrane becomes continuously wider, thinner and floppier. This structure gives rise to the tonotopic organization of the basilar membrane, meaning that each position along the membrane vibrates with the biggest amplitude in response to a specific sound frequency. For lower sound frequencies, more apical parts of the membrane are excited the most, due to the floppiness, and for higher sound frequencies, basal parts of the membrane are activated. Since the IHCs are located along the basilar membrane in the cochlea, excitation of each part depolarizes a different population of IHCs. This means that different IHCs are active for distinct sound frequencies, and the frequency that an IHC is most sensitive to is called the "best frequency" of that IHC. This tonotopic organization in the peripheral auditory system is also projected to the more downstream parts of the auditory circuits [50].

Even though each IHC is the most sensitive to sound at its best frequency, this does not mean that they do not respond to other frequencies. Increasing sound intensity broadens the area of vibration along the basilar membrane, thus activating IHCs with best frequencies near the sound frequency. The tuning curves for IHCs with different best frequencies demonstrate this effect, where the frequency that minimizes the threshold represents the best frequency (Figure I.5). The farther the sound frequency is from the best frequency of that IHC, the less sensitive the IHC is to that sound [47].
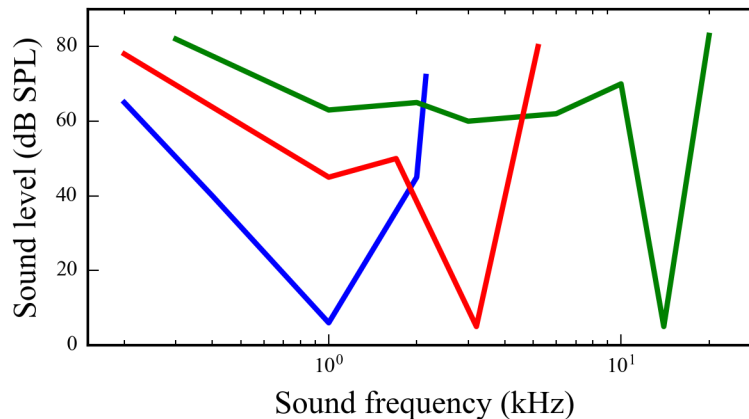
Figure I.5   Tuning curves for inner hair cells (IHCs) with best frequencies at ~1kHz (blue), ~3kHz (red) and ~15kHz (green). This figure shows the threshold sound levels needed to activate each IHC corresponding to the frequency of the sound stimulus (Data taken from [47]).

1.5.5 SGN fiber types

Experimental studies suggest that presynaptic Ca^{2+} currents may determine the transmitter-evoked postsynaptic currents [51, 52]. Therefore, it has been hypothesized that the response of the postsynaptic SGN fiber to different sound levels depends on the density of the Ca^{2+} channels near the presynaptic terminal of IHCs [52]. The SGN fiber receiving signals from synapses with dense Ca^{2+} channels at the presynaptic terminals may possibly fire with lower sound pressure levels, or even spontaneously. However, if the Ca^{2+} channel concentration near the presynaptic terminal is low, then the IHC may need a higher potential increase for a synaptic release event, which would arise from a higher sound pressure level. Based on their spontaneous firing rates and saturation profiles, SGN fibers can be classified into three groups: low- (LT), medium- (MT) and high threshold (HT) SGN fibers. The spontaneous rate of LT fibers is the highest with 18-100 spikes/s and their dynamic range is the lowest among all types, reaching their maximum discharge rate within approximately 30 dB sound pressure level (SPL). The spontaneous rate of MT fibers is lower (between 0.5 and 18 spikes/s) and their dynamic range is higher than LT fibers. HT fibers have the lowest spontaneous rates (<0.5 spikes/s) among all, and respond to sound pressure levels

19

higher than 20 dB SPL. Their spike rate increases linearly with increasing sound levels (Figure I.6) [53].
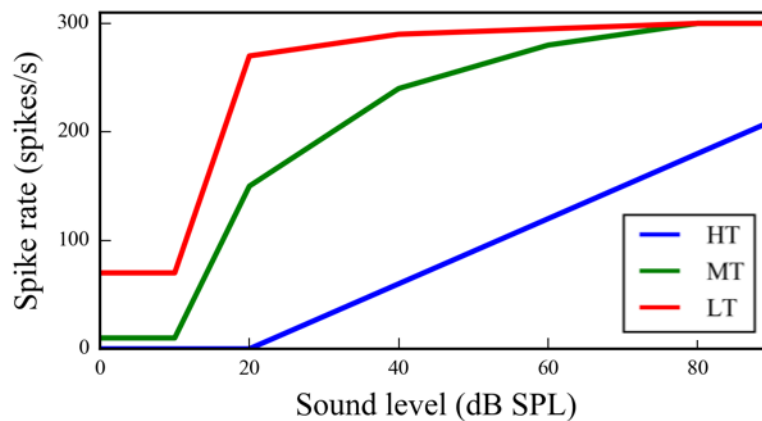
Figure I.6   The rate-intensity functions for low-threshold (LT), medium-threshold (MT) and high-threshold (HT) SGN fibers (Data taken from [53])

1.5.6 SGN fiber activity generates the temporal and intensity cues for sound localization

The SGN fibers project to higher order auditory structures in the central auditory system, where sound recognition and localization takes place. First, they form synapses with different types of cells in the cochlear nucleus. One of the cell types in the cochlear nucleus is the bushy cell, which integrates inputs from multiple SGN fibers and acts as a coincidence detector, meaning that it only fires when multiple inputs are received within a short time window. As a result, bushy cells are more phase-locked to sound than SGN fibers [54]. This precise temporal information is then transmitted to the superior olivary complex (SOC), the first binaural convergence point in the brainstem responsible for azimuthal sound localization.

There are two main nuclei which play crucial roles in localizing the sound in the horizontal plane: the lateral superior olive (LSO) and the medial superior olive (MSO). There are LSO and MSO nuclei on each side of the brain, and each nucleus receives synaptic inputs from cochlear nuclei emanating from each side of the head. LSO cells are sensitive to the difference in intensities

20

perceived by the two ears, also known as the interaural level difference (ILD). ILDs can be detected for high frequency sounds (>2kHz), since the head can create an acoustic shadow for sounds with wavelengths shorter than the head diameter, creating an intensity difference between two ears. This shadowing depends on the location of the sound source, meaning that the intensity of the sound is perceived lower at the ear farthest from the sound source. As a result, LSO cells ipsilateral to the ear that is closest to the sound source fire more, as they get excitatory input from the ipsilateral bushy cells and inhibitory input from contralateral bushy cells [55].

MSO cells, on the other hand, are sensitive to interaural time differences (ITDs), the difference in arrival time of a sound between the two ears, for mainly low frequency sounds (<2kHz) [56]. ITDs arise from the location of the sound source. That is, if a sound originates from the mid-sagittal plane, the path it needs to travel to both ears is the same, i.e., ITD equals zero. However, the more the sound source is deviated from the mid-sagittal plane, the bigger is the absolute ITD.

MSO cells get excitatory inputs from both ipsi- and contralateral spherical bushy cells [55]. Moreover, they act as binaural coincidence detectors facilitated by their intrinsic properties, low membrane time constants (<2ms) and input resistances (<10MΩ), allowing them to fire only if the inputs from both ears arrive within a very short time span [57]. If the sound source is localized closer to one ear (the ipsilateral ear), the inputs from each ear coincide more closely at the MSO on the other side of the brain (the contralateral MSO) since the signal from the contralateral ear needs to travel farther to the other side of the brain. Hence, MSO cells contralateral to the ear that is closest to the sound source fire with the highest frequency, and the ITD resulting in the highest MSO activity is called the best ITD. A typical ITD function for an MSO cell is a bell-shaped curve

having a peak at the contralateral site (Fig. I.7), and this shift from zero ITD gives rise to the ITD sensitivity [58].
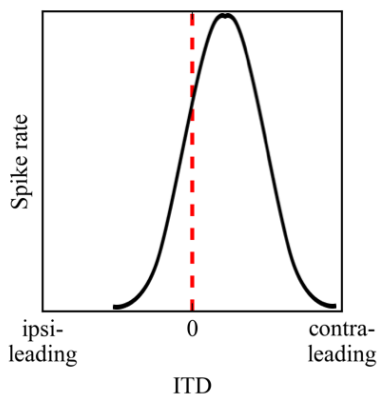
Figure I.7   **ITD function of an MSO cell.** Spike rate of an MSO cell is highest for slightly contralateral sound sources that gives rise to binaural coincidence.

1.6 From synaptic and transmission disruption of SGNs to hidden hearing loss

Hidden hearing loss (HHL) is defined as an auditory neuropathy characterized by changes in sound-evoked neural output of the SGN without hearing threshold elevation [59]. HHL has been detected in animal models by measuring the neural responses to suprathreshold sound via tests, such as the auditory brainstem response (ABR), a far-field response measured by head-mounted electrodes, or the compound action potential (CAP), a near-field response measured from the round window. The first peak of ABR (ABR peak 1) represent the activity of type I SGNs in response to sounds, and CAP reflects the synchronous response of the SGN fibers at the sound onset [59]. In humans, it has been hypothesized that difficulties in hearing, especially in noisy environments, with normal hearing thresholds may indicate HHL [59]. However, it is still controversial, as perceptual deficits have not been linked to SGN activity in humans.

In animal studies, there is mounting evidence that HHL can be caused by noise exposure, aging or peripheral myelin neuropathy [45, 60-62]. After exposure to moderate noise, animals have temporary shifts in auditory thresholds but permanent decreases in amplitude of ABR peak 1 [45,

60-62]. Kujawa and Liberman (2009) showed that animals with this type of auditory pathology have a normal complement of hair cells and SGNs, but present with loss of a subset of synaptic connections between IHCs and SGNs. They also found that the degree of synapse loss correlates with the magnitude of the decrease in suprathreshold responses, supporting the idea that cochlear synaptopathy is the mechanism for noise-induced HHL [60]. Similar observations were made regarding aging, i.e. HHL and synapse loss are the first signs of age-related hearing loss and have the same time-course [45]. Importantly, it has been suggested that moderate noise and aging primarily affect synapses associated with high threshold/low spontaneous rate SGN fibers [43]. Since these fibers can respond to sound in high background noise even when the others have been saturated, their loss could lead to difficulties in processing speech in noisy environments [43].

Proper myelination of SGNs plays a significant role in auditory processing [63]. Therefore, it has been hypothesized that peripheral neuropathy resulting from myelin disorders may be another cause of HHL. Individuals with peripheral neuropathies, such as Guillain-Barré Syndrome (GBS) [64] and Charcot-Marie-Tooth (CMT) disease [65] have been reported to have perceptual difficulties even when having normal auditory thresholds, that may indicate HHL. A recent study by Wan and Corfas (2017) showed that transient demyelination also causes HHL in mice, i.e. reduced ABR peak 1 amplitude with normal ABR thresholds [61]. In that study, acute demyelination was induced using genetically modified mice. This demyelination resulted in decreased ABR peak 1 amplitudes and increased ABR peak 1 latency without auditory threshold elevation or IHC-SGN synapse loss. Remarkably, these changes persisted even after remyelination of SGN fibers. Further investigation with immunostaining demonstrated that the organization of the heminodes, the nodal structures closest to the IHCs where action potentials are generated, were disrupted. These results suggested that the location of SGN heminodes is critical for normal

auditory responses and that their disruption causes HHL. In Chapters III and IV, we model synaptic and transmission failure in SGNs to better understand how these mechanisms can lead to HHL and how subsequent disruptions in the sound localization circuit may contribute to perceptual deficits associated with HHL.

1.7 Outline

The aim of the work in this dissertation is understanding the effect of disruptions of synaptic transmission on neuronal network activity with computational modeling methods. The study in Chapter II is a theoretical study to investigate the universal, system-wide effects of synaptic failure on large network dynamics. Chapters III and IV focus on a more specific case of disrupted synaptic transmission in the auditory system, hidden hearing loss (HHL).

The work in Chapter II is motivated by previous studies on humans suggesting that the application of anesthetics causes desynchronization of activity in different parts of the brain as a result of the disconnection of the hub regions of the brain. To test this hypothesis, we built large, scale-free neural network models consisting of leaky integrate-and-fire model neurons, which is a simplified model capturing basic features of neuronal firing. Using these models, we analyzed spatiotemporal pattern formation across large network structures with different levels of synaptic failure. As a result, this study demonstrated that disconnecting hubs might facilitate the emergence of more coherent and synchronized network states due to more balanced input levels within the network. This finding may contradict the hypothesis that disconnecting hubs decreases global coherence of brain networks and may also explain why some patients have seizures after the application of anesthetics [66, 67].

The work in Chapters III and IV is motivated by another consequence of disruption of synaptic signaling, namely HHL, an auditory neuropathy caused by noise, aging or myelin defects

resulting in hearing deficits, particularly in noisy environments. There are two main hypotheses for the mechanisms of hidden hearing loss: loss of synapses between inner hair cells and SGNs or myelin defects at the heminode of peripheral SGN axons. In Chapter III, we modeled these two scenarios to understand how they contribute to HHL mechanistically. Specifically, we constructed a computational model of sound-evoked SGN fiber activity and auditory nerve compound action potential to understand how each one of these mechanisms affects nerve transmission. We show that disruption of auditory-nerve myelin desynchronizes sound-evoked auditory neuron spiking, decreasing the amplitude and increasing the latency of the compound action potential. In addition, elongation of the initial axon segment may cause spike generation failure leading to decreased spiking probability. In contrast, the effect of synapse loss is only to decrease the probability of firing, thus reducing the compound action potential amplitude without disturbing its latency.

Many studies suggest that humans with HHL or demyelinating diseases have binaural processing deficits, which is essential for localizing sound. In Chapter IV, we used the model described in Chapter III to make further predictions on the consequences of HHL due to myelinopathy. Specifically, we explored the impact of myelinopathy on sound localization by simulating the activity of SGN fibers, bushy cells and MSO cells evoked by low frequency sounds. Since bushy cells and MSO cells act as coincidence detectors, decreased and desynchronized SGN activity in myelinopathy reduce the firing rates of bushy cells and MSO cells, providing evidence for sound localization deficits in HHL.

Chapter II

Synaptic Failure Differentially Affects Pattern Formation in Heterogeneous Networks

2.1 Introduction

The communication of neurons is primarily maintained by synapses, which play a crucial role in the functioning of the nervous system. Therefore, synaptic failure may critically impair information processing in the brain and may underlie many neurodegenerative diseases [35-37]. A number of studies have suggested that synaptic failure may preferentially target neurons with high connectivity (i.e., network hubs) [30, 41]. As a result, the activity of these highly connected neurons can be significantly affected. It has been speculated that anesthetics regulate the conscious state by affecting synaptic transmission at these network hubs and subsequently reducing overall coherence in the network activity [41]. In addition, hubs in cortical networks are shown to be more vulnerable to amyloid deposition because of their higher activity within the network, causing decrease in coherence patterns and eventually Alzheimer's disease (AD)[30]. In this chapter, we investigated how synaptic failure can affect spatiotemporal dynamics of scale free networks, which have a power law scaling of the number of connections per neuron. In these networks, relatively few neurons (hubs) have a lot of emanating or incoming connections while the majority of cells have low connectivity. We studied two types of synaptic failure: activity-independent and targeted, activity dependent synaptic failure. We defined scale-free network structures based on the

dominating direction of the connections at the hub neurons: incoming and outgoing. We found that the two structures have significantly different dynamical properties. We showed that synaptic failure may not only lead to the loss of coherence but unintuitively can also facilitate its emergence. We showed that this is because activity-dependent synaptic failure homogenizes the activity levels in the network creating a dynamical substrate for the observed coherence increase. Obtained results may lead to better understanding of changes in large-scale pattern formation during progression of neuro-degenerative diseases targeting synaptic transmission. These results have been published in *Frontiers in Neural Circuits* [68].

2.2 Materials and Methods

2.2.1 Network structure and connectivity

We used the Barabasi – Albert algorithm [69] on a population of 1000 neurons to create a scale-free connectivity. We started with an all-to-all connected network of n neurons, and then expanded the network continuously by connecting new neurons to the n pre-existing ones using a preferential attachment principle: neurons with more connections have a higher chance to receive new connections. This results in a bidirectionally connected network with $\frac{n}{10}$% connectivity. Unless otherwise stated, we used n=16 (1.6% connectivity) in our simulations. Then, we proceeded to make the connections unidirectional and defined two network transmission directions: incoming and outgoing. For that purpose, we first enumerated the neurons 1 to 1000 based on the time step they were added to the network. The earlier the neurons were added to the network, the higher chance they had to get new connections. Therefore, the neurons being assigned smaller numbers would eventually be more likely to have more connections. Then, we defined two different network structures according to the predominant directions of the connections at the hubs, i.e.

nodes having a lot of connections with many other nodes [6]. We defined incoming networks as networks with hubs having majority of incoming connections. Therefore, we changed all bidirectional connections of the network into unidirectional connections from bigger to smaller-numbered neurons. Conversely, in outgoing networks, hubs are dominated by outgoing connections. Therefore, the connections were directed from the neurons with smaller numbers to the ones with bigger numbers. Below, we will refer to these connectivity structures as 'incoming' and 'outgoing' networks, respectively [Fig.II.1(A)].
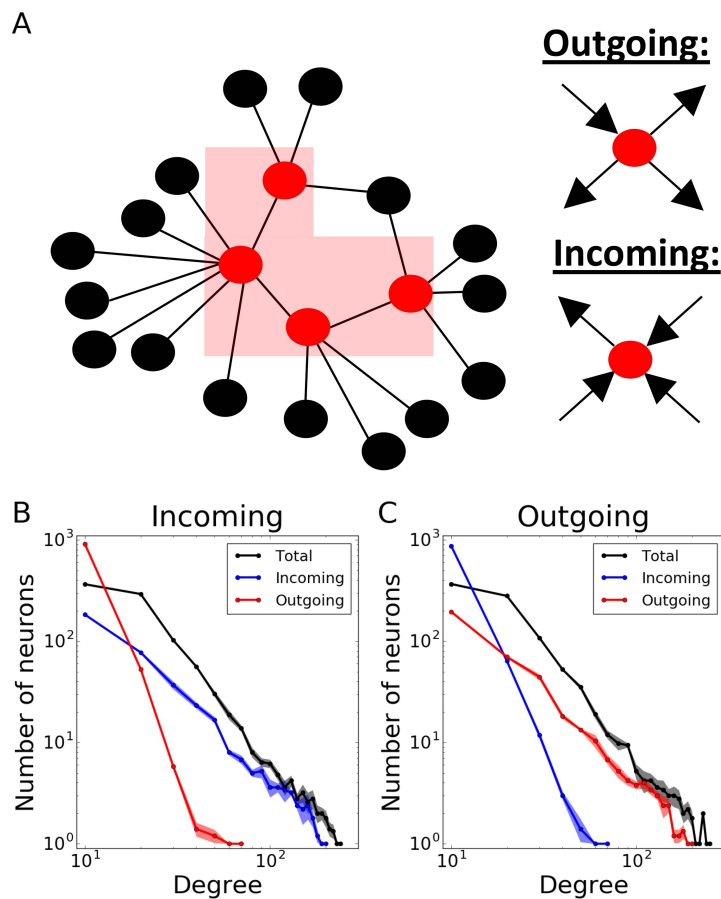
Figure II.1 Modeling different scale-free network structures depending on the directionality at the hubs.
(A) Scale- free networks are defined as 'outgoing', if the hubs have predominantly outgoing connections, and 'incoming', if the hubs have predominantly incoming connections. Total, incoming and outgoing degrees in both (B) incoming and (C) outgoing networks exhibit power-law distributions. Degree distributions are averaged over 5 different network realizations.

28

Finally, to obtain feedback connectivity, we randomly chose m% of all connections to change their directions. We defined this proportion (m%) as 'direction ratio' in the chapter. As a result, each neuron has $\frac{100}{m} - 1$ times more incoming than outgoing connections on average in incoming networks, and vice versa in outgoing networks. Unless otherwise stated, we used 17% direction ratio in both network structures in our simulations. Consequently, the resulting networks have a power-law degree distribution for their total, incoming and outgoing connections [Fig.II.1(B) and (C)].

We used an integrate-and-fire excitatory neuron model to describe dynamics of each node. The current-balance equation of this neuron model for the ith neuron is

$$\frac{\partial V_i(t)}{\partial t} = -\alpha V_i(t) + \gamma \sum_j J_{ij} S_j(t, t_s) + \beta I_{rand}, \tag{2.1}$$

where $V_i(t)$ is the membrane potential of the i-th neuron, J denotes the adjacency matrix, $\gamma = 0.25$V/s is the synaptic strength, $\alpha = 0.3$ms^{-1} is the inverse of the passive membrane time constant. The I_{rand} is a random term, which is a 0.1ms-wide rectangular current with an amplitude of 1, perturbing the neuronal dynamics with 100Hz frequency; $\beta = 6$V/s is a term to modify the amplitude.

A neuron spikes when its membrane potential reaches $V_i(t) = 1$. At the time of the spike, the voltage of the spiking neuron is reset to 0, and the neuron enters the refractory period of 5ms (t_{ref}). During this period, the neuron cannot receive any signals from its presynaptic connections [70].

There are no delays in the synaptic transmission. The postsynaptic signal arriving at each neuron is described by a double-exponential

$$S_i(t, t_s) = e^{\frac{-(t-t_{si})}{T_{decay}}} - e^{\frac{-(t-t_{si})}{T_{rise}}}, \tag{2.2}$$

where t_s is the last spike time of the i-th presynaptic excitatory neuron, T_{rise}=0.3ms and T_{decay}=3ms are rise and decay time constants, respectively.

For one set of our simulations (Fig.II.11), we added a population of inhibitory neurons consisting of 1000 neurons to the network. This population is randomly and unidirectionally wired with the same mean connectivity as excitatory population (1.6%). Moreover, inhibitory population sends connections to the excitatory one with 1.6% random connectivity, and vice versa. All parameters governing dynamics of inhibitory neurons are the same, except the sign in signal S_i:

$$S_i(t, t_s) = -\left(e^{\frac{-(t-t_{si})}{T_{decay}}} - e^{\frac{-(t-t_{si})}{T_{rise}}} \right), \qquad (2.3)$$

2.2.2 Implementation of synaptic transmission failure

We defined a parameter, transmission probability p_{trans} that provides a probability of a synapse passing (or failing to transmit) the signal, i.e., each synapse independently can pass (or fail) a presynaptic spike to a postsynaptic neuron. Here, we studied two realizations of this process: 1) activity-independent one, where transmission probability is constant (and the same for every synapse), and 2) activity-dependent one, where the probability of the synapse to succeed or fail depends on the time elapsed from the last spike of the postsynaptic neuron:

$$p_{trans}(t) = 1 - p_{syn} \times e^{\frac{-(t-t_{last}-t_{ref})}{T}}, \qquad (2.4)$$

where p_{syn} is the base failure probability, T is the failure recovery time constant and t_{last} is the last spike time of that neuron. Therefore, the term $t-t_{last}-t_{ref}$ denotes for the time passed after the last spike time and its corresponding refractory period.

2.2.3 Measures and statistics

For all realizations of the network and its dynamics, we measured the MPC (Mean Phase Coherence) between the neurons and the degree of the synchrony. The first measure allows us to assess the stability of the spatio-temporal pattern irrespective whether it is synchronous or asynchronous. Briefly, the instantaneous phase between two neurons is defined as

$$\phi_k = 2\pi \left(\frac{t_{2,k} - t_{1,k}}{t_{1,k+1} - t_{1,k}} \right), \tag{2.5}$$

where $t_{1,k}$ is the time of the last spike of the neuron 1 before that of the neuron 2 ($t_{2,k}$) and $t_{1,k+1}$ is the time of the first spike of the neuron 1 after $t_{2,k}$. Then the MPC between two neurons ($\sigma_{1,2}$) is

$$\sigma_{1,2} = \left| \frac{1}{N} \sum_{k=1}^{N} e^{i\phi_k} \right|, \tag{2.6}$$

where N is the number of spike combinations at the two cells. The network measure of MPC, $\langle \sigma \rangle$, is the average of all pairs [71].

The second measure indicates to what extent the neurons form synchronized pattern of activity. Here, the measure we used depends on the time-averaged fluctuations of the global voltage (σ_V) over an extended period of time, normalized to the average of N individual neurons' time-averaged fluctuations:

$$\lambda = \sqrt{ \frac{\sigma_V{}^2}{\frac{1}{N} \sum_{i=1}^{N} \sigma_{V_i}{}^2} }. \tag{2.7}$$

It is in the range of (0,1), increasing with synchronous activity [72]. The simulations were repeated 5 times, we calculated mean and its standard error to establish significance of the obtained results.

2.3 Results

We used scale-free network connectivity structures, which are thought to represent functional network connectivity in the brain [24]. Scale-free connectivity provides a power-law

distribution of nodal degrees resulting in a heterogeneous population of interconnected cells [69]. We further differentiated network types by establishing hub directionality, in the sense that the highly interconnected cells (the hubs) may predominantly receive inputs from other parts of the network, or send outputs to other cells (Fig. II.1[A]). The example statistics of the connectivity for both of these cases are provided on Fig. II.1 (B) and (C), where the direction ratio is being established at 17%.

First, to establish a baseline, we investigated pattern formation in the networks without failure, as a function of the mean connectivity [Fig. II.2 (A) and (B)] and direction ratio [Fig. II.2 (C) and (D)] in both incoming [Fig. II.2 (A) and (C)] and outgoing [Fig. II.2 (B) and (D)] networks. In incoming networks, the histograms of average MPC ($\langle\sigma\rangle$) as a function of neuron degrees, suggest that low degree neurons always have relatively lower MPC than the rest of the network, regardless of the connectivity and direction ratio of the network, because of the lack of common input they get. However, this difference is more pronounced for higher connectivities [Fig. II.2(A)]. Generally, we observe that for low connectivity the network has relatively few connections and thus it remains less heterogenous in terms of nodal degree. As the connectivity is increased, two competing mechanisms emerge – the networks become more heterogenous, but at the same time stronger connectivity leads to more synchronous dynamics, as is commonly observed. However, even though nodal contributions exhibit different patterns for different connectivities, these differences are only minimal in incoming networks.
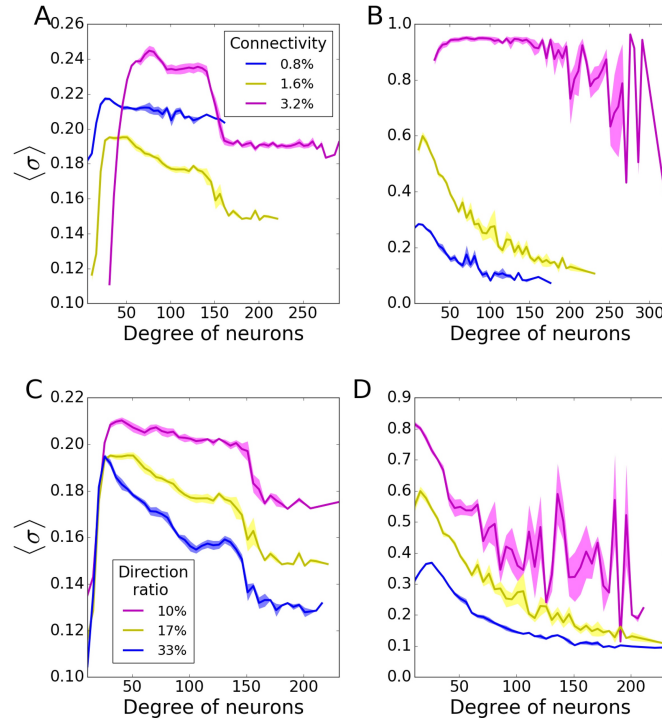
Figure II.2 Nodal contribution to network-wide Mean Phase Coherence (MPC) as a function of its degree for incoming [(A) and (C)] and outgoing [(B) and (D)] networks for different connectivities [(A) and (B)] and direction ratios at the hubs [(C) and (D)]. In incoming networks, (A) increasing connectivity causes a bigger gap between coherences of high- and moderate-degree neurons, whereas (C) increasing direction ratio decreases MPC of all degrees. In outgoing networks, MPC of all degrees increases with (B) increasing connectivity and (D) decreasing direction ratio. MPCs are averaged over 5 degrees and results are averaged over 5 randomized network realizations.

Connectivity has a bigger impact on outgoing networks [Fig. II.2(B)]. Higher connectivities result in more significant increases in MPC for all degrees. That is not surprising as hubs are the synchronizing agent to the rest of the network when they drive network activity. Unlike incoming networks, outgoing ones have the highest MPC for the neurons with lowest degrees, for 0.8% and 1.6% connectivities. The reason is that in these type of networks, neurons with lowest degrees receive signals from hubs and form synchronized clusters. This trend disappears for 3.2% connectivity though, since the network is saturated and neurons with all degrees are coherent. The bigger fluctuations for highest degrees at 3.2% connectivity might be due to the lower input they get from the network.

33

We then investigated how direction ratio (as defined in methods) affects network coherence. In incoming networks, MPC for all degrees is increased overall for lower direction ratios (more incoming connections at the hubs), although the change is not very significant [Fig. II.2(C)]. However; there is a more substantial rise in the case of outgoing networks, when hubs send more outgoing connections [Fig. II.2(D)]. These results point in the direction that the overall synchrony of the network is strongly dependent on the number of outgoing connections emanating from the hubs, rather than incoming ones. For the rest of our simulations, unless stated otherwise, we decided to use incoming and outgoing network structures with 1.6% connectivity,17% direction ratio.

Finally, we varied the frequency of random external kick I_{rand}. In case all neurons are disconnected (p_{trans}=0.0), spike frequency increases with increasing I_{rand} frequency, as expected. At the same time, as expected, the MPC decreases with more frequent I_{rand}. When all the connections are present (p_{trans}=1.0), both spike frequencies and MPCs are only minimally increased for higher frequencies of I_{rand}, since network connections dominate pattern formation. For the rest of our simulations, we chose the frequency of I_{rand} as 100 Hz. This value results in a spike frequency lower than 200Hz, the maximum frequency the network can fire due to the 5ms refractory period, when p_{trans}=1.0. Also, it introduces enough randomness to the network to make them spike less coherently when p_{trans}=0.0. These results are briefly summarized in Supplementary Figure II.1.

2.3.1 Activity – independent synaptic failure

We first investigated the history-independent transmission probability, where p_{trans} is constant. We compared the pattern formation (i.e., the MPC and synchrony) for the outgoing and incoming networks as we gradually varied p_{trans} between 0 and 1 for both network types. We

observed that outgoing networks are more sensitive to synaptic failure than incoming ones, as they become more coherent and synchronous with increasing synaptic transmission [Fig. II.3(A) and (B)].
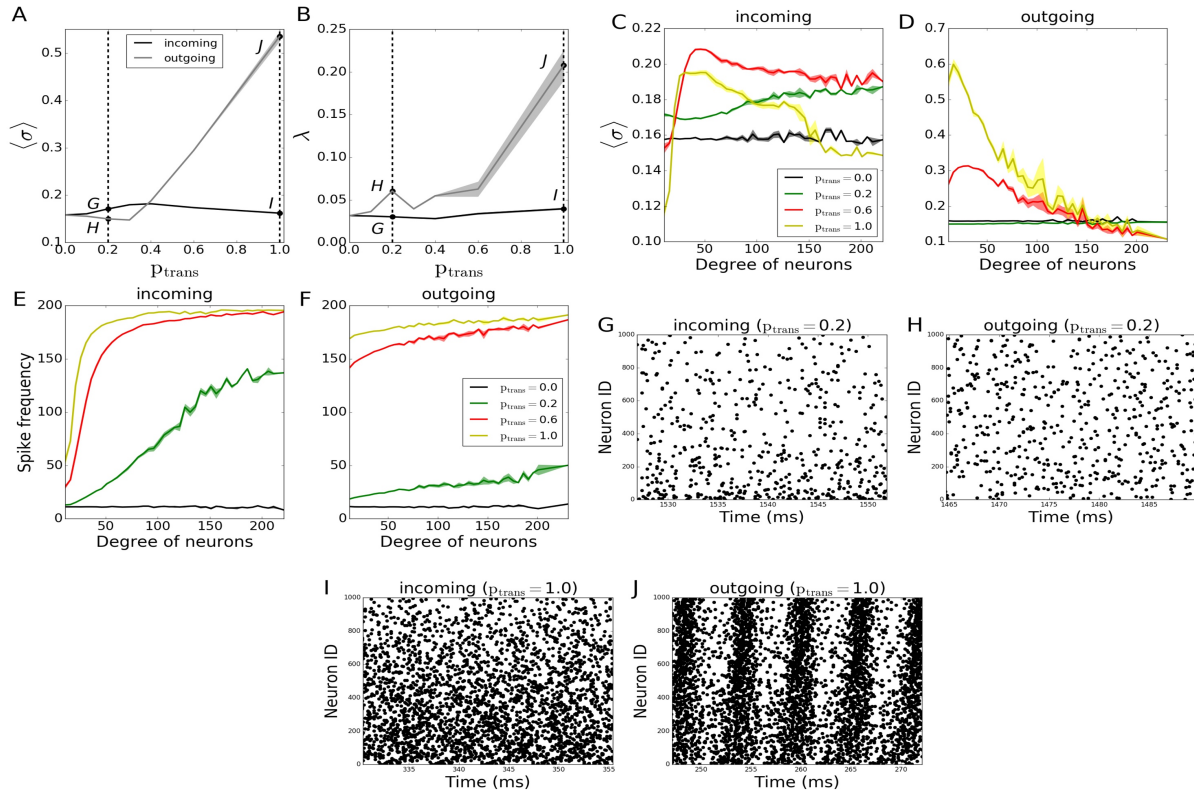
Figure II.3 Pattern formation in the networks with activity-independent synaptic failure. This figure shows that outgoing networks become more coherent and synchronous due to a more uniform spike frequency distribution throughout the network. Signals are transmitted through synapses of a neuronal network with a constant probability p_{trans}. (A) Mean Phase Coherence (MPC) and (B) Synchrony measure for incoming (black line) and outgoing (gray line) networks. [(C) and (D)] Participation in pattern formation as a function of nodal degree for activity-independent transmission failure. Histograms of Mean Phase Coherence (MPC) as a function of degree of neurons for incoming (C) and outgoing (D) networks, averaged over 5 degrees. [(E) and (F)] Spike frequencies of different degrees in incoming (E) and outgoing (F) networks, averaged over 5 degrees. Raster plots for incoming [(G) and (I)] and outgoing [(H) and (J)] networks for parameter values indicated on panels (A) and (B) [Points G-J correspond to panels (G)-(J)]. Lower neuron ID means higher degrees and vice versa [see Fig. II.12 (A) and (E) for degrees corresponding to neuron IDs]. Results are averaged over 5 simulations.

We then investigated how the MPC and synchrony forms within the network as a function of degree number of constituent neurons. The histogram of the average MPC constructed as a function of connection number for varying degrees of incoming networks [Fig. II.3(C)] suggests that, for full transmission (p_{trans}=1.0), moderate-degree neurons of incoming networks have higher

average MPC values than low-degree or high-degree neurons. This seems intuitive as the neurons with very few connections do not get enough input to form stable patterns, whereas a few cells with a large number of inputs cannot synchronize with the rest of the population, as their frequency is significantly different due to widely varying number of excitatory inputs [Fig. II.3(E)]. This trend is reversed for higher failure rate (p_{trans}=0.2), with hubs being more coherent than the rest of the network.

Moreover, for p_{trans}=0.6, neurons fire more coherently than when p_{trans}=1.0 for all degrees. This provides evidence that failure can promote more coherent behavior, as the input received by different degrees becomes more uniform with failure.

The same histogram for outgoing networks [Fig. II.2(D)] shows that, for the same p_{trans}, the average MPC values are higher than the incoming case. This is due to a more balanced input levels across the neurons in the network, i.e., a more balanced frequency distribution throughout different degrees [Fig.II.2(F)]. In general, higher-degree neurons have lower average MPC in the outgoing case, and this effect is the most pronounced for higher values of p_{trans}. The example rasterplots of the observed dynamics are presented on figures Fig. II.3(G)-Fig. II.3(J), with the corresponding values of p_{trans} marked on Fig. II.3(A) and (B).

To better assess the specific role of neurons having different degree numbers (i.e. number of connections) on pattern formation, we divided the neurons in each network into 3 groups depending on their total degree (i.e., the sum of their incoming and outgoing connections). The groups were formed so that the total number of the connections in each group is equal. Thus, the number of neurons in each group is inversely proportional to the average degree of individual neurons in the groups, resulting in equal number of connections per group; neurons with degrees less than 24 are in 'Group 1', between 24 and 48 degrees are in 'Group 2' and with more than 48

36

degrees are in 'Group 3'. In terms of number of neurons, the groups consist on average of 533, 342, 125 neurons, respectively. The signals coming through the incoming connections to a given group are tested against different transmission probabilities p_{trans}, while the rest of the connections do not fail at all (p_{trans}=1.0), to see the individual effects of the failure of signals coming to different degrees on overall pattern formation.

In incoming networks, the response of MPC to the network manipulations is generally small. Interestingly we observe that the failing signals coming to Group 1 [Fig. II.4 (A)] and Group2 [Fig. II.4 (B)] result in an overall increase in MPC values of the unaffected groups, with Group 1 having a bigger effect than Group 2. The reason is that preventing lower degree groups from receiving signals make them fire only as a result of Irand, decreasing their overall firing frequency as the synapses fail. Lowering the frequency in these two groups reduced the frequency in all other groups leading to observable increase of coherence.
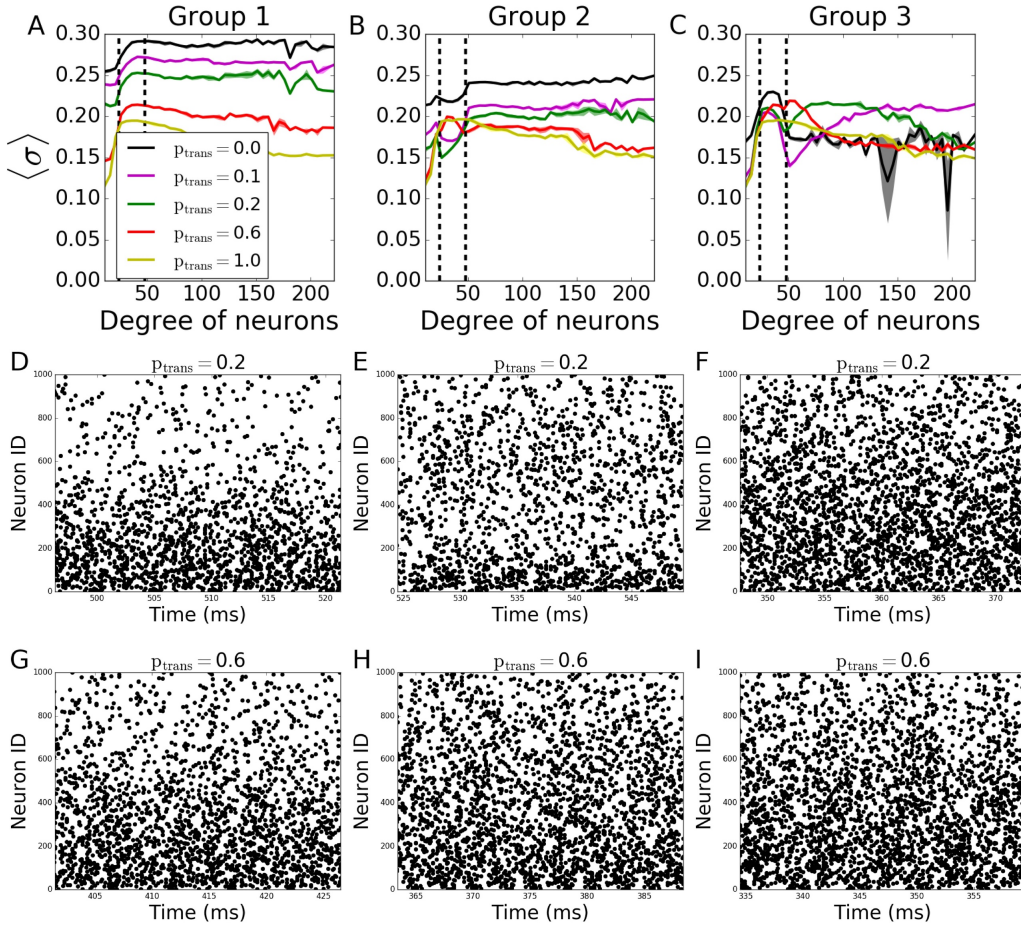
Figure II.4 Nodal contribution to network-wide Mean Phase Coherence (MPC) as a function of its degree for incoming networks. This figure shows an increased coherence of hubs, when they fail to receive signals. Neurons in the network are grouped according to their degrees. Groups are assigned such that neurons in each group has equal total number of connections. Neurons with degrees 1- 23 constitute group 1 [left of the first dashed line in panels (A), (B) and (C)], neurons with degrees 24 -47 constitute group 2 (between dashed lines) and neurons with degrees > 48 constitute group 3 (right of the second dashed line). Signals are transmitted to group 1 (A), group 2 (B) and group 3 (C) with the probability ptrans, while the rest of the network receives signals without failure. Raster plots for the cases in (A), (B) and (C) are shown in (D)-(G), (E)-(H) and (F)-(I), respectively, for two values of ptrans. Lower neuron ID means higher degrees and vice versa [see Fig. II.12 (A) and (E) for degrees corresponding to neuron IDs].

The progressive failure of incoming connections to Group 3 has a more complicated effect.

We observe a higher coherence of that group than the rest of the network for $0.0 < p_{trans} < 1.0$

[Fig.II.4 (C)]. This increase as a function reduction of the transmission probability in the hub group

brings the magnitude of the incoming signal to the hub cells to be similar to that of the intermediate

group, increasing effectively the coherent backbone of the network. For p_{trans}=0.1, we observe that

38

the MPC of hubs are equal and higher than no failure case (p_{trans}=1.0), and this equalizing effect disappears with increasing p_{trans}. This effect is further confirmed through observation which neurons from Group 3 show increased synchronization as a function of increased failure – for lower transmission rates the neurons within that group with higher degrees exhibit increased coherence, whereas for higher transmission the cells with lower degrees show increase of coherence.

In outgoing networks, even moderate increase in failure of Group 1 decreases Group 1 and Group 2's MPC significantly, but hubs (Group 3) are not affected. When p_{trans}=0.0, we observe overall decrease in frequency which leads to increase in reported coherence [Fig. II.5 (A)]. The same holds for the case when Group 2 fails to receive signals [Fig. II.5 (B)]. However, when Group 3 is disconnected, the same reversal effect is observed as in incoming case [Fig. II.5 (C)], but with significantly higher observed changes in MPC. This is again due to the homogenization of the received signals by neurons having different degree. As before, Fig. II.5 (D) - (H) show example raster plots for two transmission values: p_{trans}=0.2 and p_{trans}=1.0 .
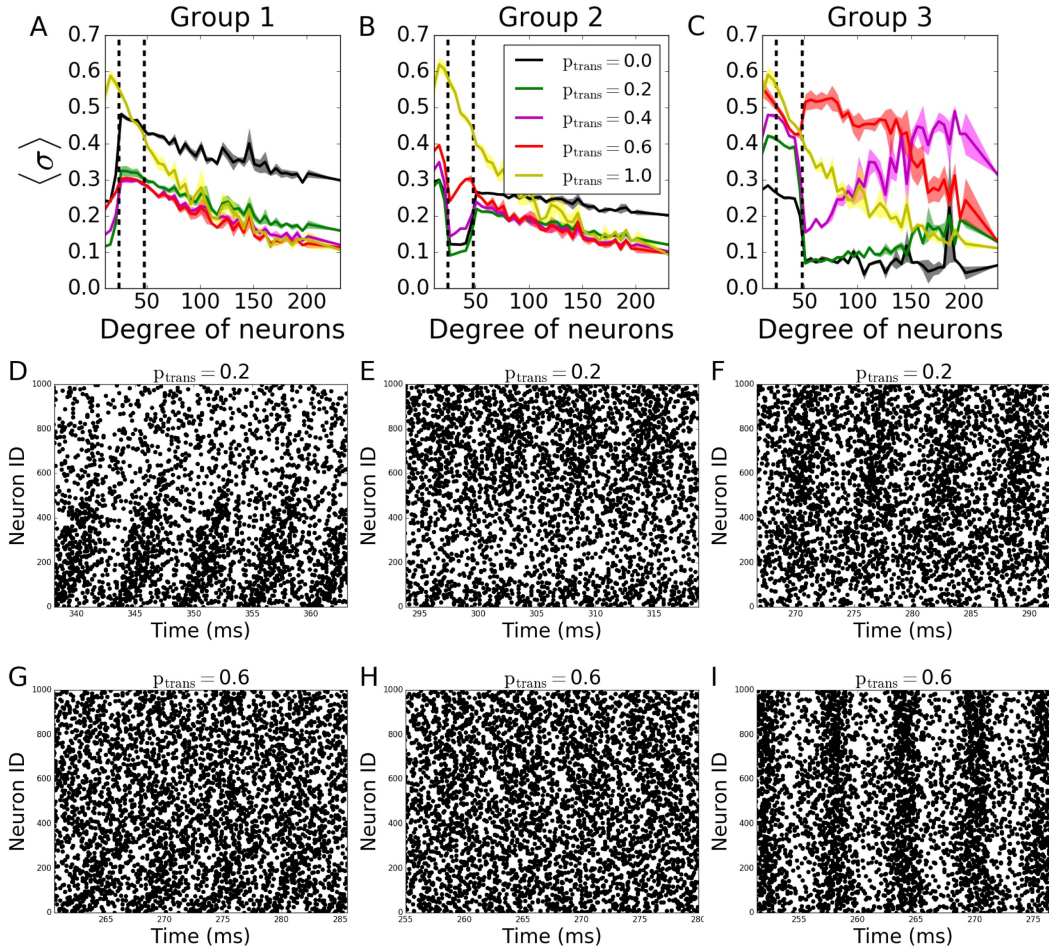
Figure II.5 **Nodal contribution to network-wide Mean Phase Coherence (MPC) as a function of its degree for outgoing networks.** This figure shows an increased coherence of hubs for $p_{trans} \geq 0.4$ than when there's no failure. Neurons in the network are grouped according to their degree. Groups are assigned such that neurons in each group has equal total number of connections. Neurons with degrees 1- 23 constitute group 1 (left of first dashed line in panels (A), (B) and (C)), neurons with degrees 24 -47 constitute group 2 (between dashed lines) and neurons with degrees > 48 constitute group 3 (right of second dashed line). Signals are transmitted to group 1 (A), group 2 (B) and group 3 (C) with the probability p_{trans}, while the rest of the network receive signals without failure. Raster plots for the cases in (A), (B) and (C) are shown in (D)-(G), (E)-(H) and (F)-(I), respectively, for two values of p_{trans}. Lower neuron ID corresponds to cells with higher degrees [see Fig. II.12 (A) and (E) for degrees corresponding to neuron IDs].

2.3.2 Activity – dependent case

The second case we studied is when the transmission probability depends on the spiking history of the postsynaptic neurons, i.e., the signal coming to the postsynaptic neuron, which more recently fired, has a higher chance to fail due to the postsynaptic receptor sensitivity. This case may be biologically more relevant, since it is known that neurodegenerative diseases, such as AD

and Parkinson's, have lower levels of postsynaptic ionotropic receptors [73, 74]. As a result, this may cause a more effective desensitization of the neurotransmitter-gated ion channels in case of higher frequency stimulation via spiking presynaptic neurons [75, 76]. Moreover, higher activity is shown to result in regional vulnerability to amyloid-β deposition in AD, which causes synaptic failure [38].

In this case, we vary two parameters; the base failure probability p_{syn} and failure recovery time constant T. Here, p_{syn}=1 indicates the possibility of complete failure of the synapse. We vary T between 0ms and 5000ms, with p_{syn}=1 and T=5000ms being a disconnected network. As before, we first assessed the overall degree of pattern formation in both types of networks. In incoming networks, we did not see any significant changes in MPC and synchrony for various T and p_{syn} values. However; for outgoing networks, we observed an overall decrease in the network coherence for increasing p_{syn}. For fast synaptic recovery, this decrease is significantly smaller [Fig. II.6 (B) and (D)]. Interestingly, however, for T=0.5ms, we observed a dramatic increase of both MPC and synchrony as p_{syn} tends to unity.
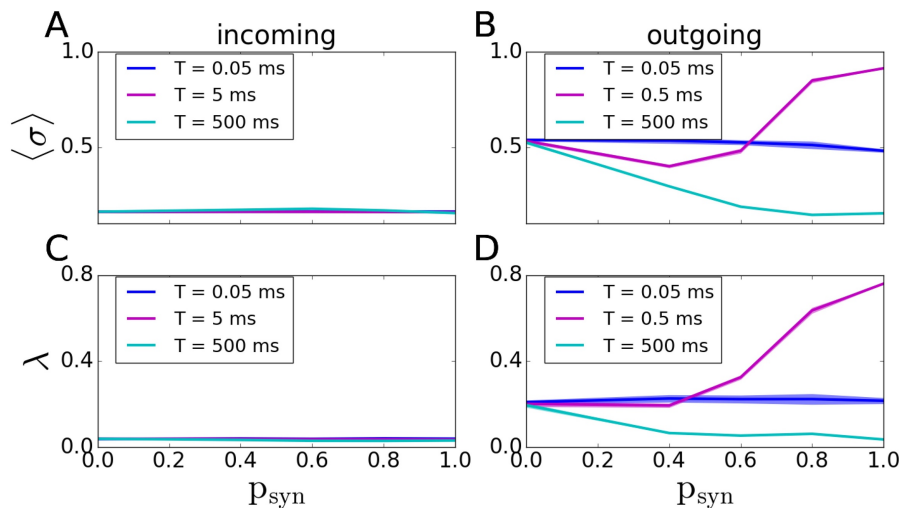
Figure II.6 Pattern formation in the incoming and outgoing networks with activity-dependent synaptic failure. [(A), (B)] MPC and [(C), (D)] synchrony for incoming [(A), (C)] and outgoing [(B), (D)] networks as a function of p_{syn} for three different values of failure recovery time constants T. There is a dramatic increase in MPC and synchrony with increasing synaptic failure (p_{syn}) for a moderate T in outgoing networks.

A more systematic scan of time constants reveals that for incoming networks, the network starts getting disconnected for T>5ms. When T=5000ms, the MPC and synchrony values are the same as activity-independent case, meaning that T is large enough that $p_{trans}\approx1\text{-}p_{syn}$ [Fig. II.7(A), (B); the corresponding raster plots are displayed on panels (C) and (D)].
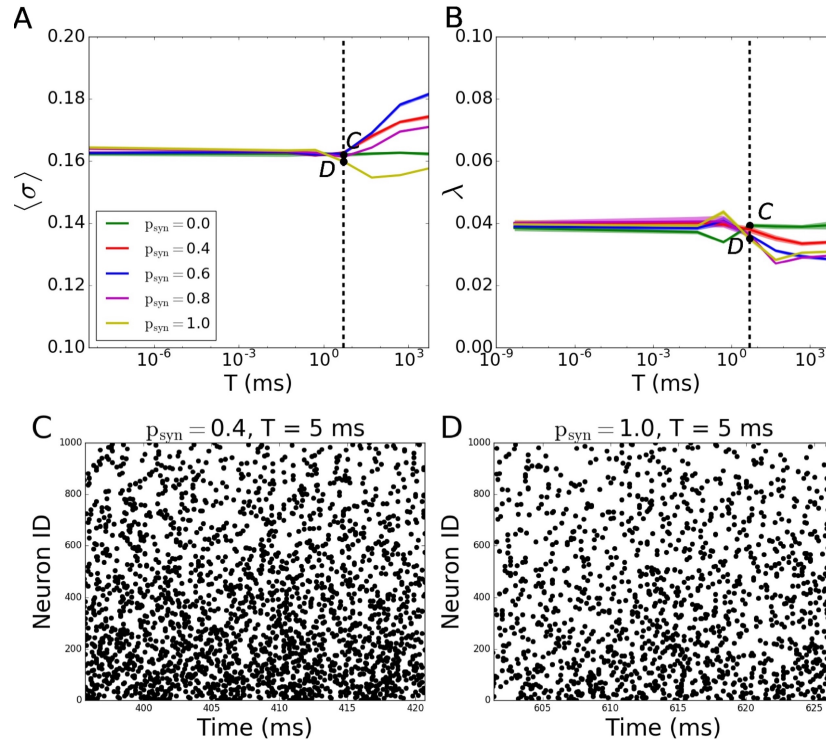
Figure II.7   **Pattern formation in the incoming networks with activity-dependent synaptic failure as a function of failure recovery time constant T.** (A) MPC and (B) synchrony as a function of time constant T for different values of p_{syn}. [(C) and (D)] Raster plots depicting network activity for parameter values marked on [(A) and (B)] [Points C and D correspond to panels (C) and (D)]. The specific parameter values of T and p_{syn} are listed on top of each raster plot. Lower neuron ID corresponds to cells with higher degrees [see Fig. II.12 (A) and (E) for degrees corresponding to neuron IDs].

The behavior of outgoing networks is similar to the one described above except for T=0.5ms, where we observed a large peak in both MPC and synchrony, as p_{syn} tends to one [Fig. II.8(A), (B); raster plots of the observed dynamics are displayed as marked on panels (C)-(F)]. We then have investigated how synaptic failure interacts with neurons with specific nodal degree to form activity pattern within the network (Fig. II.9). For incoming networks and for large T [Fig. II.9(A)-(C)] the degree dependence is largely similar to that of constant p_{trans}, described in the

42

previous section. The group with the largest coherence is the group having intermediate degree values. For small T, as expected, p_{syn} does not influence the overall coherence levels as the transmission probability rapidly recovers and $p_{trans} \approx 1.0$. For larger time constants, the overall level of coherence depends on the p_{syn}, as in the case of activity-independent case [Fig. II.3 (C)]. For a moderate time constant (T=5ms), however, we observe that hubs have higher coherence when $p_{syn} \neq 0.0$ than when $p_{syn}=0.0$, which means that failure of spikes results in a more coherent behavior of hubs, even though globally there's no significant change in the network's MPC. This as driven by synaptic failure capacity to equalize input to the cells across the network.
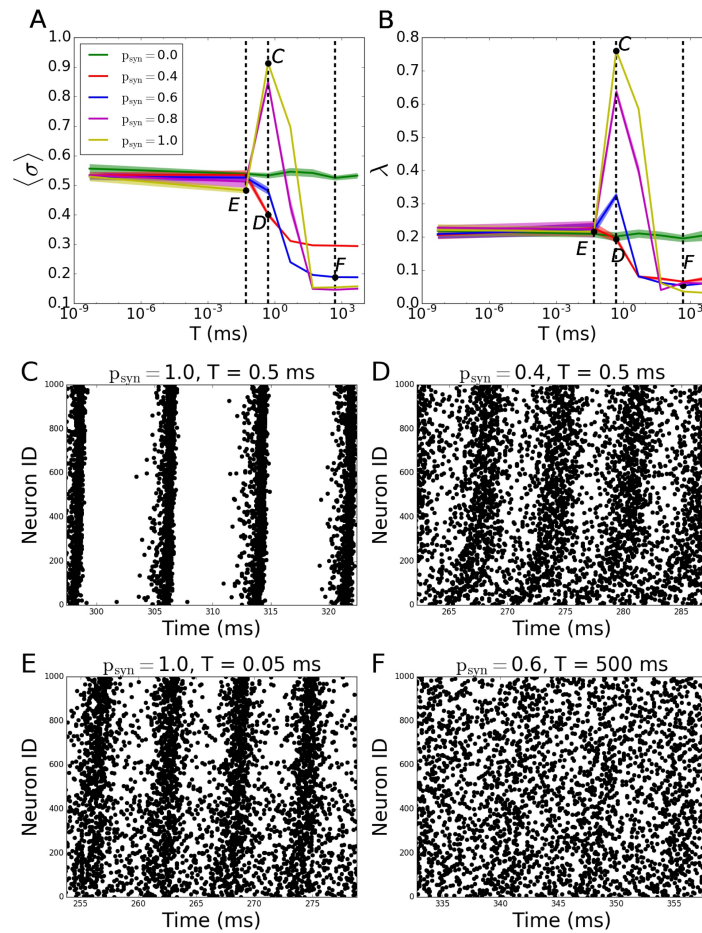
Figure II.8   Pattern formation in the outgoing networks with activity-dependent synaptic failure as a function of failure recovery time constant T. (A) MPC and (B) synchrony as a function of time constant T for different values of p_{syn}. [(C)-(F)] Raster plots depicting network activity for parameter values marked on [(A) and (B)] [Points C-F correspond to panels (C)-(F)]. The specific parameter values of T and p_{syn} are listed on top of each raster plot. Lower neuron ID corresponds to cells with higher degrees.

43
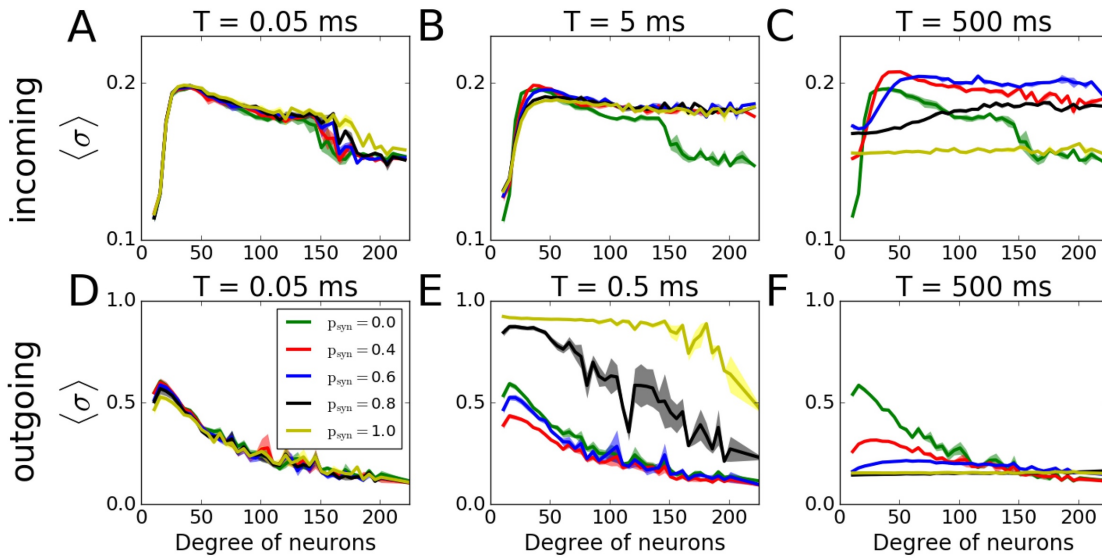
Figure II.9 **Histograms of MPC as a function of degree of neurons of incoming [(A)-(C)] and outgoing [(D)-(F)] networks for varying failure recovery time constants T** (denoted on top of each panel). Participation in pattern formation as a function of nodal degree for activity-dependent transmission failure shows an increased coherence with increased failure for moderate T in both networks.

For outgoing networks, generally the same is true for low and high values of T [Fig. II.9(D), (F)] as in incoming case. However, for the value T=0.5ms [Fig. II.9(E)], we observe a complete reversal of the overall network coherence, with the largest coherence happening for the largest p_{syn} and approaching to one. The MPC is then largely independent of the neuronal degrees, except the highest ones, where MPC starts dropping. To understand the reason behind this sudden increase, we measured the average number of signals transmitted to each neuron as a function of its incoming degree. The histograms (Fig. II.10) suggest, that for low T, for both incoming and outgoing networks, there is a linear proportionality between the input and the incoming degree number [Fig. II.10(A), (D)]. For larger values of T, the signal curves depend directly on the value of p_{syn} and for large p_{syn} they saturate for large degree values [Fig. II.10(B), (C), (E), (F)], making the amount of signal received by neurons largely independent of degree. However, only for outgoing networks and T=0.5ms, all neurons, independent from their incoming degrees, receive

44

the same number of the signals, which is significantly different from zero [Fig. II.10(E)]. This suggest that at this specific T range, all cells in the network receive about the same input magnitude allowing them to synchronize across the entire system.
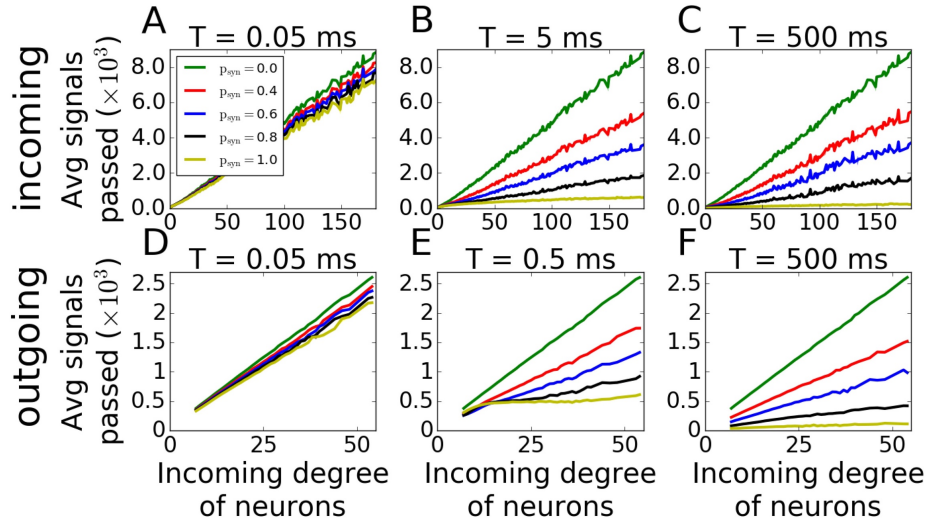
Figure II.10 Average input magnitude to a neuron as a function of nodal degree for activity-dependent synaptic failure. Histograms of average number of signals transmitted as a function of incoming degree of neurons of incoming [(A)-(C)] and outgoing [(D)-(F)] networks for varying failure recovery time constants T (denoted on top of each panel) show that for T=0.5ms and p_{syn}=1.0, outgoing networks receive the same amount of signals, independent from their degrees.

To see if similar results would be observed with different connectivities and direction ratios, we simulated various connectivity fractions and direction ratios for different time constants (T=0.05,5,500ms for incoming networks and T=0.05,0.5,500ms for outgoing networks). In incoming case, the reversal effect of MPC increase of hubs for higher p_{syn} at a moderate time constant (T=5ms) is not observed for lower or higher connectivities (Supplementary Figure 2.2). However, increasing direction ratio makes this effect more pronounced, since increasing outgoing connections at hubs makes the network more balanced overall (Supplementary Figure 2.3). In outgoing networks, this dramatic increase of overall coherence is still observed, and it is more pronounced for higher connectivities (Supplementary Figure 2.4) and lower direction ratios

(Supplementary Figure 2.5), since the amount of outgoing connections from hubs is increased in both cases, resulting in a more coherent network overall.

Lastly, we included inhibitory neurons to the network, since they are known to have significant effects on pattern formation in cortical networks [77]. We simulated outgoing networks with an inhibitory population for T=0.5ms and various p_{syn}. Our results (Fig.II.11) suggest that there's still that reversal effect as we've seen in [Fig. II.9(E)], i.e. increasing p_{syn} eventually increases the overall network coherence, when p_{syn} approaches to 1.
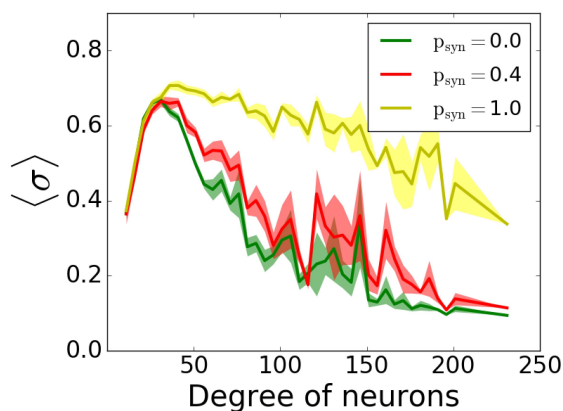
Figure II.11 Participation in pattern formation as a function of nodal degree for activity-dependent transmission failure for mixed excitatory-inhibitory networks. Histograms of MPC as a function of degree of neurons for T=0.5ms and varying p_{syn} levels show emergence of highly synchronous state for high p_{syn} values. The network is composed of 1000 excitatory and 1000 inhibitory neurons. Excitatory neurons are wired as outgoing scale-free networks, while inhibitory neurons have random connections to both inhibitory and excitatory population with the same connectivity as the one within excitatory population (1.6%).

2.4 Discussion

. In this chapter, we systematically analyzed how synaptic failure affects two complementary scale-free network structures, namely incoming and outgoing. We studied the cases when synaptic transmission probability was activity-independent and when it was activity-dependent. In the first case, we have found that targeted synaptic failure to a neuronal population having different nodal degrees has differential effects on pattern formation in the network. When synaptic failure was activity dependent, we observed that structural features of networks do not

map onto functional connectivity (Fig.II.12), but rather, synaptic failure may result in differential spatio-temporal patterning dependent on the failure recovery time constant T and the base failure probability p_{syn}. Moreover, the two network structures, incoming and outgoing, behave differently, with outgoing networks displaying overall a larger degree of coherence/synchrony and a higher dependence on transmission probability. This is especially evident for the activity-dependent transmission probability, where the outgoing networks exhibit an increased level of coherence for a large base failure probability (p_{syn}) for a specific value of the failure recovery time constant (T=0.5ms).
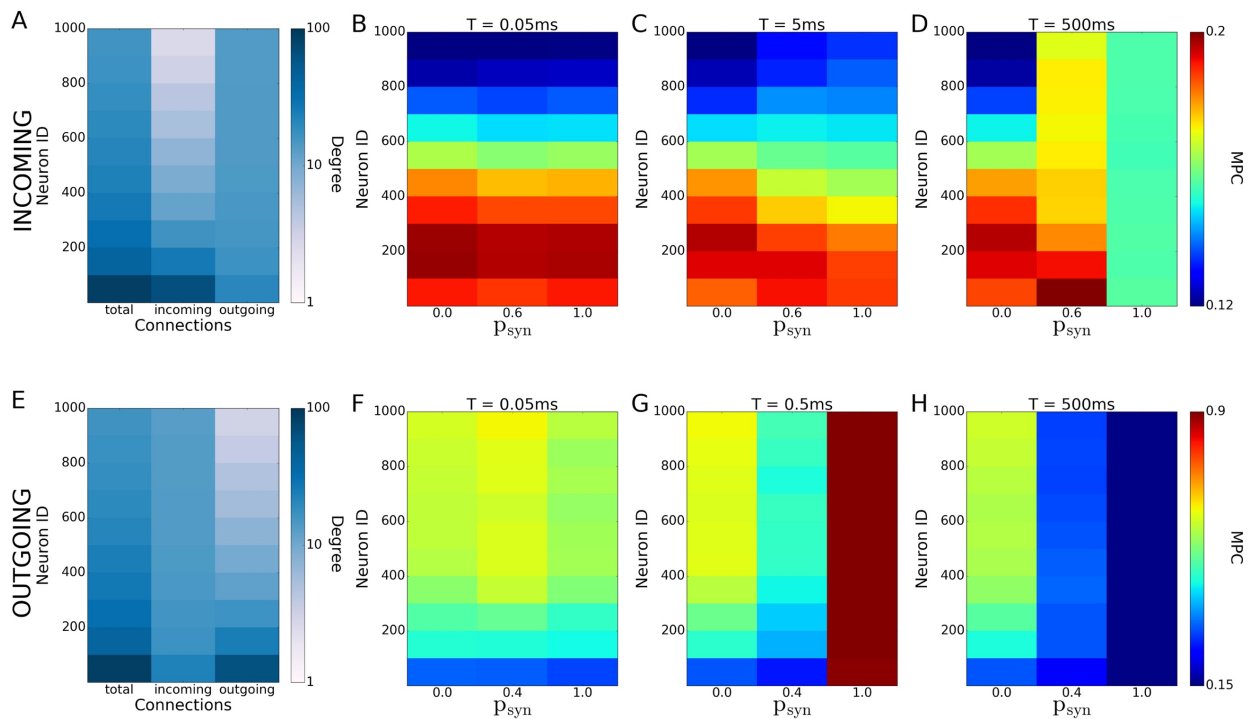
Figure II.12 Emergence of coherence patterns in scale-free networks. Heatmaps of degrees [(A) and (E)] and MPC [(B)-(D) and (F)-(H)] for incoming [(A)-(D)] and outgoing [(E)-(H)] networks show dependence of network-wide pattern formation on parameters of activity-dependent synaptic failure (T and p_{syn}). Each color is an average of the values for 100 neurons.

This abrupt increase in synchrony and coherence as a result of synaptic failure is unexpected and paints a more complex picture of possible network interactions in the brain. It was hypothesized that anesthetics act predominantly on the network hubs and overall decrease the level

of coherence across brain networks, leading to the loss of consciousness[41]. Similarly, hubs are shown to be more vulnerable to amyloid deposition due to their high activity rate, causing the disruption of large-scale coherence in the brain and eventually AD [30]. In addition, numerical studies on scale-free networks suggest that they are robust against the random removal of nodes and the change in their synchronization process is insignificant in cases when 5% of their total nodes are randomly removed. However, when hubs are targeted, only the removal of 1% of the total nodes is enough to divide the network into subnetworks and to disrupt network synchronization [6, 78-80]. We show, however, that depending on the network type, preferential deactivation of hubs and activity-dependent degeneration might lead to increased phase coherence and synchrony. Further investigation on human brain networks may be necessary to determine whether a phase of overall increased coherence occurs before the decrease of large-scale coherence in such cases as application of anesthetics or AD. That may be a useful biomarker for AD as well as a significant contribution to explain the impact on anesthetics on the human brain.

Chapter III

Contrasting Mechanisms for Hidden Hearing Loss: Synaptopathy vs Myelin Defects

3.1 Introduction

Hidden hearing loss (HHL) is an auditory neuropathy characterized by normal hearing thresholds but reduced amplitude of the sound-evoked auditory nerve compound action potential (CAP) [59]. It has been proposed that in humans HHL leads to speech discrimination and intelligibility deficits, particularly in noisy environments [59]. Animal models originally indicated that HHL can be caused by moderate noise exposures [62] or aging [45], and that loss of inner hair cell (IHC) synapses could be its cause [43]. A recent study provided evidence that transient loss of cochlear Schwann cells, that provide myelination of auditory nerve fibers, also causes permanent auditory deficits in mice which have characteristics of HHL [63]. Histological analysis of the cochlea after auditory nerve remyelination showed a permanent disruption of the myelination patterns at the heminode of type I spiral ganglion neuron (SGN) peripheral terminals, suggesting that this defect could be contributing to HHL. To shed light on the mechanisms of different HHL scenarios observed in animals and to test their impact on type I SGN activity, we constructed a reduced biophysical model for a population of SGN peripheral axons. We found that, similar to experimental results (Fig III.1A-C), the amplitudes of simulated sound-evoked SGN

49

CAPs are lower and have greater latencies when the heminodes are disorganized, i.e. they are placed at different distances from the hair cell rather than at the same distance as seen in the normal cochlea. Thus, our model confirms that disruption of the position of the heminode causes desynchronization of SGN spikes leading to a loss of temporal resolution and reduction of the sound-evoked SGN CAP. We also simulated synaptopathy by removing high threshold IHC-SGN synapses and found that the amplitude of simulated sound-evoked SGN CAPs decreases while latencies remain unchanged, corresponding to what has been observed in noise exposed animals (Fig III.1A). This model can be used to further study the effects of synaptopathy or demyelination on auditory function. Work presented here is currently submitted to *PLOS Computational Biology*.
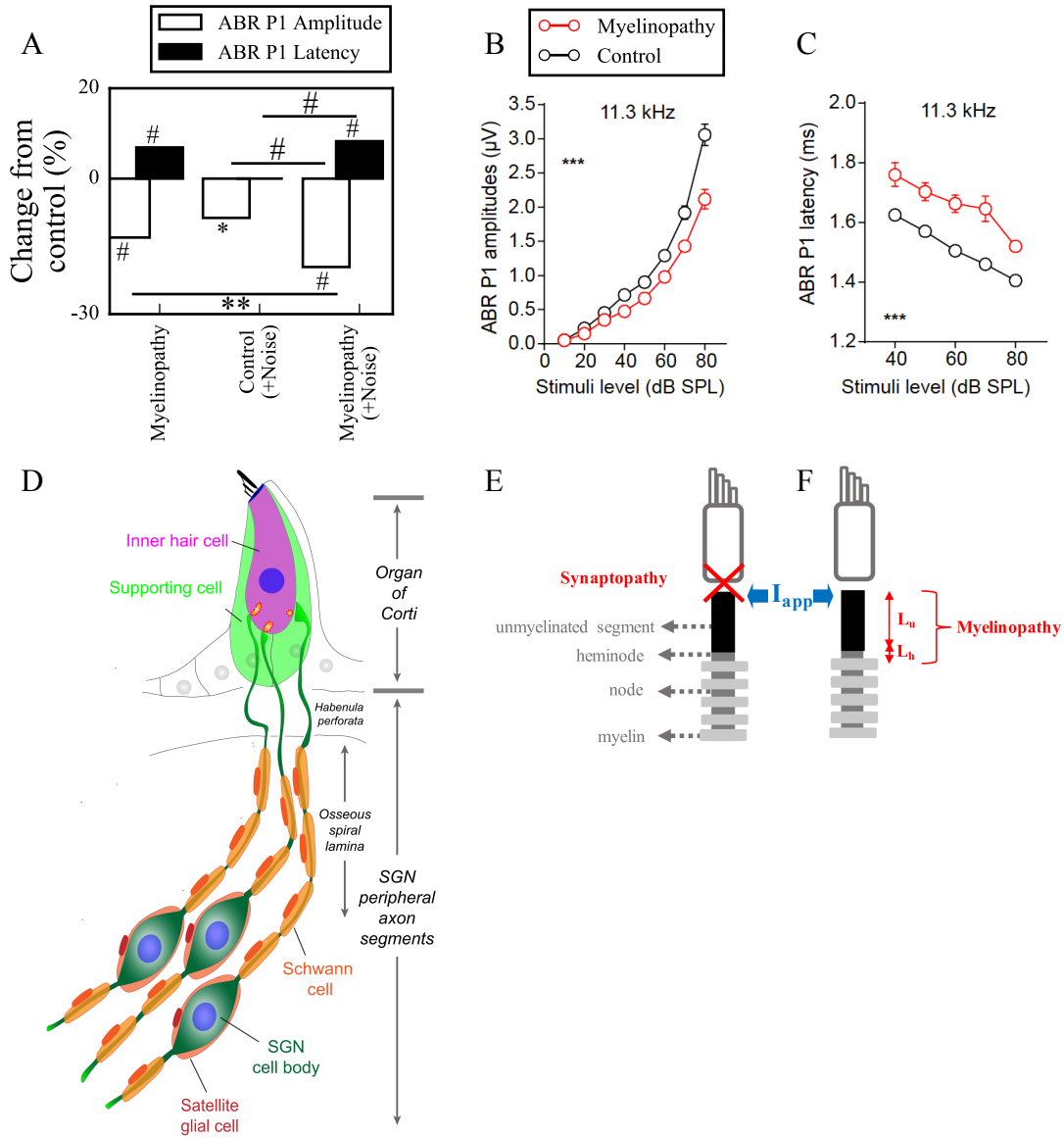
Figure III.1 Mechanisms of hidden hearing loss. (A) Experimental results suggests that different mechanisms of HHL, myelinopathy and noise exposure resulting in synaptopathy, affects ABR P1 in distinct ways: Myelinopathy increases ABR P1 latency and decreases ABR P1 amplitude, while synaptopathy decreases ABR P1 amplitude only, without any change in latency (data taken from [63]; *p<0.05, **p<0.01, #p<0.001). Figures in panels (B) and (C) taken from [63] shows ABR P1 measures evoked by 11.3kHz sound stimuli with various sound levels for control and myelinopathy cases. The decrease in ABR P1 amplitude (B) in case of myelinopathy is more pronounced for higher sound levels, whereas ABR P1 latencies (C) are increased for all sound levels. (D) Schematic illustration of type I SGNs, bipolar neurons innervating IHCs via myelinated peripheral projections. (E, F) Model peripheral fibers of type I SGNs (SGN fiber) consist of an unmyelinated segment at the peripheral end adjacent to the site of IHC synapses, followed by a heminode and 5 myelin sheaths with 4 nodes between them. Two mechanisms of hidden hearing loss are simulated: (E) synaptopathy, modeled by removing IHC-AN synapses, and (F) myelinopathy, modeled by varying the lengths of the unmyelinated segment (L_u) or the heminode (L_h).

3.2 Methods

3.2.1 SGN fiber model

Type I SGNs are bipolar neurons with peripheral axon segments innervating IHCs and central axon segments projecting into the cochlear nucleus (Fig III.1D) [81]. In this study, a compartmental model of peripheral axons of type I SGNs was constructed using the NEURON simulator (version 7.6.2, [82]) as schematized in Figs III.1E and F. For simplicity, we refer to peripheral axons of type I SGNs as SGN fibers, throughout the chapter. Each fiber consists of an unmyelinated segment (length L_u), a heminode (length L_h) and 5 myelin sheaths following the heminode, separated by 4 nodes [83, 84]. Each compartment has passive membrane properties described by specific capacitance (C_m) and specific membrane resistance (R_m). Specific cytoplasmic resistance (R_a) between each consecutive compartment was modified to obtain the speed of the action potential as 12-14m/s [85], based on the neural conduction velocity measurements of human auditory nerve [86]. Sodium and potassium channels were inserted along the SGN fibers, except the myelin sheaths, which only had passive membrane properties. The nominal conductances of both channel types at the unmyelinated segment was 15 times less than the nodes and the heminode [84], therefore action potential was initiated first at the heminode. The parameters for channel dynamics were taken from [85] (see Section 3.5), the stochastic channels in [85] were converted into deterministic ones for simplicity. This was done by multiplying channel density with the single ion channel conductance to obtain deterministic conductance values (see Table 3.1 for all parameters). The Nernst potentials for the ions Na^+ (E_{Na}) and K^+ (E_K) were set to 66 and -88 mV, respectively, and the resting potential (E_{Rest}) was -78 mV [87]. Simulations were done at 37℃. The differential equations were solved by fully implicit backward

Euler method with time step 5µs implemented in the NEURON simulation environment (see Section 3.5).

Table III-1   Morphological, electrical and ion channel parameters of the different parts of a normal SGN fiber. Values as in [84] except for R_a and myelinated segment length which were modified for human SGN fibers.

Parameters	Unmyelinated segment	Heminode	Myelin	Node
Length (µm)	10	1	40 [modified]	1
Diameter (µm)	1.2	1.2	2.2	1.2
g_{Na} (S/cm^2)	0.01208	0.1812	0	0.1812
g_K (S/cm^2)	0.015	0.225	0	0.225
R_m (ohm-cm^2)	1662	1662	1300000	1662
C (µF/cm^2)	0.05125	0.05125	0.0012	0.05125
R_a (ohm-cm)	8291.4 [modified]			

g_{Na}, maximal sodium conductance; g_K, maximal potassium conductance; R_m, specific membrane resistance; C, specific capacitance; R_a, specific cytoplasmic resistance.

3.2.2 Sound representation

We used a previously developed, well-accepted computational model [52, 88, 89] of the auditory periphery to simulate IHC-SGN synaptic release probabilities. This model takes a sound wave as an input and simulates the response of various parts of the ear (from the middle ear to SGNs) to this sound wave. The model as described in [52] is summarized next. A second-order linear bandpass Butterworth filter with cutoffs 22kHz and 12.5kHz was used to model the response of the middle ear to sound and output stapes velocity. To simulate basilar membrane (BM) velocity in response to stapes movement, a dual-resonance-nonlinear filter bank model was used [52]. BM motion results in the displacement of the IHC cilia, which was approximated as

$$\tau_C \frac{du(t)}{dt} + u(t) = \tau_C C_{cilia} v(t), \tag{3.1}$$

where $u(t)$ is the displacement of the IHC cilia, $v(t)$ is the BM velocity, C_{cilia} and τ_C represent the gain factor and the time constant for the cilia displacement, respectively. The IHC cilia displacement changes the fraction of open ion channels at the IHC apical membrane, resulting in apical conductance change, which was modelled as a three-state Boltzmann distribution as

$$G(u) = G_{cilia}^{max}\left[1 + \exp\left(-\frac{u(t)-u_0}{s_0}\right) \times \left[1 + \exp\left(-\frac{u(t)-u_1}{s_1}\right)\right]\right]^{-1} + G_a, \tag{3.2}$$

where $G(u)$ is the apical conductance, G_{cilia}^{max} is the maximum apical conductance and G_a is the passive conductance of the apical membrane. u_0, s_0, u_1 and s_1 are constants to model the nonlinearity of the proportion of open channels [52]. The voltage of an IHC depends on its apical conductance, which was modeled as

$$C_m\frac{dV(t)}{dt} + G(u)(V(t) - E_t) + G_k(V(t) - E_k') = 0, \tag{3.3}$$

where $V(t)$ is the IHC potential, C_m is the IHC membrane capacitance, G_k is the passive basolateral membrane conductance and E_t is the endocochlear potential. E_k' is the reversal potential of the basal current E_k, which can be described as $E_k' = E_k + E_tR_p/(R_p + R_t)$, where R_p and R_t are the resistances of the supporting cells.

IHC depolarization opens the calcium channels near the synapse, resulting in the change of calcium current (I_{Ca}), which was described as

$$I_{Ca}(t) = -G_{Ca}^{max}m_{I_{Ca}}^3(t)(V(t) - E_{Ca}), \tag{3.4}$$

where G_{Ca}^{max} is the maximum calcium conductance near the synapse and E_{Ca} is the reversal potential of calcium. $m_{I_{Ca}}$ is the fraction of the open calcium channels, which depend on the IHC potential, given by

$$\tau_{I_{Ca}}\frac{dm_{I_{Ca}}(t)}{dt} + m_{I_{Ca}}(t) = m_{I_{Ca},\infty}, \tag{3.5}$$

where

$$m_{I_{Ca},\infty} = [1 + \beta_{Ca}^{-1}\exp{(-\gamma_{Ca}V(t))}]^{-1}. \tag{3.6}$$

Here, $\tau_{I_{Ca}}$ is calcium current time constant, $m_{I_{Ca},\infty}$ is the steady state fraction of the open calcium channels, β_{Ca} and γ_{Ca} are constants to model experimental calcium current properties.

Calcium current (I_{Ca}) changes the concentration of the calcium ion ($[Ca^{2+}]$) near the synapse of the IHCs, which was modeled as

$$\frac{d[Ca^{2+}](t)}{dt} = I_{Ca}(t) - [Ca^{2+}](t)/\tau_{[Ca]}, \tag{3.7}$$

where $\tau_{[Ca]}$ is calcium concentration time constant. Since calcium ions near the synapse trigger neurotransmitter release from IHCs, calcium concentration ($[Ca^{2+}]$) affects the transmitter release rate, $k(t)$, such that:

$$k(t) = \max\left(([Ca^{2+}]^3(t) - [Ca^{2+}]^3_{thr})z, 0\right), \tag{3.8}$$

where $[Ca^{2+}]_{thr}$ is the minimum calcium concentration required for a release and z is a constant to obtain release rates from calcium concentration.

The model for the IHC synapse consists of three pools of neurotransmitter vesicles, a cleft (c), an immediate store (q) and a reprocessing store (w). The number of vesicles at each pool was described as

$$\frac{dq(t)}{dt} = N(w(t), x) + N([M - q(t)], y) - N\big(q(t), k(t)\big), \tag{3.9}$$

$$\frac{dc(t)}{dt} = N\big(q(t), k(t)\big) - lc(t) - rc(t), \tag{3.10}$$

$$\frac{dw(t)}{dt} = rc(t) - N(w(t), x). \tag{3.11}$$

These equations dictate that vesicle release occurs from the immediate store (q) to the cleft (c) at a rate $k(t)$. The vesicles in the cleft are either lost from the synapse at a rate l, or IHCs can take them back to the reprocessing (w) store at a rate r, where the neurotransmitters are repackaged into vesicles to be released. Then, the repackaged vesicles are transferred to the immediate store at a

rate *x*. *M* in Eq. 3.9 represents the maximum number of vesicles that can be contained at the immediate store, which receives new vesicles at a rate *y[M-q(t)]*. Here, the rate of the transfer of vesicles from the reprocessing store to the immediate store (*x*) and the rate immediate store receives new vesicles (*y*) are constants taken from [88, 89].

In this IHC synapse model, vesicles in the cleft and the reprocessing store are continuous quantities, whereas the immediate store has quantal vesicles, whose release is a stochastic process. This process is described by the function *N(n, ρ)*, which means that there are *n* vesicles, each of which have a release probability of *ρdt* at a single time step *dt*. As a result, we take the term *N(q(t), k(t))* as an output of this model, which gives us the release rate, i.e. the release probability from IHCs. In our model, we used the excitation protocol from [61] and applied 10kHz 5 ms long sound stimuli. As a result, we simulated the stimulus mediated release probabilities expected from that excitation (Fig. III.2A). We used the same parameters as in [88, 89], except for those listed in Table 2, in order to obtain release rates similar to the experimental results as in Fig III.3 in [52].

Table III-2 Parameters for the model of middle ear-IHC synapse, changed from [88, 89]

Parameters	LT	MT	HT
Order of the linear gammatone filters	3	3	1
G_{Ca}^{max}(nS)	4	3	2

G_{Ca}^{max}, maximum calcium conductance near the IHC synapse; LT, low threshold fiber; MT, medium threshold fiber; HT, high threshold fiber.
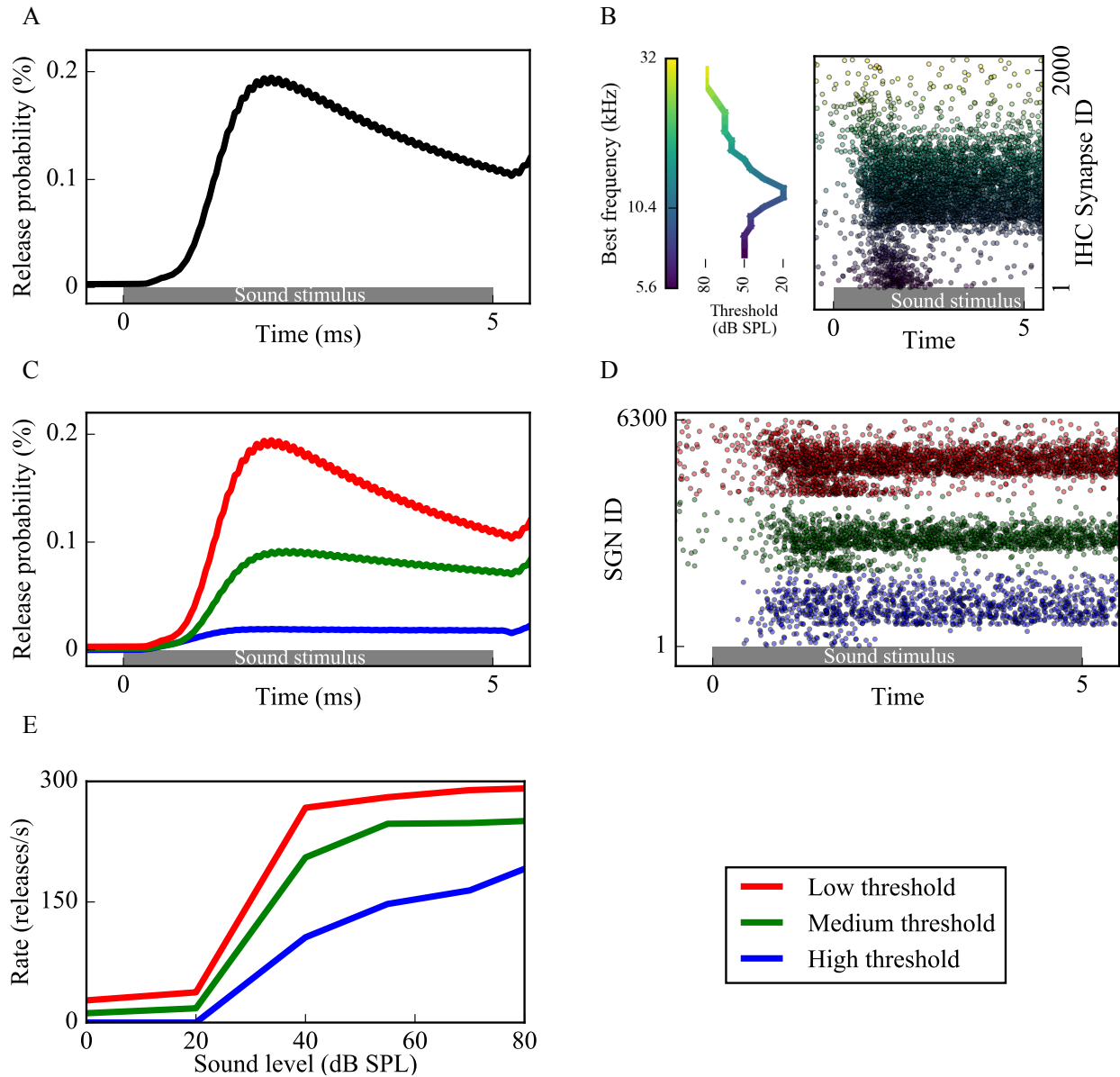
Figure III.2 Sound-evoked activity of low, medium and high threshold SGN fibers results from increased vesicle release probabilities from corresponding IHC-SGN synapses. (A) Sound stimuli results in an increased vesicle release probability from IHCs (as computed using the coupled Eqs. (3.1-3.11)) and release times as determined by a Poisson process. (B) Cumulative release events of an IHC synapse population with best frequencies between 5.6kHz-32kHz in response to a 10kHz sound stimuli. The dots, color coded based on the BFs of the synapses, represent release times of each IHC synapse in a population defined as different IHC synapse IDs. Since the thresholds of IHCs depend on their BFs, each population has different release patterns. For each release event, the corresponding SGN fiber is stimulated with a brief external current pulse, resulting in spiking activity. (C) Three groups of SGN fibers, low (LT), medium (MT) and high (HT) threshold, were simulated based on their spontaneous firing rates and saturation profiles in response to sound. (D) Based on the release probabilities, different fiber types exhibit different cumulative responses (red dots: low threshold, green dots: medium threshold, blue dots: high threshold). Panels A-D are example simulations for simulated 80dB SPL 10kHz sound stimuli. (E) The trend of spike rates of each fiber type for various sound levels in our model are comparable to Fig 3 of [52].

The output of the IHC synapse model is IHC-SGN synaptic release probabilities (Fig III.2A), which were used to determine a Poisson process of IHC release (Fig III.2B) that governed brief external stimuli to the corresponding nerve fiber to induce action potential generation. The external stimuli mimicking synaptic release from IHCs [90] were simulated in the form of external current pulses I_{app}, expressed as

$$I_{app} = 0.19A(e^{-\frac{t}{\tau_2}} - e^{-\frac{t}{\tau_1}})(V_m - E_{exp}) \tag{3.12}$$

where A=0.1nS, τ_1=0.3ms, τ_2=0.5ms and E_{exp}=0mV, unless otherwise stated (Supplementary Figure 3.3 and Supplementary Figure 3.4A). I_{app} is applied at the beginning of the unmyelinated segment (Fig III.1E and F) and the time of the action potential at the center of the heminode was taken as output (Fig III.2D).

3.2.3 Defining different fiber types

SGNs can be classified into 3 groups depending on their spontaneous firing properties, thresholds for sound-evoked activity and saturation profiles, namely low threshold (LT), medium threshold (MT) and high threshold (HT) fibers. Based on the measurements reported in [53], we modeled the properties of these three fiber groups as follows (Figs III.2C-E): LT fibers have high spontaneous rates (18-100 spikes/s), low dynamic ranges, and reach their maximum discharge rate within approximately 30 dB sound pressure level (SPL). MT fibers have lower spontaneous firing (between 0.5 and 18 spikes/s), higher dynamic ranges, and show slower increase and saturation of spike rates with increasing SPL compared to LT fibers. HT fibers have very low spontaneous firing rates (<0.5 spikes/s), and response thresholds higher than ~20 dB SPL. For higher SPL, their spike rate increases linearly with sound intensity, therefore their dynamic range is the highest [53]. To simulate these different fibers, we varied $[Ca^{2+}]_{thr}$ and G_{Ca}^{max} of the IHC synapses of each fiber type (see [88, 89] and Table 3.2). In our model, we had IHC synapses with 21 characteristic

frequencies varying logarithmically between 5.6kHz and 32kHz to simulate experimental data [61]. For each characteristic frequency, we used 100 LT, 100 MT and 100 HT fibers, 6300 fibers in total.

3.2.4 Analyzing spike trains obtained from simulations

In response to simulated sound stimulus, each model SGN fiber fires a sequence of spikes (Fig III.2D). We used three methods to analyze SGN fiber spike trains:

3.2.4.1Measurement of time intervals between non-identical spike trains of SGN fiber populations

This metric, modified from a shuffled autocorrelogram measure in [91], was used to quantify temporal properties of SGN fiber spiking within a population based on the time intervals of the spikes between each non-identical pair of spike trains within the population. From all possible non-identical pairs of spike trains within a population, forward time intervals were measured between each spike i of the first spike train and spikes of the second spike train falling between the i-th and (i+1)-st spikes (Fig III.3A). All time intervals from all pairs were tallied in a histogram and the histogram was reflected over y-axis, since each forward time interval of a pair (a,b) is a backward time interval of the pair (b,a).
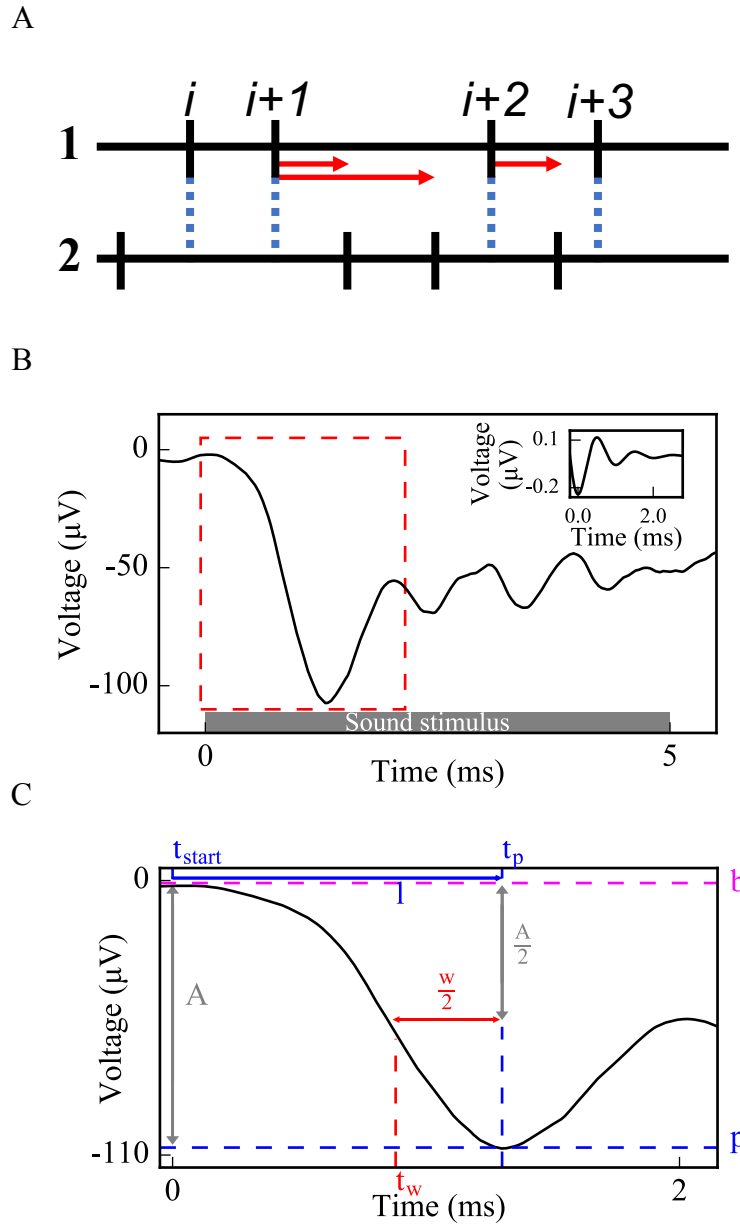
Figure III.3 Methods used to evaluate cumulative activity of SGN fiber populations: pairwise spike time differences (A) and simulated CAP (B,C). (A) For each non-identical pair of spike trains from an SGN fiber population, forward time intervals are measured between each spike i of the spike train 1 and all spikes of the spike train 2 falling between i and i+1. Standard deviations of the distributions of these time intervals are calculated to evaluate synchronous spike timing in the SGN fiber population. (B) Each spike in Fig III.2D is convolved with the unitary response of CAP [the inset of (B)] and convolutions from each spike are summed up to obtain a simulated CAP of the SGN fiber population. (C) Amplitude, latency and width are measured from the first peak of the simulated CAP [dashed rectangle in (B) is zoomed in for (C)] (b: baseline, p: peak, A: amplitude of the peak, t_p: peak time, l: latency, w: width, t_w: half amplitude time before t_p).

3.2.4.2 Convolution into the unitary response of compound action potential (CAP)

To yield a cumulative response of the activity of the population of SGN fibers and to be able to compare model results with in vivo ABR P1 results, we convolved each spike with the unitary response and summed them up to generate a population CAP (Fig III.3B). In this study, we considered this computed CAP as equivalent to ABR P1. The unitary response U(t) was described as in [92]:

$$U(t) = \begin{cases} A \times e^{-k(t-0.288)} \times \sin\left(2\pi f(t-0.288)\right) & \text{for } -0.215 \le t \le 2.785 \\ 0 & \text{otherwise} \end{cases} \quad (3.13)$$

where $A = 0.16\mu V$, $k = 1.44ms^{-1}$, $f = 0.994ms^{-1}$ and t is the time (Fig III.3B inset).

Fifty population CAPs were averaged to measure the width (w), amplitude (a) and latency (w) of the initial CAP peak more accurately, which were computed as:

$$a = |p - b| \quad (3.14)$$

$$l = t_p - t_{start} \quad (3.15)$$

$$w = 2(t_w - t_p) \quad (3.16)$$

where p is the peak voltage, b is the baseline voltage, t_p is the time when the voltage equals p, and t_w is the time when the voltage equals $-\left(|b| + \frac{a}{2}\right)$ (the half-peak) before t_p (Fig III.3C).

3.2.4.3 Calculating spike probability and latency for each SGN fiber population.

The probability that release events at IHC-SGN synapses resulted in spikes at the heminodes of an SGN fiber population was calculated by dividing the number of spikes at the heminode of each SGN fiber by the number of release events and averaging over all fibers within a population. Spike latency of an SGN fiber population was calculated by the time difference between a spike and a release preceding that spike averaged over all spikes of that population.

61

3.3 Results

Using the model of the type I SGN fiber population, we investigated the effects of myelinopathy and synaptopathy on type I SGN spike generation and spike timing. We first simulated different myelinopathy scenarios by varying the length of the initial unmyelinated segment L_u (Fig III.1F, from a putative control value of 9 µm) and the first heminode length L_h (from a control value of 1 µm) for all (i.e. LT, MT and HT) fibers. Next, we simulated synaptopathy by removing IHC-SGN synapses (Fig III.1E) considering the cases where only synapses on HT fibers are affected or synapses on all fiber types are affected. Lastly, we investigated the combined effects of myelinopathy and synaptopathy.

3.3.1 Effects of myelinopathy on SGN population activation patterns

Mouse studies have shown that transient demyelination and the subsequent remyelination alters the position of SGN heminodes, resulting in heminodes that are positioned farther from the IHC-SGN synapse and at variable positions, in contrast to healthy SGN fibers where heminodes on all fibers are aligned [61]. To identify the effect of this heterogeneity of heminode locations on SGN spike timing, we first considered a population of fibers with different ranges of L_u values stimulated with identical IHC release patterns (Fig III.4). Here, we denote 0% increase as the putative control fiber length (L_u=9 µm), while 100% increase means L_u was varied between 9 and 18 µm uniformly across the population. We assessed the level of synchronization of spikes across the SGN fiber population by stimulating all fibers with an identical randomly determined IHC release pattern. As heterogeneity of L_u values was increased (Fig III.4A), the population spike rate decreased reflecting spike generation failure on fibers with large L_u. At the same time, variability in spike timing increased as illustrated in spike raster plots (Figs III.4B, D, F, H show a portion of the generated spike trains, insets show timing of first spikes) and computed pairwise spike time

intervals (Figs III.4C, E, G, I, see Methods). These disruptions in spike generation and timing resulted in increased standard deviation of the distribution of pairwise spike time differences across the population (Fig III.4A). These initial observations suggest that myelinopathy not only disrupts spike timing of SGNs within a population, but also leads to the loss of spikes.
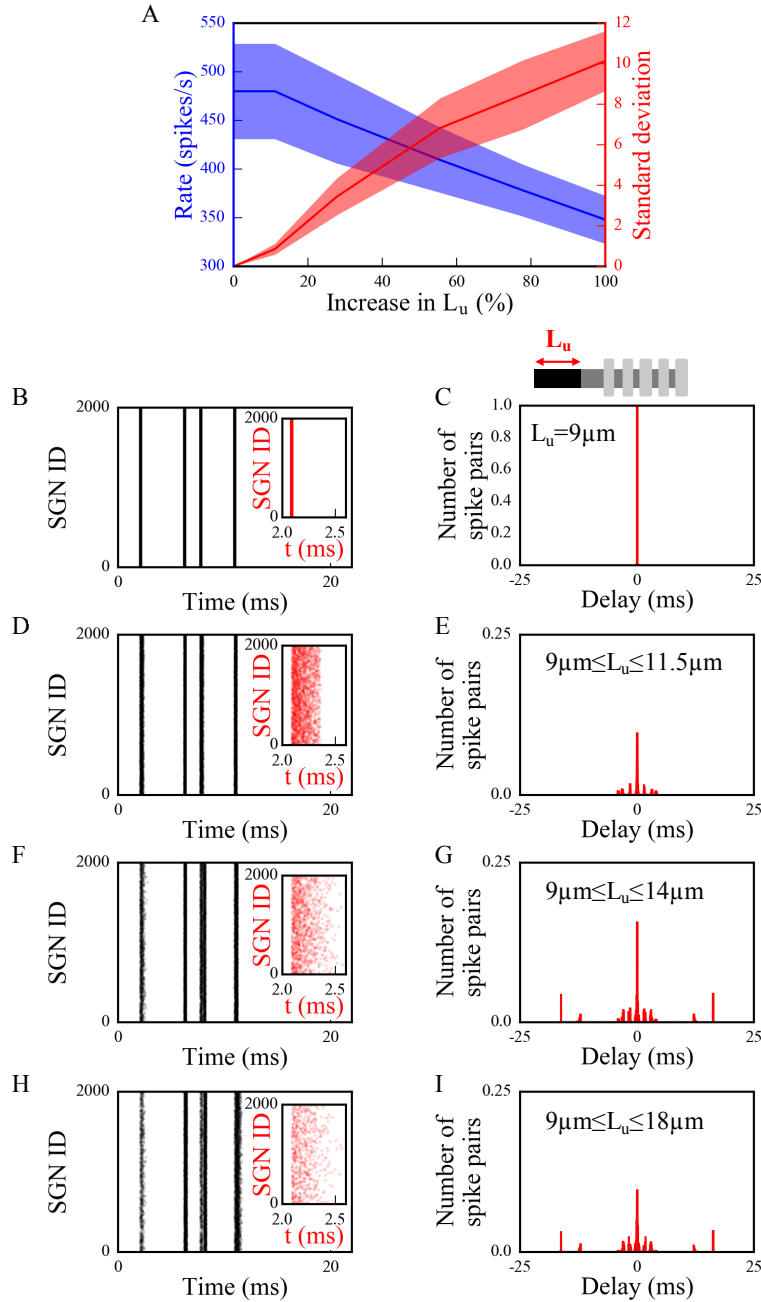
Figure III.4 The synchronous activity of SGN fiber populations is disrupted and their response to sound is decreased with increasing levels of L_u heterogeneity. SGN fiber populations with different heterogeneity levels of L_u were stimulated with a randomly determined release pattern. We assumed release events from all IHCs for the population occurred simultaneously. Raster plots [(B), (D), (F) and (H), insets: the first bursts of the raster plots] and corresponding histograms of time intervals between non-identical pairs of spike trains within a population [(C), (E), (G) and (I)] are shown for populations of SGN fibers with $L_u=9\mu m$ (0% increase in L_u) [(B) and (C)], $9\mu m \leq L_u \leq 11.5\mu m$ (~28% increase in L_u) [(D) and (E)], $9\mu m \leq L_u \leq 14\mu m$ (~56% increase in L_u) [(F) and (G)] and $9\mu m \leq L_u \leq 18\mu m$ (100% increase in L_u) [(H) and (I)]. The ordinates of the histograms are normalized over the number of spike pairs with 0ms delay for the population where all fibers have $L_u=9\mu m$ (C). Simulations were done 5 times. Firing rate and standard deviations of time intervals are averaged for all populations in (A), shaded area represents the standard error of the mean.

64

To investigate effects of this disruption of spike generation and timing in the full model, CAPs were computed from spike responses of populations of LT, MT and HT SGN fibers subject to simulated myelinopathy. Responses of fiber populations with homogeneous initial unmyelinated segments (L_u) or first heminode length (L_h) values were investigated to see the gradual effect of variable myelination patterns on cumulative activity of SGN fibers. Additionally, populations with heterogeneous, random L_u or L_h values were simulated to represent a population heterogeneity induced by myelinopathy. We note that when increasing first heminode length (L_h) the number of expressed channels (Na^+ and K^+) was kept constant, consequently decreasing their density. However, when increasing initial unmyelinated segment length (L_u), the density of expressed channels was kept constant, consequently increasing their number. Results were not qualitatively different when these assumptions were reversed (see Discussion in Section 3.4). Model results show that, in response to a simulated 70 dB SPL stimulus, CAPs computed from SGN fiber populations with homogeneous myelination patterns had decreased peak amplitude and increased latency to the peak when L_u was longer than the putative normal length of 9 μm (Fig III.5A) and L_h was longer than the putative normal length of 1 μm (Fig III.6A). The latency of the simulated CAP for a normal SGN population (L_u = 9 μm and L_h = 1 μm) was ~1.2ms, which is within the range of experimental CAP latencies [92]. The amplitude decrease was highly significant for L_u > 11 μm and L_h > 3 μm with ~60% of a drop from normal (Figs III.5B and III.6B). This was due to the fact that at those values failure of spike generation occurred because of the increased lengths, L_u and L_h. CAP peak latencies were significantly longer than normal for all homogeneous populations, with L_u > 12 μm and L_h > 3 μm having ~15% of an increase. The changes in CAP widths were minimal for all cases. For populations with heterogeneous

myelination patterns, however, CAP peaks were significantly (~45%) lower, and latencies and widths were significantly higher than normal populations (Figs III.5C and III.6C).
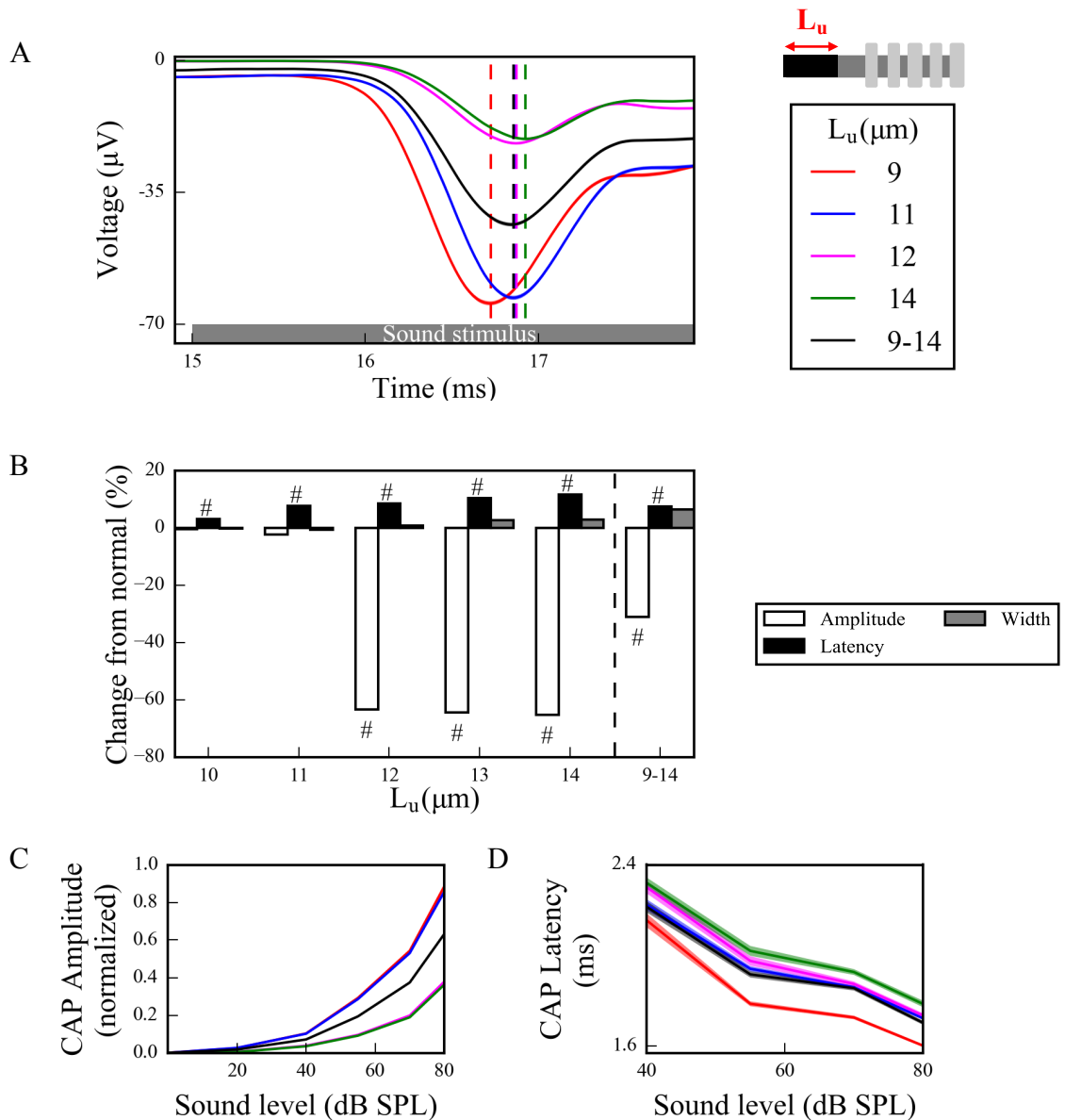
Figure III.5 Longer L_u significantly decreases and delays the peak of the sound-evoked CAPs of SGN fibers. (A) Sound-evoked CAPs of SGN fiber populations with varying L_u at 70dB SPL, averaged over 50 simulations. Shaded regions correspond to the standard error of the mean and dashed lines correspond to the peaks of each CAP, labeled with the same colors as the CAPs. The decrease and delay of peak CAPs are more obvious for populations with $L_u > 11$ μm. (B) Comparison of CAP measures of each population relative to normal L_u ($L_u = 9$ μm) at 70 dB SPL. Latencies are significantly higher for all populations and peaks are significantly lower for populations with $L_u > 11$ μm. The increases in widths are only minimal (*$p<0.05$, **$p<0.01$, #$p<0.001$). (C) Normalized CAP amplitudes for various sound levels exhibit an exponential increase and the decreases in CAP amplitudes for populations with $L_u > 11$ μm are more pronounced for higher sound levels. (D) The latencies of CAP peaks increase with higher L_u for all sound levels decreasing along the sound levels.
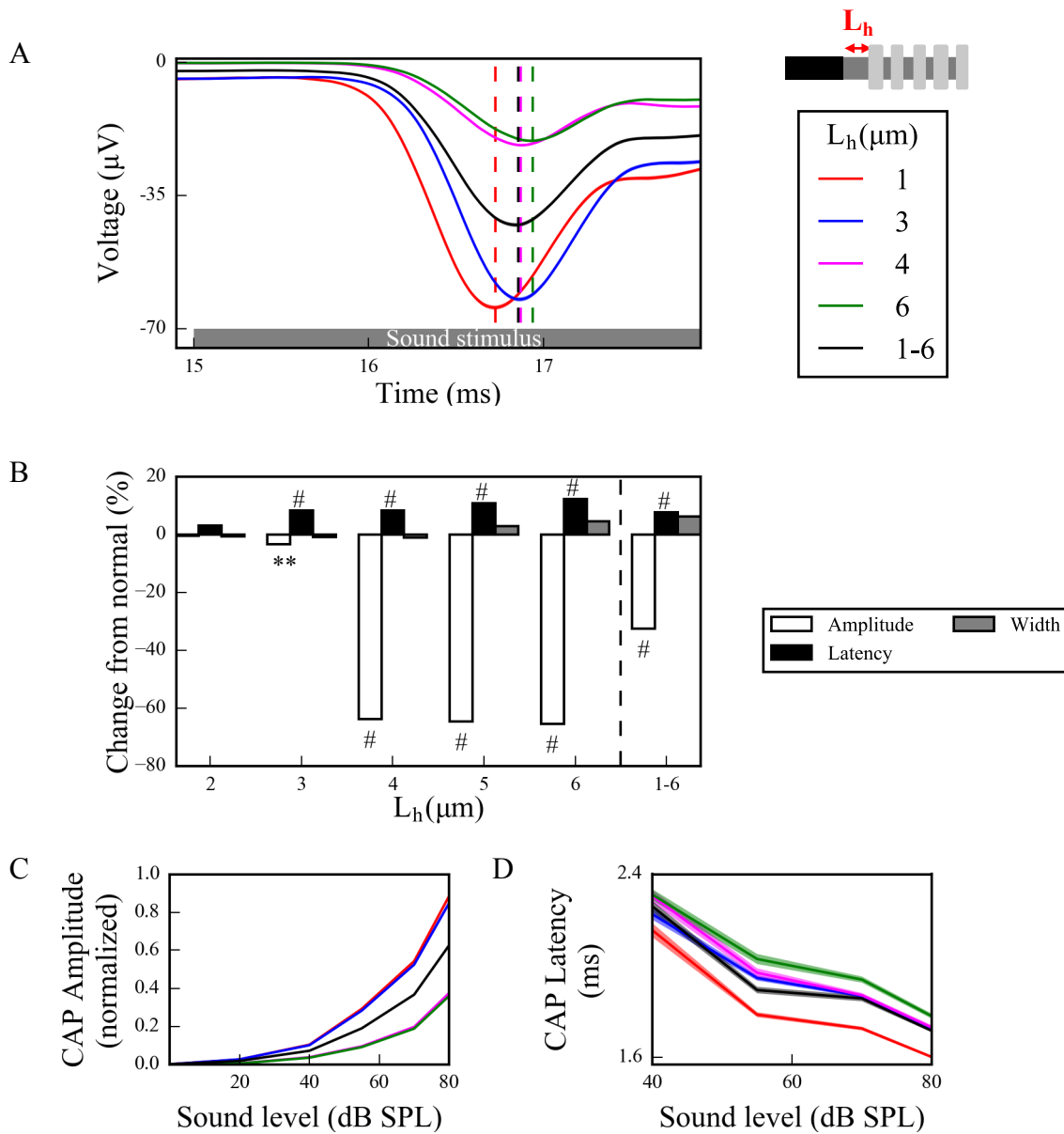
Figure III.6 Longer L_h significantly decreases and delays the peak of the sound-evoked CAPs of SGN fibers. (A) Sound-evoked CAPs of SGN fiber populations of varying L_h at 70dB SPL, averaged over 50 simulations. Shaded regions correspond to the standard error of the mean and dashed lines correspond to the peaks of each CAP, labeled with the same colors as the CAPs. The decreased peak amplitude and increased latency of CAP peak are more obvious for populations with $L_h > 3$ µm. (B) Comparison of CAP measures of each population relative to the normal L_h ($L_h = 1$ µm) at 70 dB SPL. CAP latencies are significantly higher for populations with $L_h > 2$ µm and peak amplitudes are significantly lower for populations with $L_h > 3$ µm. The increases in widths are only minimal (*$p<0.05$, **$p<0.01$, #$p<0.001$). (C) Normalized CAP amplitudes exhibits an exponential increase and the decreases in CAP amplitudes of populations with $L_h > 3$ µm are more pronounced for higher sound levels. (D) The latencies of CAP peaks increase with higher L_h for all sound levels decreasing along the sound levels.

67

In addition, to assess the dependencies of CAP properties on sound intensities, we measured responses to simulated sound stimuli between 0-80 dB. For $L_u \leq 11$ μm and $L_h \leq 3$ μm, CAP peak amplitudes increased with sound intensity (Figs III.5C and III.6C, respectively) and the profile of increase was more similar to experimental measurements of ABR (Fig III.1B, also see Supplementary Fig 3.4 in [61]) and CAP [92]. However, for $L_u > 11$ μm and $L_h > 3$ μm, CAP amplitudes remained small for all sound intensities due to reduced spike generation. For populations with heterogeneous myelination patterns, CAP amplitudes were between the L_u=11 μm and L_u=12 μm cases, and the L_h=3 μm and L_h=4 μm cases for all sound levels, reflecting reduced spike generation in some fibers of the population with higher L_u and L_h values. CAP latencies were longer for higher values of L_u and L_h (Figs III.5D and III.6D) and they decreased with increasing sound levels for all cases, consistent with experimental observations (Fig III.1C, also see Supplementary Fig 4 in [61]). In the heterogeneous populations, CAP latencies showed values similar to the L_u=11 μm and the L_h=3 μm cases.

3.3.2 Effects of synaptopathy on SGN population activation patterns

There is strong evidence indicating that noise-induced synaptopathy, primarily at HT fibers, could be one of the mechanisms of hidden hearing loss [43, 44, 93]. To simulate it, we considered responses of a population of control SGN fibers (L_u = 9 μm, L_h = 1 μm) with all HT IHC-SGN synapses removed. To investigate the specific effect of loss of synapses on HT fibers, we compared responses to the case where the same number of synapses (1/3th of whole population) were removed randomly from the whole population of three fiber types. The CAPs computed from populations with and without synaptopathy (Fig III.7A) in response to a 70 dB SPL suggest that HT-targeted synaptopathy produces only a small effect on CAP peak amplitude while random synaptopathy has a more significant effect on the amplitude (~30% vs ~10% decrease from normal

at 70dB SPL) (Fig III.7B). Moreover, there was no latency and width changes for both HT and random synaptopathies.
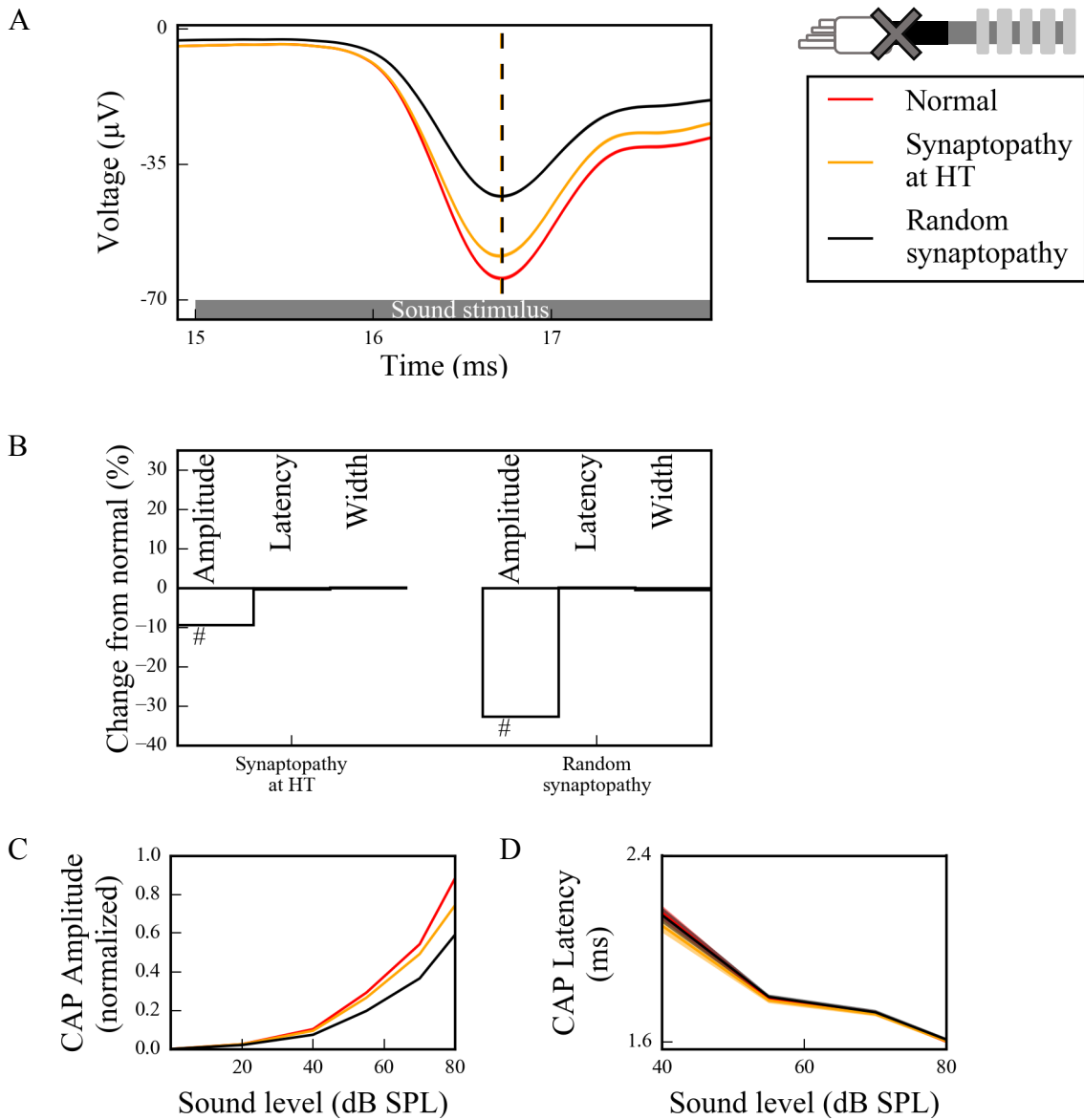
Figure III.7 Synaptopathy at IHC-SGN synapses decreases the peak of the CAP significantly, without changes to peak latency and width. (A) Sound-evoked CAPs of SGN fiber populations with different synaptopathy scenarios at 70dB SPL, averaged over 50 simulations. Shaded regions correspond to the standard error of the mean and dashed lines correspond to the peaks of each CAP, labeled with the same colors as the CAPs. Synaptopathy has smaller effects on CAP peak amplitude and latency when it affects only HT fiber synapses compared to affecting all fiber types randomly. (B) Comparison of CAP measures of synaptopathy cases relative to normal (no synaptopathy) at 70 dB SPL (*p<0.05, **p<0.01, #p<0.001). (C) Normalized CAP amplitudes exhibit an exponential increase and the decreases in CAP amplitudes of populations with both synaptopathy scenarios are more pronounced for higher sound levels. The latencies of the CAP peaks do not exhibit any significant difference between different populations for all sound levels.

We simulated sound intensities between 0-80 dB SPL to assess how CAP peak amplitude and latency depend on sound intensities in the synaptopathic cochlear model. For HT synaptopathy, a decrease of CAP peaks was observed for only higher sound intensities (>70dB SPL), while CAP peaks of random synaptopathy were lower than the normal case for sound intensities higher than 40dB SPL (Fig III.7C). CAP latencies did not show any significant differences for any sound level in any synaptopathy case (Fig III.7D).

3.3.3 Combined effects of myelinopathy and synaptopathy of hidden hearing loss

To investigate how different HHL mechanisms interact and affect cumulative SGN fiber activity, we combined them in our model (Fig III.8). When HT synaptopathy (Fig III.8A and B) was combined with myelinopathy affecting the length of the initial unmyelinated segment L_u, CAP peak amplitude showed significant additive decrease but latency and width showed no change beyond that produced by the myelin defects alone (compare Case 3 with Cases 1 and 2). When both myelinopathy mechanisms were combined by varying L_u and L_h across the population, both CAP peak amplitude and latency showed significant additive changes (compare Case 4 with Case 2). In response to varied sound intensities between 0-80 dB SPL, the additive effects of synaptopathy and myelinopathy on CAP peak amplitude and latency changes were prominent for higher SPL (Figs III.8C and D, respectively).
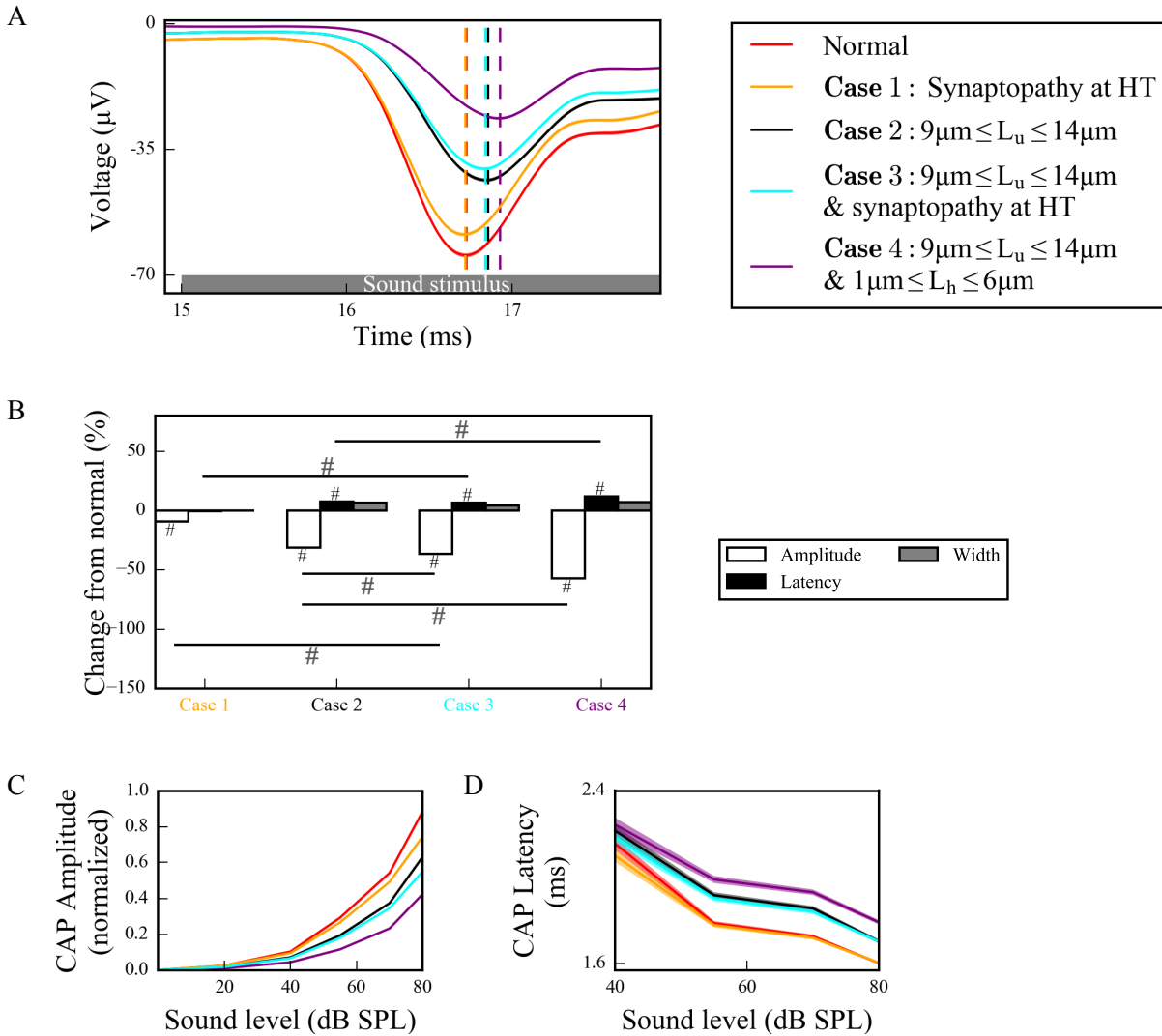
Figure III.8 Different scenarios of hidden hearing loss have additive effects on SGN activity. (A) Sound-evoked CAPs of SGN fiber populations with different myelinopathy and synaptopathy scenarios at 70dB SPL, averaged over 50 simulations (dashed lines correspond to the peaks of each CAP, labeled with the same colors as the CAPs). Combined synaptopathy and myelinopathy (Case 3) shows additive effects on the decrease in CAP peak amplitude, but not on the increase in CAP peak latency (compare to Cases 1 and 2). Combined different myelinopathies show additive effects on both CAP peak amplitude and latency (compare Cases 2 and 4). (B) Comparison of average CAP measures for different myelinopathy and synaptopathy cases relative to normal, and between cases at 70 dB SPL (*p<0.05, **p<0.01, #p<0.001). Normalized CAP amplitudes (C) and CAP latencies (D) for different myelinopathy and synaptopathy cases for various sound levels, averaged over 50 simulations. Shaded areas correspond to the standard error of the mean.

In summary, model results suggest that decreases in CAP peak amplitudes show additive effects for combined synaptopathy and myelinopathy. Also, there were significant increases in CAP peak latencies only for myelinopathy-based mechanisms, with latencies showing additive effects in combined myelinopathies, while synaptopathies do not affect this CAP features.

71

3.4 Discussion

We built a reduced biophysical model simulating sound-evoked activity of type I SGN populations to analyze two hypotheses of the cause of HHL, synaptopathy and myelinopathy. Model SGN spike times were convolved with the unitary response of the CAP, a near-field response of SGNs, to convert spike times into cumulative activity for comparison with experimental results. The cumulative CAP for the normal case (L_u=9 µm and L_h=1 µm) in our model has similar characteristics as experimental CAP [92]: The peak latency at 80dB SPL is ~1.2ms and the peak amplitude increases exponentially with increasing sound levels, with a value of ~70µV at 70dB SPL. Moreover, the model shows that synaptopathy reduces the amplitude of the cumulative CAP response without affecting its latency due to a reduction in the number of nerve fibers responding without disruption of spike timing. In contrast, myelinopathy, when modeled as disorganization of either the initial unmyelinated nerve segment length or the heminodal spacing, causes disruption of spike timing in addition to loss of firing response, affecting both the peak amplitude and latency of the cumulative CAP.

Previously, it has been shown that noise exposure and aging cause HHL due to synapse loss at SGN-IHC synapses, which results in a decrease of ABR P1 without increases in latency or thresholds (Fig III.1A) [45, 60, 61, 94]. Moreover, it has been hypothesized that synapse loss occurs preferentially at HT SGN-IHC synapses [43]. Consistent with experimental results, our simulations for both HT synaptopathy and random synaptopathy show that CAP latencies are unchanged for either scenario, but the amplitude of the CAP peak is significantly decreased. However, the decrease in CAP amplitude was larger for random synaptopathy, in contrast to HT synaptopathy case, where differences in SGN fiber activity appeared only with higher SPL stimuli. These results suggest that synaptopathy at HT synapses is a more likely scenario for HHL than

random loss of synapses, since experimental results show that thresholds remain unchanged (Fig III.7) [43].

A computational study from Bourien et al. (2014) has previously investigated the effects of different auditory fiber degeneration scenarios on cumulative CAP characteristics [92]. They provided evidence that removing $1/3^{rd}$ of the auditory fibers randomly from an auditory fiber population linearly decreased the cumulative CAP amplitude with minimal threshold elevation and no change in CAP peak latency, which is consistent with our results for random synaptopathy (Fig III.7). They also removed preferentially HT fibers from the population and showed that there is no threshold elevation and no change in CAP peak latency and amplitude, when all HT fibers are removed. This is slightly different than our results for HT synaptopathy, since we saw a decrease in CAP peak amplitude, when we removed all HT synapses (Fig III.7). This might be due to the difference in HT fiber proportions in both studies; in our case $1/3^{rd}$ of the synapses are HT, whereas in their study it is only 10%.

As shown by Wan and Corfas (2017), myelinopathy affects the distance from the IHC-SGN synapse to the heminode and introduces heterogeneity in heminode locations across a SGN fiber population, which is likely to result in their desynchronized activity [61]. Here, we provided evidence that increasing heterogeneity of heminode locations decreases the synchronization of spike timing of SGN fiber populations. Moreover, spike rates of more heterogeneous SGN fiber populations dropped, suggesting a loss of spike generation in SGN fibers with heminodes further from IHCs (Fig III.4). Our simulations of cumulative CAP signals show that myelinopathy increases the latency and the width of the peak of CAP, similar to experimental observations of ABR P1 (Fig III.1C), providing support for the disruption of spike timing in SGN activity (Figs

III.5 and III.6). In addition, the amplitude of the simulated CAP decreased with myelinopathy, reflecting the reduction of SGN spike activity.

Combining synaptopathy and myelinopathy HHL mechanisms led to additive effects in our model. Decreases in CAP peak amplitude were additive for combined synaptopathy and myelinopathy, but synaptopathy did not contribute to changes in CAP latency even in the combined scenario. Combining myelinopathy mechanisms led to additive increases in both peak CAP amplitude and latency (Fig III.8). These results match with the experimental results qualitatively (Fig III.1A), further supporting the accuracy of our model.

In the myelinopathy simulations, we varied the length of the initial unmyelinated segment L_u keeping a constant channel density (Fig III.5) and varied the length of the heminode L_h keeping constant channel numbers (Fig III.6). Results show similar effects on SGN fiber activity, i.e. the populations with the same combined lengths L_u+L_h exhibit the same behavior. As evidence on how channels might be affected by the disruption of myelination patterns is lacking, we also simulated cases where L_u increases with constant channel number (Supplementary Figure 3.1) and L_h increases with constant channel density (Supplementary Figure 3.2). Results show that spreading the same number of channels over an increased L_u (Supplementary Figure 3.1), rather than increasing the number by keeping the channel density constant (Fig III.5), decreases the L_u value at which the abrupt decrease in CAP peak occurs due to loss of spike generation. With constant channel number, CAP peaks for homogeneous populations with L_u>11 μm decreased ~70% from normal (L_u=9 μm) (Supplementary Figure III.1B). In contrast, varying L_h while keeping the heminode channel density constant, i.e., increasing the number of channels for larger L_h, increased the L_h value associated with the loss of spike generation up to 6 μm, compared to 3 μm when channel number was kept constant (Fig III.6). To conclude, any of these scenarios results in

74

qualitatively similar SGN fiber activity patterns, only affecting the L_u and L_h lengths at which loss of spike generation leads to an abrupt drop in the CAP peak.

To better understand the effects of myelinopathy on SGN spike generation, we additionally analyzed the outcome of one vesicle release event to a single SGN fiber. As described in the Methods section, SGN response to vesicle release was simulated by applying a brief external current pulse to the peripheral end of the SGN fibers. We calculated the time difference between a spike of one SGN fiber and the preceding release event, which we define as delay, for various amplitudes (A in Equation 3.12) of the external current pulse I_{app}, by keeping τ_1 and τ_2 constant (Supplementary Figure 3.3). Here, we provided evidence that increasing L_u delays the spike more, up to a critical value of L_u for all I_{app} characteristics. For L_u values higher than the critical value, single release event does not result in a spike at an SGN fiber. We showed that this critical value is higher for stronger external current pulses (I_{app}) and the increase in the delay with increasing L_u is faster for weaker I_{app}. However, different I_{app} characteristics exhibit qualitatively similar trends, meaning that synaptic efficacy would not affect our results qualitatively.   Then, we investigated the population outcome of vesicle release events to the SGN fibers. We thus calculated the probability that release events result in corresponding spikes for various amplitudes I_{app} of the external current pulse for increasing values of L_u (Supplementary Figure 3.4A). For simulated 70dB SPL stimuli, higher I_{app} amplitudes increased spike probability for larger L_u values, leading to increases in the L_u values at which spike generation was affected. If L_u exceeded a critical value, the probability of spike generation decreased significantly, due to the fact that one release event is not enough to generate a spike in an SGN fiber with an L_u higher than this critical value, as shown in Supplementary Figure 3.3. These results show that this L_u critical value required for spike generation depends on IHC-SGN synaptic efficacy.

To analyze the effect of sound level on SGN fiber spike probability, we ran simulations for all sound levels keeping the amplitude (A) of I_{app} fixed at the default value ($A = 0.1$nS, solid black rectangle in Supplementary Figure 3.4A). As described in the Methods section, increasing sound level was simulated by increasing the probability of a vesicle release event, thus leading to higher rate of release from IHCs, i.e. higher frequencies of external current pulse applications to SGN fibers. For this I_{app} value, spike generation was affected for $L_u > 11$ μm as evident in the results shown in Fig III.5. For SGN fibers with $L_u \leq 11.7$ μm, spike probabilities were higher than 40% for all sound levels (Supplementary Figure 3.4B). However, spike probabilities decreased gradually with higher sound levels due to the inability of the fibers to respond to high frequency stimulation. This means, despite more frequent release events from IHC-SGN synapses with higher sound levels, SGN fibers cannot fire with a higher frequency due to the saturation of their spike rate, resulting in decreased spike probabilities. For SGN fibers with $L_u > 11.7$ μm, spike probability was very low reflecting loss of spike generation but it increased slightly with increasing sound level, as high frequency stimulation facilitated spike generation due to temporal summation. Results for heterogeneous L_u values between 9 and 14 μm showed intermediate spike probabilities (~40%) as compared to homogeneous L_u values of 9 μm, for all sound levels.

Lastly, to analyze effects of myelinopathy on SGN spike latency, we averaged the time differences between each spike and the preceding release event causing the spike for populations of SGN fibers with varied homogeneous L_u values and varied sound levels (Supplementary Figure 3.4C). The populations with $L_u > 11$ μm were not included since spikes were not reliably generated and for the heterogeneous population, the fibers with $L_u > 11$ μm were ignored. The homogeneous populations showed increased latencies with increasing L_u and the heterogeneous population's latencies were between those for $L_u = 10$ μm and $L_u = 11$ μm for low sound intensities. Latencies

were generally decreased with increasing sound levels. However, standard deviations of spike latencies increased with sound level, presumably reflecting higher variability in spike response to higher frequency stimulation (Supplementary Figure 3.4D). Additionally, the population with heterogeneous L_u values showed higher standard deviations for lower sound levels than the homogeneous populations with $L_u \leq 11$ µm. This increase in spike timing variability is responsible for increases in the width of the cumulative CAP for the heterogeneous population shown in Fig III.5.

In conclusion, our model results show that HHL deficits due to myelinopathy could be caused by not only loss of SGN spike activity, as in synaptopathy, but also disruption of spike timing and synchronization across a population of SGN fibers. Furthermore, these results can be revealed with simpler models of inner hair cell release, without taking the nonlinear dynamics of cochlear excitation into account, illustrating the significance of the SGN fiber organization of our model (data not shown). Illumination of the underlying differences in these mechanisms for HHL based on the model may be useful for the development and testing of treatments for HHL. Moreover, the model framework may be extended to investigate mechanisms behind other peripheral auditory system disorders.

Chapter IV

Binaural Processing Deficits Due to Myelin Defects

4.1 Introduction

The ability to determine the location of the source of a sound is critical for all animals. They can easily find prey, escape from predators and survive other dangers in nature thanks to their sound localization skills. Humans, as well, benefit from this ability to assess their safety and to distinguish speech when competing sounds are present. Unlike visual and somatosensory systems, the auditory system does not use location cues to detect where the stimulus comes from. Instead, temporal, spectral and intensity cues are needed to determine the location of the source in three-dimensional space [55]. Locating the sound in the horizontal plane requires precise temporal and intensity information coming from both ears. Integration of the binaural information in humans takes place in the superior olivary complex (SOC) located in the midbrain, which has a nucleus called the medial superior olive (MSO), where temporal cues are analyzed. MSO cells receive binaural excitatory and inhibitory inputs from spherical (SBC) and globular bushy cells (GBC), respectively [57]. SBCs and GBCs are located in the cochlear nucleus, the first relay point for signals from the periphery to the central auditory system. Multiple spiral ganglion neurons (SGNs) project to SBCs and GBCs, which respond more phase-locked to sound than the SGN fibers, therefore transmitting more precise timing information to MSO cells [54].

MSO cells are sensitive to interaural time differences (ITDs), the difference in the arrival time of the sound to both ears, thanks to their coincidence detection properties [56]. This means, MSO cells do not fire unless they are excited by contra- and ipsilateral SBCs within a short time window. Consequently, humans can resolve ITDs as short as 10μs and can locate the sound as precisely as a few degrees [47]. For the binaural excitatory inputs to coincide at the MSO on one side of the brain, the sound should arrive to the contralateral ear first, to compensate for the internal delay caused by the path the signal needs to travel in the brain from one hemisphere to the other. As a result, the ITDs with the highest MSO activity, also called the best ITDs, correspond to slightly contralateral leading sound sources. This gives rise to different MSO activity patterns in each hemisphere, and the horizontal location of the sound is encoded in the brain by the difference in firing rates between the MSOs in both hemispheres [58].

The precise timing of binaural signals is essential to detect the horizontal direction of the sound source. Therefore, the disruption of the synaptic signaling along the peripheral auditory circuits would significantly impair sound localization skills in humans. Many behavioral and electrophysiological studies suggest that humans with normal audiometric thresholds have problems with encoding and processing binaural cues, giving rise to speech intelligibility and ITD sensitivity deficits, as a result of noise exposure [95-97], aging [98] or demyelinating diseases [65, 99, 100], a condition known as hidden hearing loss (HHL). In this study, we hypothesize that these perceptual deficits stem from the lack of coincidence of inputs from SBCs to MSO cells, leading to decreased activity levels of MSO cells and ITD discrimination deficits. To test this hypothesis, we employ the computational model from Chapter III to simulate the activity of SGN fibers with myelin defects at SGN heminodes, since animal studies suggested that myelinopathy in the SGN heminodes results in HHL. Then, we simulate the activity of SBCs and GBCs, which then project

to MSO cells. Model results show decreased firing rates of MSO cells for varying ITDs with increasing degrees of myelinopathy indicating decreased MSO activity and ITD sensitivity. Thus, we provided evidence that myelin defects might lead to lower MSO activity levels, which potentially causes sound localization problems and speech intelligibility deficits in HHL patients.

4.2 Methods

4.2.1 SGN fibers

A compartmental model for peripheral axons of SGN fibers are modeled as described in Section 3.2.1. Each SGN fiber has an initial unmyelinated segment L_u and a heminode length L_h. The putative control is identified as an SGN population with all fibers having L_u of 9µm and L_h of 1µm. We modeled myelinopathy by forming populations of SGNs with heterogeneous L_u values where we increased L_u variation up to a range of 9-18 µm. We denote a homogeneous population with our putative control (L_u=9 µm) as 0% variation of L_u, and the heterogeneous population with L_u values distributed uniformly between 9-18 µm as 100% variation of L_u.

To represent the sound stimulus, we used the model described in Section 3.2.2 in our simulations. Spike trains of SGNs were generated by the model explained in Section 3.2.2.

4.2.2 Network structure

Arrival of sound to the ear triggers neurotransmitter release from inner hair cells, which then activates SGNs. SGNs transmit this input to the ipsilateral and contralateral cochlear nuclei. SBCs and GBCs in the cochlear nucleus receive inputs from multiple SGNs (2-3 to SBCs and 5-40 to GBCs [101]), leading to higher phase-locking with the sound signal. MSO cells receive binaural excitatory inputs directly from SBCs and binaural inhibitory inputs from GBCs via a relay point, trapezoid body (TB).

In our cochlear nucleus circuit model, we implement previously developed neuron models for SBC, GBC and MSO cell populations in both hemispheres, with each population containing 300 neurons. For simplicity, we assumed GBCs send signals directly to MSO cells. SGN populations consist of 100 low-threshold (LT), 100 medium-threshold (MT) and 100 high-threshold (HT) neurons, each having characteristic frequencies at 200Hz (see Section 3.2.3 for the definition of SGN types and how they are implemented). Each SBC receives 4 and each GBC receives 40 excitatory inputs from ipsilateral SGNs. MSO is the first region of binaural integration in the auditory circuit, and each cell in the MSO gets 6 excitatory inputs from SBCs of each hemisphere and 3 inhibitory inputs from GBCs of each hemisphere.

4.2.3 Node dynamics of SBCs, GBCs and MSOs

Implementing a previously developed model of the cochlear nucleus circuit, SBC, GBC and MSO cells are modeled as single compartment Hodgkin-Huxley type models, with parameters and ion channels adjusted to experimental observations [102].

The membrane potentials of SBCs and GBCs are modeled as

$$C_m \frac{dV_m}{dt} = -(g_l(V_m - E_{rest}) + g_{Na}m^3h(V_m - E_{Na}) + g_{KHT}n^2p(V_m - E_K) + g_{KLT}w^4z(V_m - E_K) + g_h r(V_m - E_h) + I_{syn}), \tag{4.1}$$

where C_m is the membrane capacitance, g_l is the leak conductance, g_{Na} is the Na$^+$ conductance, g_{KHT} and g_{KLT} are high and low threshold K$^+$ conductances, respectively, and g_h is the hyperpolarization-activated cation conductance. E_{rest} stands for the resting membrane potential and E_x represents the Nernst potentials of each ion x (for x=Na$^+$, K$^+$ and H$^+$) (Table 4.1). The variables m, h, n, p, w, z and r are the voltage dependent conductance gating variables expressed as

$$\frac{di}{dt} = \alpha_i(V_m)(1 - i) - \beta_i(V_m)i \quad for \ i = m, h \tag{4.2}$$

81

and

$$\frac{dj}{dt} = \frac{j_\infty - j}{j_\tau} \; for \; j = n, p, w, z, r \tag{4.3}$$

where,

$$\alpha_m(V_m) = \frac{1.872(V_m + 49)}{1 - e^{\frac{-(V_m + 49)}{3}}} \tag{4.4}$$

$$\beta_m(V_m) = \frac{-2.08(V_m + 58)}{1 - e^{\frac{(V_m + 58)}{20}}} \tag{4.5}$$

$$\alpha_h(V_m) = \frac{12.48}{1 + e^{\frac{(V_m + 68)}{3}}} + \frac{25.344}{1 + e^{V_m + 61.3}} \tag{4.6}$$

$$\beta_h(V_m) = \frac{18.72}{1 + e^{\frac{-(V_m + 21)}{10}}} \tag{4.7}$$

$$w_\infty(V_m) = (1 + e^{\frac{-(V_m + 48)}{6}})^{-0.25} \tag{4.8}$$

$$\tau_w(V_m) = 1.5 + \frac{100}{6e^{\frac{(V_m + 60)}{6}} + 16e^{\frac{-(V_m + 60)}{45}}} \tag{4.9}$$

$$z_\infty(V_m) = 0.5 + \frac{1}{2(1 + e^{\frac{(V_m + 71)}{10}})} \tag{4.10}$$

$$\tau_w(V_m) = 50 + \frac{1000}{e^{\frac{(V_m + 60)}{20}} + e^{\frac{-(V_m + 60)}{8}}} \tag{4.11}$$

$$r_\infty(V_m) = (1 + e^{\frac{(V_m + 76)}{7}})^{-1} \tag{4.12}$$

$$\tau_r(V_m) = 25 + \frac{100000}{237e^{\frac{(V_m + 60)}{12}} + 17e^{\frac{-(V_m + 60)}{14}}} \tag{4.13}$$

$$n_\infty(V_m) = (1 + e^{\frac{-(V_m + 15)}{5}})^{-0.5} \tag{4.14}$$

$$\tau_n(V_m) = 0.7 + \frac{100}{11e^{\frac{(V_m + 60)}{24}} + 21e^{\frac{-(V_m + 60)}{23}}} \tag{4.15}$$

$$p_\infty(V_m) = (1 + e^{\frac{-(V_m + 23)}{6}})^{-1} \tag{4.16}$$

$$\tau_p(V_m) = 5 + \frac{100}{4e^{\frac{(V_m + 60)}{32}} + 5e^{\frac{-(V_m + 60)}{22}}}. \tag{4.17}$$

I_{syn} is the excitatory synaptic current generated by SGN activity expressed as

$$I_{syn}(t, V_m) = \sum_{i=1}^{N} A e^{\frac{-(t-t_{s_i})}{0.2}} (V_m - E_{ex}) \qquad (4.18)$$

where N is the number of presynaptic spikes, t_{s_i} is the time of the presynaptic SGN spike i and

E_{ex}=0 mV is the reversal potential for excitatory current. A is the synaptic strength and equals

13nS for SBCs and 4.76nS for GBCs. These values of A are adjusted to obtain experimentally

observed responses for the activity of SBC and GBC populations. The refractory period for both

populations is 0.5ms and no signals can be received during this period.

Table IV-1 Parameters for SBC, GBC and MSO cells

	SBC-GBC	MSO
C_m (pF)	12	70
E_{rest} (mV)	-65	-55.8
g_l (nS)	37	13
E_{Na} (mV)	50	56.2
g_{Na} (nS)	4592.8	3900
E_K (mV)	-77	-90
g_{KHT} (nS)	35.1	650
g_{KLT} (nS)	367.4	N/A
E_h (mV)	-43	-35
g_h (nS)	36.7	520

The current balance equation for MSO cells is expressed as

$$C_m \frac{dV_m}{dt} = -(g_l(V_m - E_{rest}) + g_{Na}m^3h(V_m - E_{Na}) + g_{KLT}w^4z(V_m - E_K) + g_h r(V_m - E_h) +$$

$$I_{syn,e} + I_{syn,i}), \qquad (4.19)$$

where C_m is the membrane capacitance, g_l is the leak conductance, g_{Na} is the Na$^+$ conductance, g_{KLT} is the low threshold K$^+$ conductance and g_h is the hyperpolarization-activated cation conductance. E_{rest} stands for the resting membrane potential and E_x represents the Nernst potentials of each ion x (for x=Na$^+$, K$^+$ and H$^+$) (Table 4.1). The variables m, h, w, z and r are the voltage dependent conductance gating variables that are governed by Equation (4.3) with steady state activation and time constant functions given by

$$m_\infty(V_m) = (1 + e^{\frac{-(V_m+38)}{7}})^{-1} \tag{4.20}$$

$$\tau_m(V_m) = \frac{0.48}{5e^{\frac{(V_m+60)}{18}} + 36e^{\frac{-(V_m+60)}{25}}} \tag{4.21}$$

$$h_\infty(V_m) = (1 + e^{\frac{(V_m+65)}{6}})^{-1} \tag{4.22}$$

$$\tau_h(V_m) = \frac{19.23}{7e^{\frac{(V_m+60)}{11}} + 10e^{\frac{-(V_m+60)}{25}} + 0.12} \tag{4.23}$$

$$w_\infty(V_m) = (1 + e^{\frac{-(V_m+57.3)}{11.7}})^{-1} \tag{4.24}$$

$$\tau_w(V_m) = \frac{46}{6e^{\frac{(V_m+75)}{12.15}} + 24e^{\frac{-(V_m+75)}{25}} + 0.55} \tag{4.25}$$

$$z_\infty(V_m) = 0.4 + 0.6(1 + e^{\frac{(V_m+57)}{5.44}})^{-1} \tag{4.26}$$

$$\tau_z(V_m) = 12 + \frac{240}{e^{\frac{(V_m+60)}{20}} + e^{\frac{-(V_m+60)}{8}}} \tag{4.27}$$

$$r_\infty(V_m) = (1 + e^{\frac{(V_m+80.4)}{10}})^{-1} \tag{4.28}$$

$$\tau_r(V_m) = 79 + e^{\frac{-(V_m+61.5)^2}{800}} \tag{4.29}$$

$I_{syn,e}$ and $I_{syn,i}$ are excitatory and inhibitory synaptic currents received from the SBC and GBC cells, respectively. $I_{syn,e}$ is described as

$$I_{syn,e}(t, V_m) = \sum_{i=1}^{N}(54.37nS)\frac{t - t_{s_i} - t_{delay}}{0.17}e^{-\left(\frac{t-t_s-t_{delay}}{0.17}\right)}(V_m - E_{ex}), \tag{4.30}$$

where N is the number of presynaptic SBC spikes, t_{s_i} is is the time of the presynaptic SBC spike i and E_{ex}=0 mV is the reversal potential for excitatory current. t_{delay} is the time required for the signal from SBCs to reach MSO cells, which is 1.5ms for ipsilateral input and 1.6ms for contralateral input.

$I_{syn,i}$ is expressed as

$$I_{syn,i}(t, V_m) = -\sum_{i=1}^{N}\left\{(5.8nS)(e^{-\left(\frac{t-t_{s_i}-t_{delay}}{0.14}\right)} - e^{-\left(\frac{t-t_{s_i}-t_{delay}}{1.6}\right)})\right\}(V_m - E_{in}), \quad (4.31)$$

where N is the number of presynaptic GBC spikes, t_{s_i} is the time of the presynaptic GBC spike i and E_{ex}=-70 mV is the reversal potential for excitatory current. t_{delay} is the time required for the signal from GBCs to reach MSO cells, which is 1.5ms for ipsilateral input and 1.0ms for contralateral input.

4.2.4 Vector strength and relative vector strength measurements

A measure of vector strength (VS) is used to determine the degree of phase-locking of a neuron population to a sound wave. It is calculated as

$$VS = \frac{\sqrt{[\sum_{i=1}^{n}\cos\theta_i]^2 + [\sum_{i=1}^{n}\sin\theta_i]^2}}{n}, \quad (4.32)$$

where θ_i is the phase of each spike i within the periodic sound wave, and n is the total number of spikes within a neuron population [103]. This measure varies between 0 and 1, where 1 means perfect synchrony and 0 means no phase-locking to sound.

Relative VS is used to assess the degree of phase-locking relative to the putative control. It can be defined as

$$Relative\ VS = \frac{\sqrt{[\sum_{i=1}^{n}\cos\theta_i]^2 + [\sum_{i=1}^{n}\sin\theta_i]^2}}{N}, \quad (4.33)$$

where θ_i is the phase of each spike i within the periodic sound wave, and N is the total number of spikes in the putative control.

4.2.5 Simulations

We simulated the sound-evoked activity of all cell types in response to a sound stimulus pulse of 200Hz and 50dB for 100ms. Our results below (Section 4.3) show the responses to one sound stimulus.

4.3 Results

Our model generates spike times of SGN, SBC, GBC and MSO populations in response to a sound stimulus. We analyzed the spike rates and vector strengths of phase-locking to sound for the different cell types while simulating varying degrees of myelinopathy on SGN axons. As in Chapter III, we investigate changes in firing patterns as a function of variation of L_u, the length of the initial unmyelinated segment of SGN axons. In our putative control case with 0% variation of L_u, in response to a sound pulse, the VS of SGN axons is approximately 0.84 while the VS of SBCs is approximately 0.93, which is higher than the SGNs. The GBC and MSO cell responses are highly phase-locked to the sound wave, with VS approaching to 1.0. (Fig. IV.1A). These results agree with experimental observations [54, 104] that locking to sound increases at SBCs and even more so at GBCs and MSO cells, as compared to SGNs. Even though increasing the degree of myelinopathy did not affect the VS significantly indicating that firing neurons remain locked to the sound independent of variation of L_u, the relative VS for all cell populations decreased for higher variations of L_u (Fig. IV.1B). Moreover, this drop was more significant for SBCs and MSOs, which act as monaural and binaural coincidence detectors, respectively. This shows that the

disruption of SGN activity due to myelinopathy has a high downstream impact on the level of phase-locking to sound in the SBC and MSO populations.

We measured this effect directly by comparing the relative change in firing frequency across the cell populations. Myelin defects in SGN fibers cause a drop in cumulative SGN activity [61], as shown in Chapter III. Here, as well, simulations with different degrees of myelinopathy suggest that the activity of an SGN population is significantly decreased with increasing degrees of myelinopathy (Figure IV.2A). This leads to smaller numbers of input spikes to the cochlear nucleus, significantly decreasing the firing rates of SBCs (Figure IV.2B), GBCs (Figure IV.2C) and finally MSO cells as well (Figure IV.2D). Moreover, the change of firing rates relative to the putative control (0% variation in L_u) suggests that the activity drop with L_u variation is more significant in SBCs than SGNs, with MSO cells showing the largest relative decreases (Figure IV.2E).

A

B
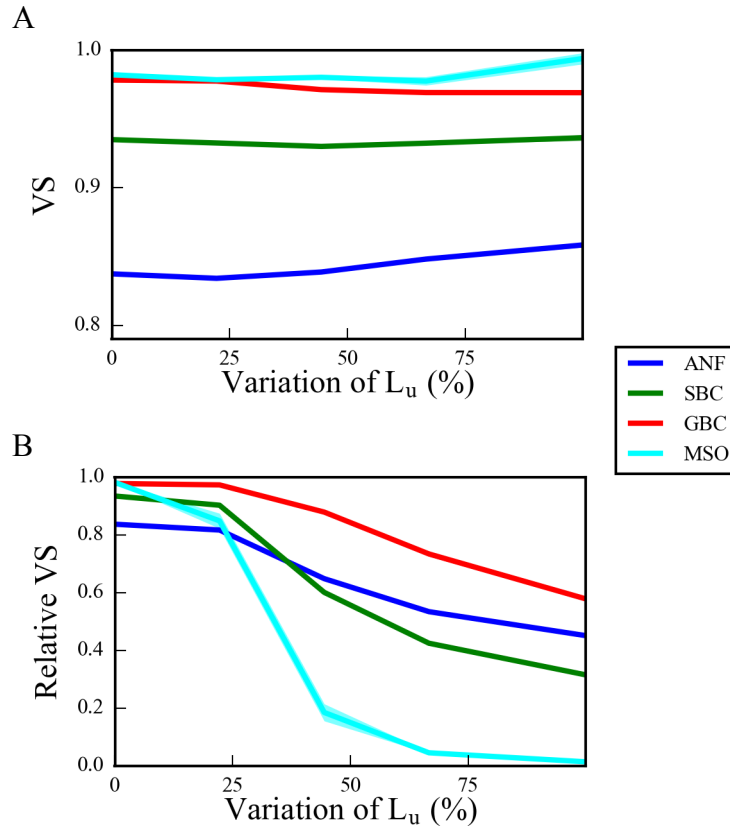
Figure IV.1 (A) Vector strength of phase-locking to the sound wave and (B) relative vector strength measurements for different cell types and degrees of myelinopathy in response to 200Hz, 50dB sound stimulus. Here, 0% variation of L_u represents a circuit with a homogeneous population of SGNs with 9 μm long L_u and 100% variation of L_u represents a circuit with a heterogeneous SGN population with 9 μm $\leq L_u \leq$ 18 μm.

Since the horizontal location of sound sources are encoded by the difference in firing rates between MSO cells on the left and right sides of the brain [104], we simulated MSO activity in both hemispheres for different ITD values, representing the horizontal angle of the sound. Here, ITD>0 means that sound arrives first to the left ear and ITD<0 means that sound arrives first to the right ear. For our putative control case, model results showed that MSO activity on one side of the brain reaches a maximum for sounds coming from slightly contralateral positions (Figure IV.3A, blue curve), as the delayed arrival of sound to the ipsilateral ear compensates for the internal delay of the contralateral signal due to the path it travels between the hemispheres of the brain. This asymmetric bell-shaped curve of MSO activity relative to ITDs is critical, as the difference

between left and right MSO spike rates encodes the horizontal angle of the sound (Figure IV.3B,

blue curve). Simulated increasing degrees of myelinopathy decreased the peak of this bell-shaped

curve (Figure IV.3A), leading to lower rate differences between left and right MSO cells (Figure

IV.3B).
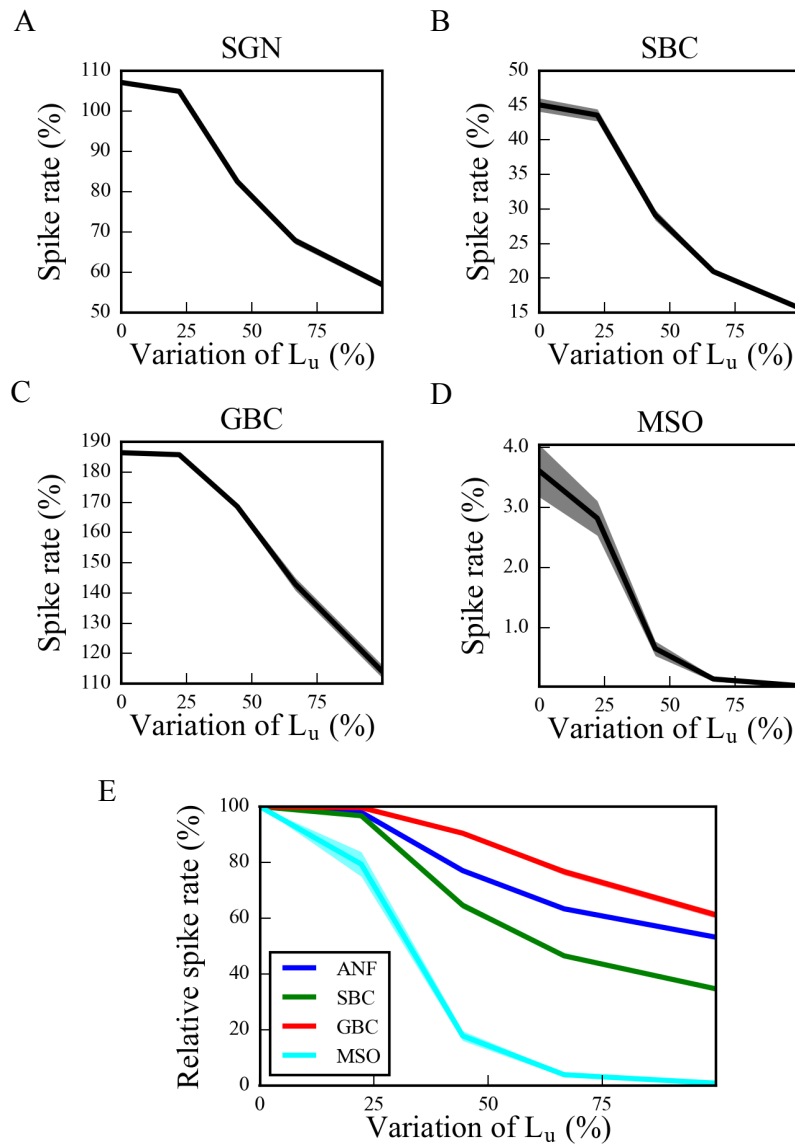
Figure IV.2 The spike rates of (A) SGNs, (B) SBCs, (C) GBCs and (D)MSO cells for increasing L_u variations show that activities of all cell types are decreased for higher variations. (E) Spike rates relative to the putative control (0% variation) show that MSO cells are affected the most by myelinopathy. Here, 0% variation of L_u means that all SGNs within the MSO circuit have $L_u = 9$ μm and 100% variation of L_u stands for a circuit with a heterogeneous SGN population with 9 μm $\leq L_u \leq 18$ μm. The spike rate of MSO populations are calculated at their best ITDs (ITD=0.2ms for the right MSO)

A

B
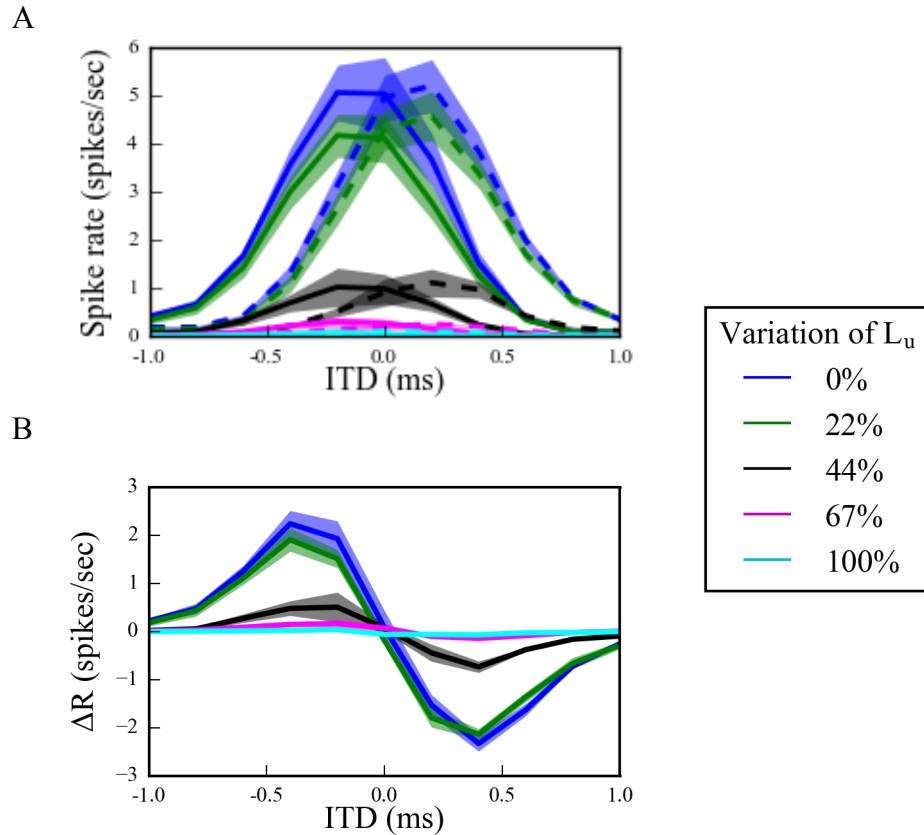
Figure IV.3 The spike rates of MSO cells at their best ITDs drop significantly for increasing L_u variation.
(A) Spike rates of left (solid lines) and right (dashed lines) MSO cells as a function of ITD for circuits with SGN populations of varying ranges of L_u values. (B) The difference of MSO firing rates (MSO$_{left}$-MSO$_{right}$) for varying degrees of myelinopathy in SGN fibers.

4.4 Discussion

In this study, we built a computational model of mammalian cochlear nucleus circuits to understand the impact of SGN myelin defects on binaural information processing. Specifically, we explored how the activity of SGNs, cochlear nucleus cells (SBCs and GBCs) and MSO cells are affected by varying degrees of demyelination. We modeled the degree of demyelination by increasing the range of L_u, the length of the initial unmyelinated segment in SGN axons, within a population of SGN fibers and showed that the activity of an SGN population and the level of phase-locking to the sound stimulus drops for cases with larger L_u ranges. As a result, the cochlear nucleus is driven less by SGN fiber inputs, subsequently decreasing the firing rates of SBC and

GBC populations. Moreover, the drop in the activity levels relative to the putative control is bigger in SBCs than in SGNs. This confirms the hypothesis that disruption of SGN activity plays a role in the decrease in firing rates in SBCs. Since multiple SGN inputs need to arrive to SBCs within a short time window to generate SBC activity, desynchronized SGN activity reduces the probability of SBC firing. Same thing happens for MSO cells as well. Lower SBC activity decreases the chance of binaural excitatory coincidences at the MSO, leading to lower MSO firing rates. However, the relative decrease in MSO firing rates is bigger than the relative decrease in SBC activity. This is due to the desynchronization of SBC activity, leading to even lower chances of coincidences in MSO cells.

Since the difference in MSO firing rates between both hemispheres is critical for the detection of the horizontal angle of sound sources, lower activity levels in both hemispheres decreases this difference, presumably causing binaural processing and sound localization deficits. These results are in line with behavioral human studies, which provided evidence that myelin defects generate problems in locating the sound due to the decrease in ITD sensitivity [65, 99, 100]. This model can be useful to further study the effect of the loss of synapses between inner hair cells and SGNs, which is another mechanism for HHL and is also known to cause speech intelligibility deficits. Comparing the impact of these two mechanisms of HHL (synaptopathy and myelinopathy) on the activity patterns in cochlear nucleus circuits would give us insight into possible treatments for both HHL scenarios to overcome binaural processing deficits.

Chapter V

Conclusion

5.1 Summary

In this dissertation, we investigated the impact of disruption of synaptic transmission on neuronal network structures with computational modeling methods from both a theoretical and an applied perspective. In the theoretical work (Chapter II), we explored spatiotemporal pattern formation on large neuronal networks when synapses are not reliable. In the applied study (Chapters III and IV), we analyzed a specific case which emerges from improper synaptic transmission in peripheral auditory system, called hidden hearing loss (HHL).

Previous studies on consciousness suggested that application of anesthetics leads to loss of coherence in the brain due to the disconnection of the hub structures in the brain networks. To test this hypothesis, we explored the effect of gradual, probabilistic synaptic failure on large, scale-free networks with different directionalities. We provided evidence that disconnecting hubs may lead to the emergence of more coherent activity as a result of homogenized input levels within the networks.

Next, we investigated a particular instance resulting from disrupted signal transmission: HHL. Several in-vivo studies showed that HHL may arise from two distinct mechanisms; loss of inner hair cell-spiral ganglion neuron (IHC-SGN) synapses and disruption of myelination patterns at the heminode of the peripheral SGN axon. In Chapter III, we built a computational model to

simulate the effect of both scenarios on cumulative SGN activity, i.e. compound action potential (CAP). We found that both scenarios decrease the amplitude of CAP, whereas only myelinopathy increases the latency to the CAP peak, due to the desynchronized activity patterns of SGN fibers.

Many behavioral studies on humans indicated that HHL leads to binaural processing and sound localization deficits. To explore the mechanism giving rise to this outcome, we modeled a mammalian MSO circuit, since firing rate of MSO cells play an essential role in sound localization (Chapter IV). MSO cells are driven by the activity of SGN fibers, therefore we used SGN spike times generated by the HHL model explained in Chapter III to activate MSO cells. We showed that increasing the degree of myelinopathy gradually decreases MSO activity. This potentially explains why people with HHL have speech intelligibility deficits.

5.2 Future directions

In this dissertation, we investigated the significance of proper synaptic transmission on the functioning of the brain, and specifically of the auditory system. However, more steps could be taken to elucidate the mechanisms underlying hearing deficits. In Chapter IV, we explored the impact of HHL due to myelinopathy on MSO activity. The possible next step would be studying the effect of synaptopathy on MSO firing rates. Shedding light on the different mechanisms of both scenarios would be helpful to figure out treatments for HHL. Moreover, ITD is not the only cue for binaural sound localization. The location of a high frequency sound can be detected by intensity cues, known as ILD, which means the intensity difference on both ears. Modeling LSO circuits which are sensitive to ILDs and simulating LSO activity for different HHL scenarios would give us more insight into the mechanisms of sound localization deficits of HHL patients.

Besides computational work, experimental studies would be helpful to test our hypothesis that hidden hearing loss due to synaptopathy and myelinopathy might lead to sound localization

deficits. So far, behavioral studies showed that myelin defects, aging or noise exposure may cause binaural processing deficits with no elevation in hearing thresholds in humans [62, 65, 95, 96, 99, 100]. However, they did not test the SGN activity in these people, therefore there is lacking evidence that they have hidden hearing loss. Moreover, these studies cannot explain the source of these problems on sound localization. Thus, animal studies would be beneficial to provide evidence that different hidden hearing loss scenarios lead to sound localization deficits and to identify the underlying mechanisms causing binaural integration problems. Specifically, behavioral studies on gerbils with different hidden hearing loss scenarios could assess the effect of these hidden hearing loss scenarios on sound localization. Moreover, electrophysiological studies on these gerbils could be done to measure the activity of MSO and LSO cells, which would potentially shed light into the source of sound localization problems.

Appendix

This section contains some supplementary figures and text mentioned in Chapters II and III. Supplementary figures for Chapter II (Supp.fig.2.1-2.5) give insights into the network dynamics and pattern formation with varying noise and connectivities for incoming and outgoing networks. Supplementary figures for Chapter III (Supp.fig.3.1-3.4) show the effect of different myelinopathy scenarios or different I_{app} values on the activity of SGN fibers. The details of the model to simulate SGN activity are described in the supplementary text.

Supplementary Material
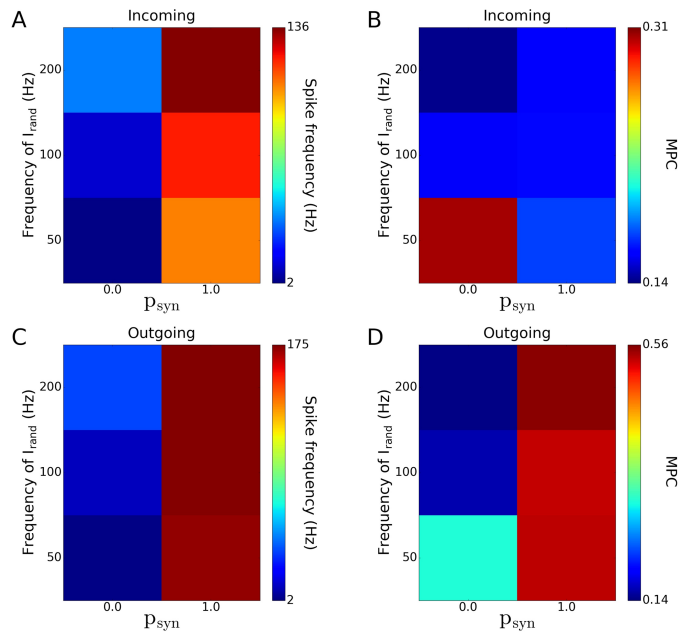
Supplementary Figure 2. 1 Network Spike frequency [(A) and (C)] and mean phase coherence [(B) and (D)] for various frequencies of random input (I_{rand}), for incoming [(A) and (B)] and outgoing [(C) and (D)] networks. Results are averaged over 5 randomized network realizations.
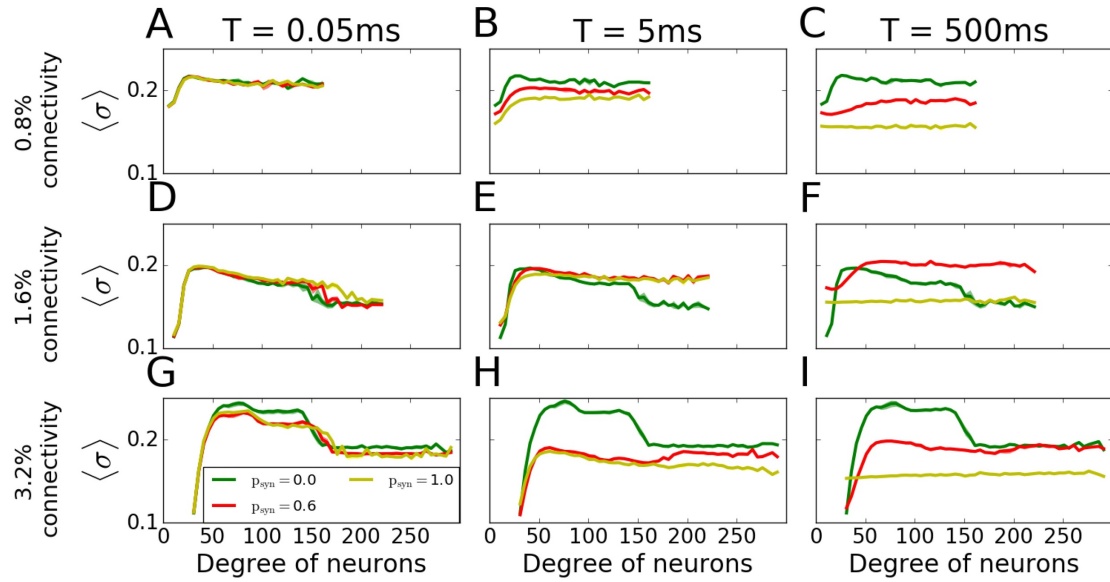
Supplementary Figure 2. 2 Nodal contribution to network-wide Mean Phase Coherence (MPC) as a function of its degree for incoming networks for different connectivities and failure recovery time constant T. The increase in MPC of hubs with higher failure cannot be observed for lower or higher connectivities for T=5ms. MPCs are averaged over 5 degrees and results are averaged over 5 randomized network realizations.
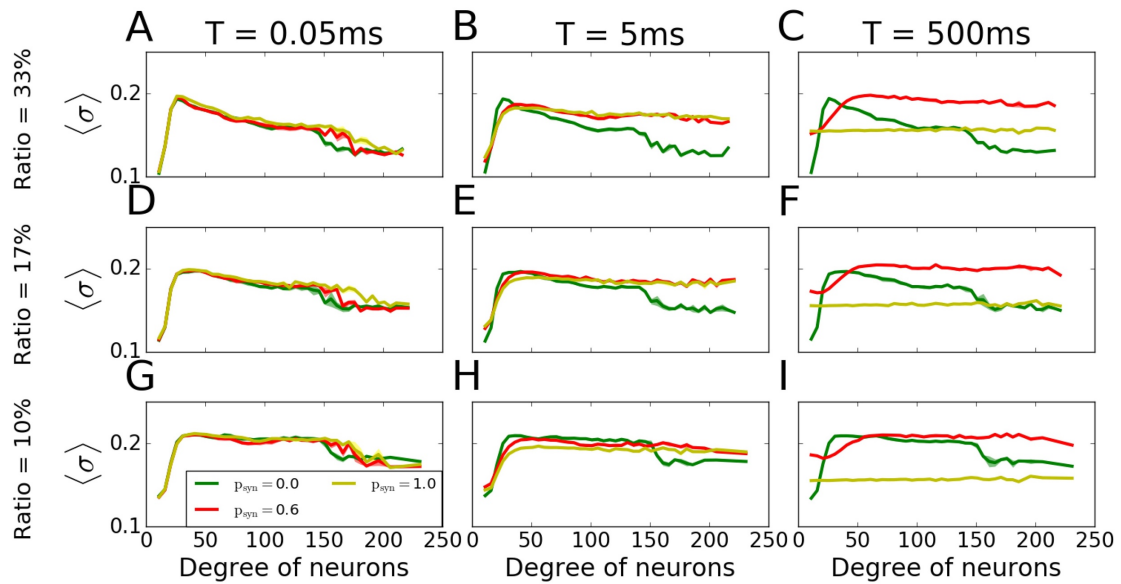
Supplementary Figure 2. 3 Nodal contribution to network-wide Mean Phase Coherence (MPC) as a function of its degree for incoming networks for different direction ratios and failure recovery time constant T. Higher direction ratios result in a more obvious increase in MPC of hubs for T=5ms when there's more failure. MPCs are averaged over 5 degrees and results are averaged over 5 randomized network realizations.
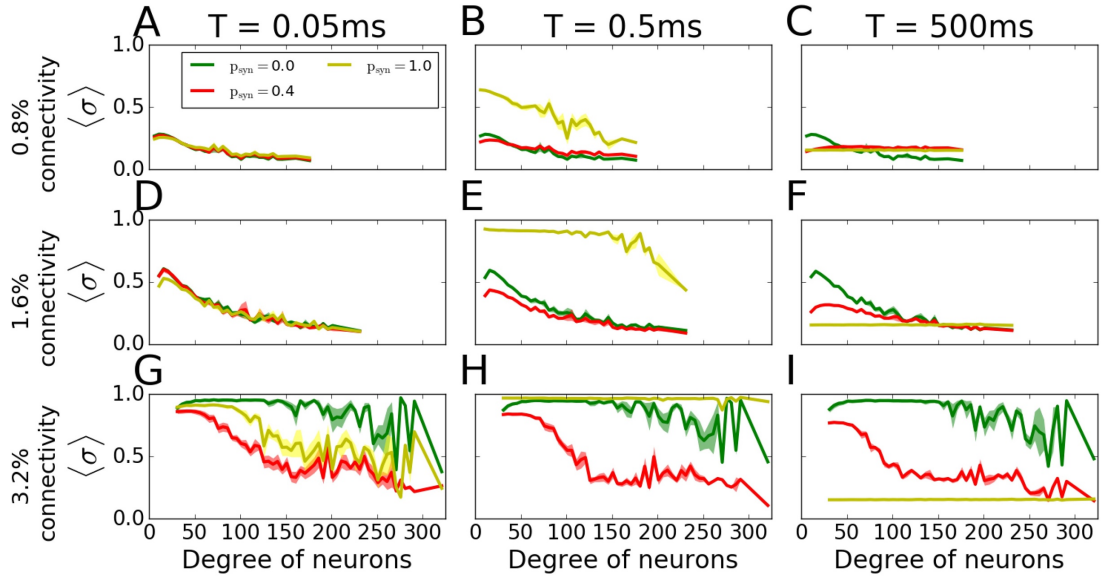
Supplementary Figure 2. 4 Nodal contribution to network-wide Mean Phase Coherence (MPC) as a function of its degree for outgoing networks for different connectivities and failure recovery time constant. Higher connectivities result in a bigger increase in MPC for T=0.5ms with higher failure p_{syn}. MPCs are averaged over 5 degrees and results are averaged over 5 randomized network realizations.

Supplementary Figure 2. 5 Nodal contribution to network-wide Mean Phase Coherence (MPC) as a function of its degree for outgoing networks for different direction ratios and failure recovery time constant T. For T=0.5ms, the increase in MPC values of p_{syn}=1.0 is more pronounced for lower direction ratios. MPCs are averaged over 5 degrees and results are averaged over 5 randomized network realizations.

97

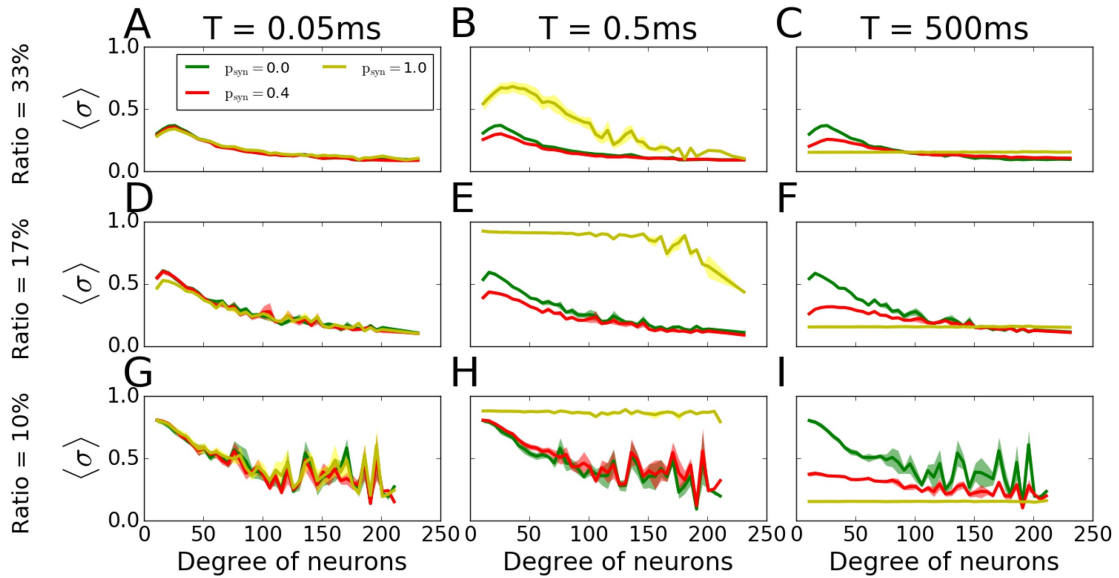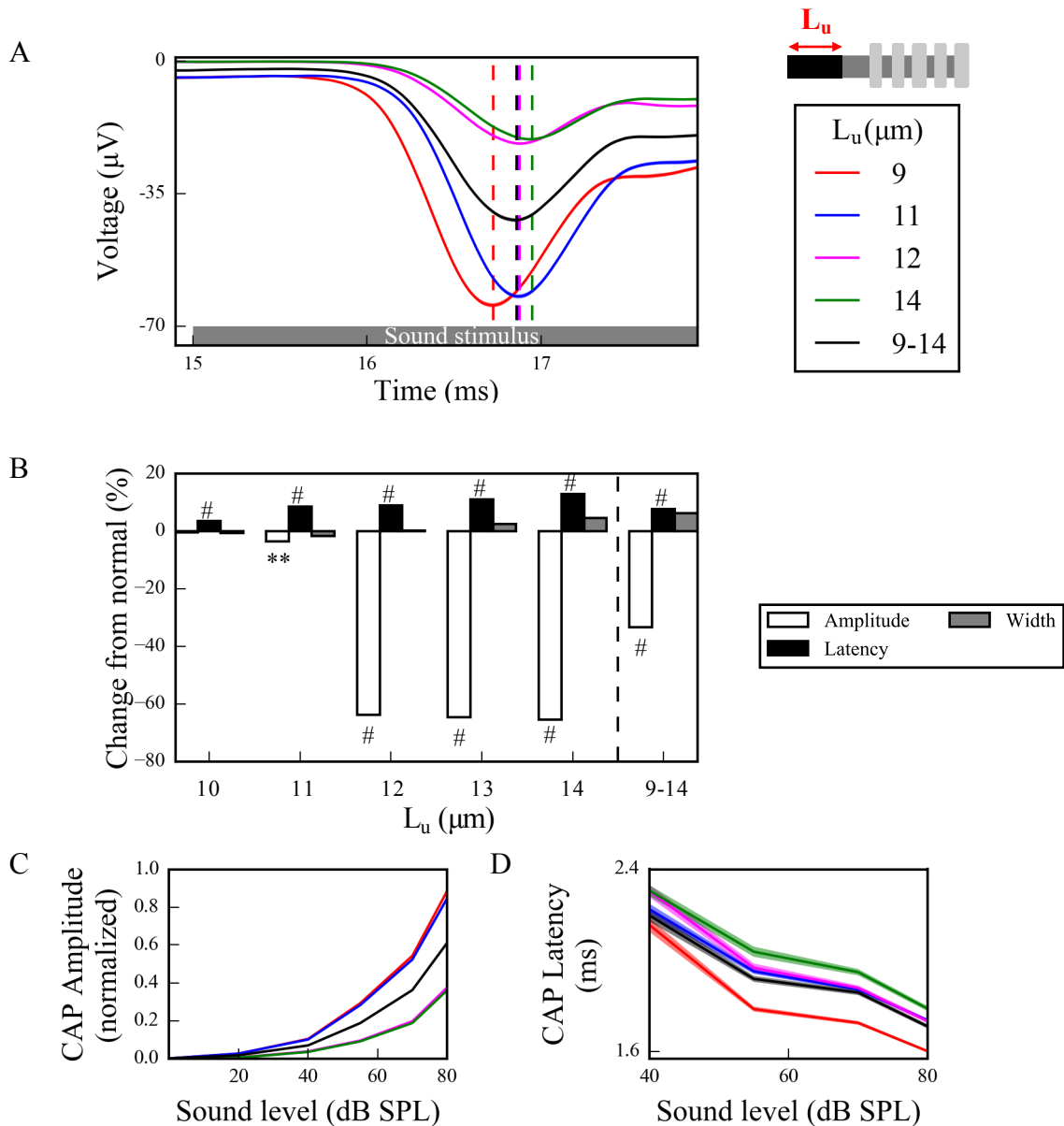**Supplementary Figure 3. 1 Keeping constant channel number as length of unmyelinated segment, L_u, is increased leads to larger effects on cumulative CAP of increased Lu.** (A) Sound-evoked CAPs of SGN fiber populations with varied L_u at 70dB SPL, averaged over 50 simulations (dashed lines correspond to the peaks of each CAP, labeled with the same colors as the CAPs). The number of membrane ionic channels was kept fixed at the values for normal L_u (L_u =10 μm). Decreases in peak amplitude and increases in peak latency are larger for populations with L_u > 12 μm (compare to Fig III.5). (B) Comparison of CAP measures relative to normal L_u (L_u =9 μm) of each population at 70 dB SPL (*p<0.05, **p<0.01, #p<0.001). Normalized CAP amplitudes (C) and CAP latencies (D) for various sound levels, averaged over 50 simulations. Shaded areas correspond to the standard error of the mean.
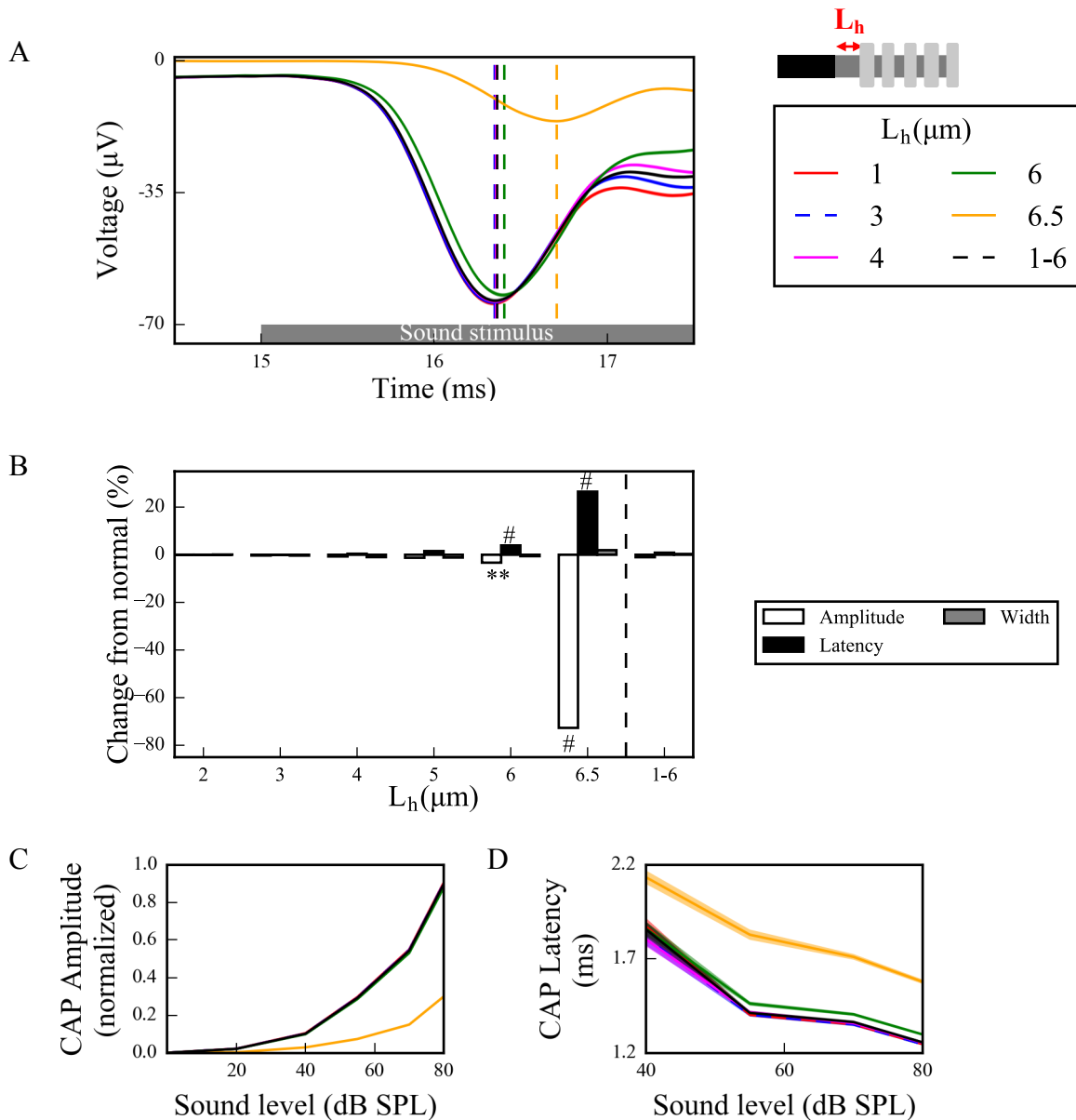
Supplementary Figure 3. 2 Maintaining channel density at the heminode as its length, L_h, is varied reduces effects on cumulative CAP of increased L_h. (A) Sound-evoked CAPs of SGN fiber populations with varied L_h at 70dB SPL, averaged over 50 simulations (dashed lines correspond to the peaks of each CAP, labeled with the same colors as the CAPs). Densities of membrane ionic channels were kept constant at the values for normal L_h (L_h =1 μm). Decreases in amplitude and increases in latency of CAP peaks are more obvious for populations with $L_h > 6$ μm (compare to Fig III.6). (B) Comparison of CAP measures relative to normal L_h (L_h =1 μm) for each population at 70 dB SPL (*p<0.05, **p<0.01, #p<0.001). Normalized CAP amplitudes (C) and CAP latencies (D) for various sound levels, averaged over 50 simulations. Shaded areas correspond to the standard error of the mean.
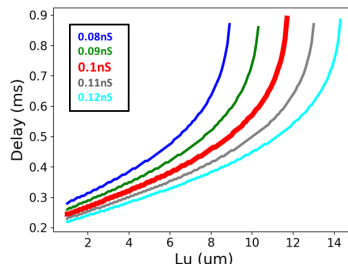
Supplementary Figure 3. 3 The characteristics of I$_{app}$ and the L$_u$ value of SGN fibers determine the time difference between a spike and a release preceding the spike (delay). External current pulses (I$_{app}$) with varying amplitudes are applied to the peripheral end of SGN fibers to simulate a vesicle release event, and the time difference between the release and the resulting spike is calculated for single SGN fibers with varying L$_u$. Red curve represents our default stimulation to simulate release events, unless otherwise stated.
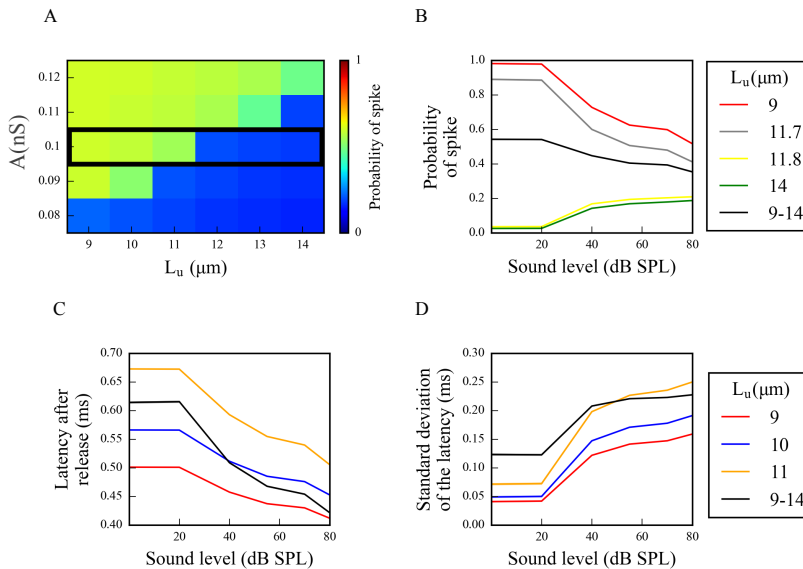
Supplementary Figure 3. 4 Myelinopathy results in a significantly reduced spike probability and increased latency after a release event. (A) The probability that simulated IHC-SGN synaptic vesicle release events result in spike generation at the heminodes of postsynaptic SGN fibers was calculated for various SGN fiber populations at 70dB SPL, averaged over 50 simulations. The amplitude of external current pulses (I$_{app}$) applied at the beginning of L$_u$, representing IHC-SGN vesicle release, was varied between 0.08nS and 0.12nS. The threshold L$_u$, where abrupt drop of spike probability occurs, increases with increasing I$_{app}$. Panels (B)-(D) and all other results in the chapter were obtained with I$_{app}$=0.1nS. (B) Spike probabilities for SGN fiber populations with different homogeneous L$_u$ values in response to different sound levels exhibit an abrupt drop when L$_u$ ≥11.7 μm for all sound levels. (C) The average latency after each release event of spikes across SGN fiber populations, averaged over 50 simulations, increases for longer L$_u$. (D) Standard deviations of spike latencies of SGN fiber populations, averaged over 50 simulations, increase with sound level. The heterogeneous population (9 μm ≤ L$_u$ ≤ 14 μm) has higher standard deviation than homogeneous populations for every sound level. Since fibers with L$_u$ >11 μm do not fire in response to single release events, they are not shown in panels (C) and (D).

100

In Chapter III, for each SGN fiber, the transmembrane potential V_m is a function of space x and time t and is expressed as:

$$-\frac{1}{R_a}\frac{\partial^2 V_m(x,t)}{\partial x^2} + C_m\frac{\partial V_m(x,t)}{\partial t} + \frac{V_m(x,t)-E_{rest}}{R_m} + I_{ion}(x,t) = I_{app}(x,t) \tag{i}$$

where R_a is the specific cytoplasmic resistance, C_m is the specific capacitance, R_m is the specific membrane resistance, E_{rest} is the resting potential, $I_{ion}(x,t)$ and $I_{app}(x,t)$ are ionic and applied currents, respectively.

Ionic current ($I_{ion}(x,t)$) consists of sodium ($I_{Na}(x,t)$) and potassium ($I_K(x,t)$) currents:

$$I_{ion}(x,t) = I_{Na}(x,t) + I_K(x,t) \tag{ii}$$

where,

$$I_{Na}(x,t) = g_{Na}\big(m(t)\big)^3 h(t)(V_m(x,t) - E_{Na}) \tag{iii}$$

and

$$I_K(x,t) = g_K\big(n(t)\big)^4 (V_m(x,t) - E_K) \tag{iv}$$

Here, $m(t)$, $h(t)$ and $n(t)$ are gating variables, g_{Na} and g_K are maximal sodium and potassium conductances, respectively, and E_{Na} and E_K are the Nernst potentials for sodium and potassium ions, respectively. The gating variables i (for $i=m,\ n$ and h) are expressed in terms of rate functions $\alpha_i(V_m)$ and $\beta_i(V_m)$, such that [85]:

$$\frac{di}{dt} = \alpha_i(V_m)(1-i) - \beta_i(V_m)i \quad for\ i = m, n, h \tag{v}$$

where,

$$\alpha_m(V_m) = \frac{1.872(V_m+52.59)}{1-e^{\frac{-(V_m+52.59)}{6.06}}} \tag{vi}$$

$$\beta_m(V_m) = \frac{-3.973(V_m+57)}{1-e^{\frac{V_m+57}{9.41}}} \tag{vii}$$

$$\alpha_h(V_m) = \frac{-0.549(V_m+105.74)}{1-e^{\frac{V_m+105.74}{9.06}}} \tag{viii}$$

101

$$\beta_h(V_m) = \frac{22.57}{1+e^{\frac{-(V_m+22)}{12.5}}} \tag{ix}$$

$$\alpha_n(V_m) = \frac{0.129(V_m+43)}{1-e^{\frac{-(V_m+43)}{10}}} \tag{x}$$

$$\beta_n(V_m) = \frac{-0.324(V_m+68)}{1-e^{\frac{V_m+68}{10}}} \tag{xi}$$

Bibliography

1. Koch C. Cable theory in neurons with active, linearized membranes. Biol Cybern. 1984;50(1):15-33. doi: 10.1007/bf00317936. PubMed PMID: 6324889.

2. Purves D AG, Fitzpatrick D, et al., editors. Neuroscience. 2nd edition. Sunderland (MA): Sinauer Associates, Myelination. ICVaaRo.

3. Bird TD. Charcot-Marie-Tooth (CMT) Hereditary Neuropathy Overview. 1998 Sep 28 [Updated 2020 Jan 2]. In: Adam MP AH, Pagon RA, et al., editors. GeneReviews® [Internet]. Seattle (WA): University of Washington, Seattle. 1993-2020. Available from: https://www-ncbi-nlm-nih-gov.proxy.lib.umich.edu/books/NBK1358/.

4. Donofrio PD. Guillain-Barré Syndrome. Continuum (Minneap Minn). 2017;23(5, Peripheral Nerve and Motor Neuron Disorders):1295-309. doi: 10.1212/CON.0000000000000513. PubMed PMID: 28968363.

5. Hodler J, Kubik-Huch RA, von Schulthess GK, editors. Diseases of the Brain, Head and Neck, Spine 2020–2023: Diagnostic Imaging [Internet]. Cham (CH): Springer, 10.1007/978-3-030-38490-6.

6. Boccaletti S, Latora V, Moreno Y, Chavez M, Hwang D-U. Complex networks: Structure and dynamics. Physics Reports. 2006;424(2006):175-308.

7. van den Heuvel MP, Sporns O. Network hubs in the human brain. Trends Cogn Sci. 2013;17(12):683-96. doi: 10.1016/j.tics.2013.09.012. PubMed PMID: 24231140.

8. Alexander AL, Lee JE, Lazar M, Field AS. Diffusion tensor imaging of the brain. Neurotherapeutics. 2007;4(3):316-29. doi: 10.1016/j.nurt.2007.05.011. PubMed PMID: 17599699; PubMed Central PMCID: PMCPMC2041910.

9. Weissman TA, Pan YA. Brainbow: new resources and emerging biological applications for multicolor genetic labeling and analysis. Genetics. 2015;199(2):293-306. doi: 10.1534/genetics.114.172510. PubMed PMID: 25657347; PubMed Central PMCID: PMCPMC4317644.

10. Gross J, Kujala J, Hamalainen M, Timmermann L, Schnitzler A, Salmelin R. Dynamic imaging of coherent sources: Studying neural interactions in the human brain. Proc Natl Acad Sci U S A. 2001;98(2):694-9. doi: 10.1073/pnas.98.2.694. PubMed PMID: 11209067; PubMed Central PMCID: PMCPMC14650.

11.   Schnitzler A, Gross J. Normal and pathological oscillatory communication in the brain. Nat Rev Neurosci. 2005;6(4):285-96. doi: 10.1038/nrn1650. PubMed PMID: 15803160.

12.   Büchel C, Coull JT, Friston KJ. The predictive value of changes in effective connectivity for human learning. Science. 1999;283(5407):1538-41. doi: 10.1126/science.283.5407.1538. PubMed PMID: 10066177.

13.   Friston KJ, Frith CD, Liddle PF, Frackowiak RS. Functional connectivity: the principal-component analysis of large (PET) data sets. J Cereb Blood Flow Metab. 1993;13(1):5-14. doi: 10.1038/jcbfm.1993.4. PubMed PMID: 8417010.

14.   Harriger L, van den Heuvel MP, Sporns O. Rich club organization of macaque cerebral cortex and its role in network communication. PLoS One. 2012;7(9):e46497. Epub 2012/09/28. doi: 10.1371/journal.pone.0046497. PubMed PMID: 23029538; PubMed Central PMCID: PMCPMC3460908.

15.   van den Heuvel MP, Kahn RS, Goñi J, Sporns O. High-cost, high-capacity backbone for global brain communication. Proc Natl Acad Sci U S A. 2012;109(28):11372-7. Epub 2012/06/18. doi: 10.1073/pnas.1203593109. PubMed PMID: 22711833; PubMed Central PMCID: PMCPMC3396547.

16.   Tomasi D, Volkow ND. Functional connectivity density mapping. Proc Natl Acad Sci U S A. 2010;107(21):9885-90. Epub 2010/05/10. doi: 10.1073/pnas.1001414107. PubMed PMID: 20457896; PubMed Central PMCID: PMCPMC2906909.

17.   Tomasi D, Volkow ND. Association between functional connectivity hubs and brain networks. Cereb Cortex. 2011;21(9):2003-13. Epub 2011/01/31. doi: 10.1093/cercor/bhq268. PubMed PMID: 21282318; PubMed Central PMCID: PMCPMC3165965.

18.   Li L, Hu X, Preuss TM, Glasser MF, Damen FW, Qiu Y, et al. Mapping putative hubs in human, chimpanzee and rhesus macaque connectomes via diffusion tractography. Neuroimage. 2013;80:462-74. Epub 2013/04/17. doi: 10.1016/j.neuroimage.2013.04.024. PubMed PMID: 23603286; PubMed Central PMCID: PMCPMC3720835.

19.   Nijhuis EH, van Cappellen van Walsum AM, Norris DG. Topographic hub maps of the human structural neocortical network. PLoS One. 2013;8(6):e65511. Epub 2013/06/10. doi: 10.1371/journal.pone.0065511. PubMed PMID: 23935801; PubMed Central PMCID: PMCPMC3677881.

20.   Iturria-Medina Y, Sotero RC, Canales-Rodríguez EJ, Alemán-Gómez Y, Melie-García L. Studying the human brain anatomical network via diffusion-weighted MRI and Graph Theory. Neuroimage. 2008;40(3):1064-76. Epub 2007/11/19. doi: 10.1016/j.neuroimage.2007.10.060. PubMed PMID: 18272400.

21.   Gong G, He Y, Concha L, Lebel C, Gross DW, Evans AC, et al. Mapping anatomical connectivity patterns of human cerebral cortex using in vivo diffusion tensor imaging tractography. Cereb Cortex. 2009;19(3):524-36. Epub 2008/06/20. doi: 10.1093/cercor/bhn102. PubMed PMID: 18567609; PubMed Central PMCID: PMCPMC2722790.

22. Markov NT, Ercsey-Ravasz MM, Ribeiro Gomes AR, Lamy C, Magrou L, Vezoli J, et al. A weighted and directed interareal connectivity matrix for macaque cerebral cortex. Cereb Cortex. 2014;24(1):17-36. Epub 2012/09/25. doi: 10.1093/cercor/bhs270. PubMed PMID: 23010748; PubMed Central PMCID: PMCPMC3862262.

23. Yan C, He Y. Driving and driven architectures of directed small-world human brain functional networks. PLoS One. 2011;6(8):e23460. Epub 2011/08/12. doi: 10.1371/journal.pone.0023460. PubMed PMID: 21858129; PubMed Central PMCID: PMCPMC3155571.

24. Bullmore E, Sporns O. Complex brain networks: graph theoretical analysis of structural and functional systems. Nat Rev Neurosci. 2009;10(3):186-98. Epub 2009/02/04. doi: 10.1038/nrn2575. PubMed PMID: 19190637.

25. van den Heuvel MP, Stam CJ, Boersma M, Hulshoff Pol HE. Small-world and scale-free organization of voxel-based resting-state functional connectivity in the human brain. Neuroimage. 2008;43(3):528-39. Epub 2008/08/22. doi: 10.1016/j.neuroimage.2008.08.010. PubMed PMID: 18786642.

26. Eguíluz VM, Chialvo DR, Cecchi GA, Baliki M, Apkarian AV. Scale-free brain functional networks. Phys Rev Lett. 2005;94(1):018102. Epub 2005/01/06. doi: 10.1103/PhysRevLett.94.018102. PubMed PMID: 15698136.

27. Bassett DS, Bullmore ET. Human brain networks in health and disease. Curr Opin Neurol. 2009;22(4):340-7. doi: 10.1097/WCO.0b013e32832d93dd. PubMed PMID: 19494774; PubMed Central PMCID: PMCPMC2902726.

28. Bassett DS, Bullmore E, Verchinski BA, Mattay VS, Weinberger DR, Meyer-Lindenberg A. Hierarchical organization of human cortical networks in health and schizophrenia. J Neurosci. 2008;28(37):9239-48. doi: 10.1523/JNEUROSCI.1929-08.2008. PubMed PMID: 18784304; PubMed Central PMCID: PMCPMC2878961.

29. van den Heuvel MP, Mandl RC, Stam CJ, Kahn RS, Hulshoff Pol HE. Aberrant frontal and temporal complex network structure in schizophrenia: a graph theoretical analysis. J Neurosci. 2010;30(47):15915-26. doi: 10.1523/JNEUROSCI.2874-10.2010. PubMed PMID: 21106830; PubMed Central PMCID: PMCPMC6633761.

30. Buckner RL, Sepulcre J, Talukdar T, Krienen FM, Liu H, Hedden T, et al. Cortical hubs revealed by intrinsic functional connectivity: mapping, assessment of stability, and relation to Alzheimer's disease. J Neurosci. 2009;29(6):1860-73. doi: 10.1523/JNEUROSCI.5062-08.2009. PubMed PMID: 19211893; PubMed Central PMCID: PMCPMC2750039.

31. Seeley WW, Crawford RK, Zhou J, Miller BL, Greicius MD. Neurodegenerative diseases target large-scale human brain networks. Neuron. 2009;62(1):42-52. doi: 10.1016/j.neuron.2009.03.024. PubMed PMID: 19376066; PubMed Central PMCID: PMCPMC2691647.

32. Shi F, Wang L, Peng Z, Wee CY, Shen D. Altered modular organization of structural cortical networks in children with autism. PLoS One. 2013;8(5):e63131. Epub 2013/05/10. doi: 10.1371/journal.pone.0063131. PubMed PMID: 23675456; PubMed Central PMCID: PMCPMC3651174.

33. Supekar K, Menon V, Rubin D, Musen M, Greicius MD. Network analysis of intrinsic functional brain connectivity in Alzheimer's disease. PLoS Comput Biol. 2008;4(6):e1000100. Epub 2008/06/27. doi: 10.1371/journal.pcbi.1000100. PubMed PMID: 18584043; PubMed Central PMCID: PMCPMC2435273.

34. Agosta F, Sala S, Valsasina P, Meani A, Canu E, Magnani G, et al. Brain network connectivity assessed using graph theory in frontotemporal dementia. Neurology. 2013;81(2):134-43. Epub 2013/05/29. doi: 10.1212/WNL.0b013e31829a33f8. PubMed PMID: 23719145.

35. Chen Y, Fu AKY, Ip NY. Synaptic dysfunction in Alzheimer's disease: Mechanisms and therapeutic strategies. Pharmacol Ther. 2019;195:186-98. Epub 2018/11/12. doi: 10.1016/j.pharmthera.2018.11.006. PubMed PMID: 30439458.

36. Franks NP. General anaesthesia: from molecular targets to neuronal pathways of sleep and arousal. Nat Rev Neurosci. 2008;9(5):370-86. doi: 10.1038/nrn2372. PubMed PMID: 18425091.

37. Wishart TM, Parson SH, Gillingwater TH. Synaptic vulnerability in neurodegenerative disease. J Neuropathol Exp Neurol. 2006;65(8):733-9. doi: 10.1097/01.jnen.0000228202.35163.c4. PubMed PMID: 16896307.

38. Bero AW, Yan P, Roh JH, Cirrito JR, Stewart FR, Raichle ME, et al. Neuronal activity regulates the regional vulnerability to amyloid-β deposition. Nat Neurosci. 2011;14(6):750-6. Epub 2011/05/01. doi: 10.1038/nn.2801. PubMed PMID: 21532579; PubMed Central PMCID: PMCPMC3102784.

39. de Haan W, Mott K, van Straaten EC, Scheltens P, Stam CJ. Activity dependent degeneration explains hub vulnerability in Alzheimer's disease. PLoS Comput Biol. 2012;8(8):e1002582. Epub 2012/08/16. doi: 10.1371/journal.pcbi.1002582. PubMed PMID: 22915996; PubMed Central PMCID: PMCPMC3420961.

40. Diao S, Ni J, Shi X, Liu P, Xia W. Mechanisms of action of general anesthetics. Front Biosci (Landmark Ed). 2014;19:747-57. Epub 2014/01/01. doi: 10.2741/4241. PubMed PMID: 24389218.

41. Lee H, Mashour GA, Noh GJ, Kim S, Lee U. Reconfiguration of network hub structure after propofol-induced unconsciousness. Anesthesiology. 2013;119(6):1347-59. doi: 10.1097/ALN.0b013e3182a8ec8c. PubMed PMID: 24013572; PubMed Central PMCID: PMCPMC3873632.

42. Moon JY, Lee U, Blain-Moraes S, Mashour GA. General relationship of global topology, local dynamics, and directionality in large-scale brain networks. PLoS Comput Biol. 2015;11(4):e1004225. Epub 2015/04/14. doi: 10.1371/journal.pcbi.1004225. PubMed PMID: 25874700; PubMed Central PMCID: PMCPMC4397097.

43. Furman AC, Kujawa SG, Liberman MC. Noise-induced cochlear neuropathy is selective for fibers with low spontaneous rates. J Neurophysiol. 2013;110(3):577-86. Epub 2013/04/17. doi: 10.1152/jn.00164.2013. PubMed PMID: 23596328; PubMed Central PMCID: PMCPMC3742994.

44.   Liberman LD, Suzuki J, Liberman MC. Dynamics of cochlear synaptopathy after acoustic overexposure. J Assoc Res Otolaryngol. 2015;16(2):205-19. Epub 2015/02/13. doi: 10.1007/s10162-015-0510-3. PubMed PMID: 25676132; PubMed Central PMCID: PMCPMC4368657.

45.   Sergeyenko Y, Lall K, Liberman MC, Kujawa SG. Age-related cochlear synaptopathy: an early-onset contributor to auditory functional decline. J Neurosci. 2013;33(34):13686-94. doi: 10.1523/JNEUROSCI.1783-13.2013. PubMed PMID: 23966690; PubMed Central PMCID: PMCPMC3755715.

46.   Heffner HE, Heffner RS. Hearing ranges of laboratory animals. J Am Assoc Lab Anim Sci. 2007;46(1):20-2. PubMed PMID: 17203911.

47.   Kandel ER, Schwartz JH, Jessell TM. Principles of Neural Science. New York: McGraw-Hill Companies; 2000.

48.   Heimer L. (1983) Auditory System. In: The Human Brain and Spinal Cord. Springer NY, NY.

49.   Jia S, Dallos P, He DZ. Mechanoelectric transduction of adult inner hair cells. J Neurosci. 2007;27(5):1006-14. doi: 10.1523/JNEUROSCI.5452-06.2007. PubMed PMID: 17267554; PubMed Central PMCID: PMCPMC6673181.

50.   Mann ZF, Kelley MW. Development of tonotopy in the auditory periphery. Hear Res. 2011;276(1-2):2-15. Epub 2011/01/27. doi: 10.1016/j.heares.2011.01.011. PubMed PMID: 21276841.

51.   Augustine GJ, Charlton MP, Smith SJ. Calcium entry and transmitter release at voltage-clamped nerve terminals of squid. J Physiol. 1985;367:163-81. doi: 10.1113/jphysiol.1985.sp015819. PubMed PMID: 2865362; PubMed Central PMCID: PMCPMC1193058.

52.   Sumner CJ, Lopez-Poveda EA, O'Mard LP, Meddis R. A revised model of the inner-hair cell and auditory-nerve complex. J Acoust Soc Am. 2002;111(5 Pt 1):2178-88. doi: 10.1121/1.1453451. PubMed PMID: 12051437.

53.   Winter IM, Robertson D, Yates GK. Diversity of characteristic frequency rate-intensity functions in guinea pig auditory nerve fibres. Hear Res. 1990;45(3):191-202. PubMed PMID: 2358413.

54.   Joris PX, Carney LH, Smith PH, Yin TC. Enhancement of neural synchronization in the anteroventral cochlear nucleus. I. Responses to tones at the characteristic frequency. J Neurophysiol. 1994;71(3):1022-36. doi: 10.1152/jn.1994.71.3.1022. PubMed PMID: 8201399.

55.   Middlebrooks JC. Sound localization. Handb Clin Neurol. 2015;129:99-116. doi: 10.1016/B978-0-444-62630-1.00006-8. PubMed PMID: 25726265.

56.   Yin TC, Chan JC. Interaural time sensitivity in medial superior olive of cat. J Neurophysiol. 1990;64(2):465-88. doi: 10.1152/jn.1990.64.2.465. PubMed PMID: 2213127.

57.   Scott LL, Mathews PJ, Golding NL. Posthearing developmental refinement of temporal processing in principal neurons of the medial superior olive. J Neurosci. 2005;25(35):7887-95. doi: 10.1523/JNEUROSCI.1016-05.2005. PubMed PMID: 16135745; PubMed Central PMCID: PMCPMC6725447.

58.   Harper NS, McAlpine D. Optimal neural population coding of an auditory spatial cue. Nature. 2004;430(7000):682-6. doi: 10.1038/nature02768. PubMed PMID: 15295602.

59.   Kohrman DC, Wan G, Cassinotti L, Corfas G. Hidden Hearing Loss: A Disorder with Multiple Etiologies and Mechanisms. Cold Spring Harb Perspect Med. 2019. Epub 2019/01/07. doi: 10.1101/cshperspect.a035493. PubMed PMID: 30617057.

60.   Kujawa SG, Liberman MC. Adding insult to injury: cochlear nerve degeneration after "temporary" noise-induced hearing loss. J Neurosci. 2009;29(45):14077-85. doi: 10.1523/JNEUROSCI.2845-09.2009. PubMed PMID: 19906956; PubMed Central PMCID: PMCPMC2812055.

61.   Wan G, Corfas G. Transient auditory nerve demyelination as a new mechanism for hidden hearing loss. Nat Commun. 2017;8:14487. Epub 2017/02/17. doi: 10.1038/ncomms14487. PubMed PMID: 28211470; PubMed Central PMCID: PMCPMC5321746.

62.   Rajan R, Cainer KE. Ageing without hearing loss or cognitive impairment causes a decrease in speech intelligibility only in informational maskers. Neuroscience. 2008;154(2):784-95. Epub 2008/04/04. doi: 10.1016/j.neuroscience.2008.03.067. PubMed PMID: 18485606.

63.   Long P, Wan G, Roberts MT, Corfas G. Myelin development, plasticity, and pathology in the auditory system. Dev Neurobiol. 2018;78(2):80-92. Epub 2017/09/26. doi: 10.1002/dneu.22538. PubMed PMID: 28925106; PubMed Central PMCID: PMCPMC5773349.

64.   Takazawa T, Ikeda K, Murata K, Kawase Y, Hirayama T, Ohtsu M, et al. Sudden deafness and facial diplegia in Guillain-Barré Syndrome: radiological depiction of facial and acoustic nerve lesions. Intern Med. 2012;51(17):2433-7. Epub 2012/09/01. PubMed PMID: 22975563.

65.   Choi JE, Seok JM, Ahn J, Ji YS, Lee KM, Hong SH, et al. Hidden hearing loss in patients with Charcot-Marie-Tooth disease type 1A. Sci Rep. 2018;8(1):10335. Epub 2018/07/09. doi: 10.1038/s41598-018-28501-y. PubMed PMID: 29985472; PubMed Central PMCID: PMCPMC6037750.

66.   DeFriez CB, Wong HC. Seizures and opisthotonos after propofol anesthesia. Anesth Analg. 1992;75(4):630-2. doi: 10.1213/00000539-199210000-00030. PubMed PMID: 1530178.

67.   Voss LJ, Sleigh JW, Barnard JP, Kirsch HE. The howling cortex: seizures and general anesthetic drugs. Anesth Analg. 2008;107(5):1689-703. doi: 10.1213/ane.0b013e3181852595. PubMed PMID: 18931234.

68.   Budak M, Zochowski M. Synaptic Failure Differentially Affects Pattern Formation in Heterogenous Networks. Front Neural Circuits. 2019;13:31. Epub 2019/05/08. doi: 10.3389/fncir.2019.00031. PubMed PMID: 31139055; PubMed Central PMCID: PMCPMC6519395.

69.   Albert-László Barabási RA, Hawoong Jeong. Mean-field theory for scale-free random networks. Physica A: Statistical Mechanics and its Applications1999. p. 173-87.

70. Burkitt AN. A review of the integrate-and-fire neuron model: II. Inhomogeneous synaptic input and network properties. Biol Cybern. 2006;95(2):97-112. Epub 2006/07/05. doi: 10.1007/s00422-006-0082-8. PubMed PMID: 16821035.

71. Mormann F, Lehnertz K, David P, Elger CE. Mean phase coherence as a measure for phase synchronization and its application to the EEG of epilepsy patients. Physica D: Nonlinear Phenomena,2000. p. 358-69.

72. Golomb D, Rinzel J. Dynamics of globally coupled inhibitory neurons with heterogeneity. Phys Rev E Stat Phys Plasmas Fluids Relat Interdiscip Topics. 1993;48(6):4810-4. doi: 10.1103/physreve.48.4810. PubMed PMID: 9961165.

73. Dinamarca MC, Ríos JA, Inestrosa NC. Postsynaptic Receptors for Amyloid-β Oligomers as Mediators of Neuronal Damage in Alzheimer's Disease. Front Physiol. 2012;3:464. Epub 2012/12/20. doi: 10.3389/fphys.2012.00464. PubMed PMID: 23267328; PubMed Central PMCID: PMCPMC3526732.

74. Xu Y, Yan J, Zhou P, Li J, Gao H, Xia Y, et al. Neurotransmitter receptors and cognitive dysfunction in Alzheimer's disease and Parkinson's disease. Prog Neurobiol. 2012;97(1):1-13. Epub 2012/02/25. doi: 10.1016/j.pneurobio.2012.02.002. PubMed PMID: 22387368; PubMed Central PMCID: PMCPMC3371373.

75. Rosenmund C, Mansour M. Ion channels: how to be desensitized. Nature. 2002;417(6886):238-9. doi: 10.1038/417238a. PubMed PMID: 12015586.

76. Papke D, Gonzalez-Gutierrez G, Grosman C. Desensitization of neurotransmitter-gated ion channels during high-frequency stimulation: a comparative study of Cys-loop, AMPA and purinergic receptors. J Physiol. 2011;589(Pt 7):1571-85. Epub 2011/02/07. doi: 10.1113/jphysiol.2010.203315. PubMed PMID: 21300749; PubMed Central PMCID: PMCPMC3099016.

77. van Vreeswijk C, Sompolinsky H. Chaos in neuronal networks with balanced excitatory and inhibitory activity. Science. 1996;274(5293):1724-6. doi: 10.1126/science.274.5293.1724. PubMed PMID: 8939866.

78. Albert R, Jeong H, Barabasi AL. Error and attack tolerance of complex networks. Nature. 2000;406(6794):378-82. doi: 10.1038/35019019. PubMed PMID: 10935628.

79. Chen JLaG. A time-varying complex dynamical network model and its controlled synchronization criteria. *IEEE Transactions on Automatic Control*2005. p. 841-6.

80. Li K, Fu X, Small M, Ma Z. Adaptive mechanism between dynamical synchronization and epidemic behavior on complex networks. Chaos. 2011;21(3):033111. doi: 10.1063/1.3622678. PubMed PMID: 21974646; PubMed Central PMCID: PMCPMC7112447.

81. Kiang NY, Rho JM, Northrop CC, Liberman MC, Ryugo DK. Hair-cell innervation by spiral ganglion cells in adult cats. Science. 1982;217(4555):175-7. PubMed PMID: 7089553.

82.   Hines ML, Carnevale NT. NEURON: a tool for neuroscientists. Neuroscientist. 2001;7(2):123-35. doi: 10.1177/107385840100700207. PubMed PMID: 11496923.

83.   Liberman MC, Oliver ME. Morphometry of intracellularly labeled neurons of the auditory nerve: correlations with functional properties. J Comp Neurol. 1984;223(2):163-76. doi: 10.1002/cne.902230203. PubMed PMID: 6200517.

84.   Woo J, Miller CA, Abbas PJ. The dependence of auditory nerve rate adaptation on electric stimulus parameters, electrode position, and fiber diameter: a computer model study. J Assoc Res Otolaryngol. 2010;11(2):283-96. Epub 2009/12/22. doi: 10.1007/s10162-009-0199-2. PubMed PMID: 20033248; PubMed Central PMCID: PMCPMC2862915.

85.   Mino H, Rubinstein JT, Miller CA, Abbas PJ. Effects of electrode-to-fiber distance on temporal neural response with electrical stimulation. IEEE Trans Biomed Eng. 2004;51(1):13-20. doi: 10.1109/TBME.2003.820383. PubMed PMID: 14723489.

86.   Møller AR, Colletti V, Fiorino FG. Neural conduction velocity of the human auditory nerve: bipolar recordings from the exposed intracranial portion of the eighth nerve during vestibular nerve section. Electroencephalogr Clin Neurophysiol. 1994;92(4):316-20. doi: 10.1016/0168-5597(94)90099-x. PubMed PMID: 7517853.

87.   Woo J, Miller CA, Abbas PJ. Biophysical model of an auditory nerve fiber with a novel adaptation component. IEEE Trans Biomed Eng. 2009;56(9):2177-80. Epub 2009/06/02. doi: 10.1109/TBME.2009.2023978. PubMed PMID: 19497810.

88.   Steadman M. Mark-Steadman/Neural-Representations-Of-Speech: Neural Representations Of Speech (Version v1.1). Geneva: Zenodo2018.

89.   Steadman MA, Sumner CJ. Changes in Neuronal Representations of Consonants in the Ascending Auditory System and Their Role in Speech Recognition. Front Neurosci. 2018;12:671. Epub 2018/10/12. doi: 10.3389/fnins.2018.00671. PubMed PMID: 30369863; PubMed Central PMCID: PMCPMC6194309.

90.   Yi E, Roux I, Glowatzki E. Dendritic HCN channels shape excitatory postsynaptic potentials at the inner hair cell afferent synapse in the mammalian cochlea. J Neurophysiol. 2010;103(5):2532-43. Epub 2010/03/10. doi: 10.1152/jn.00506.2009. PubMed PMID: 20220080; PubMed Central PMCID: PMCPMC2867566.

91.   Louage DH, van der Heijden M, Joris PX. Temporal properties of responses to broadband noise in the auditory nerve. J Neurophysiol. 2004;91(5):2051-65. doi: 10.1152/jn.00816.2003. PubMed PMID: 15069097.

92.   Bourien J, Tang Y, Batrel C, Huet A, Lenoir M, Ladrech S, et al. Contribution of auditory nerve fibers to compound action potential of the auditory nerve. J Neurophysiol. 2014;112(5):1025-39. Epub 2014/05/21. doi: 10.1152/jn.00738.2013. PubMed PMID: 24848461.

93.   Schmiedt RA, Mills JH, Boettcher FA. Age-related loss of activity of auditory-nerve fibers. J Neurophysiol. 1996;76(4):2799-803. doi: 10.1152/jn.1996.76.4.2799. PubMed PMID: 8899648.

94.   Möhrle D, Ni K, Varakina K, Bing D, Lee SC, Zimmermann U, et al. Loss of auditory sensitivity from inner hair cell synaptopathy can be centrally compensated in the young but not old brain. Neurobiol Aging. 2016;44:173-84. Epub 2016/05/10. doi: 10.1016/j.neurobiolaging.2016.05.001. PubMed PMID: 27318145.

95.   Prendergast G, Millman RE, Guest H, Munro KJ, Kluk K, Dewey RS, et al. Effects of noise exposure on young adults with normal audiograms II: Behavioral measures. Hear Res. 2017;356:74-86. Epub 2017/10/25. doi: 10.1016/j.heares.2017.10.007. PubMed PMID: 29126651; PubMed Central PMCID: PMCPMC5714059.

96.   Bernstein LR, Trahiotis C. Behavioral manifestations of audiometrically-defined "slight" or "hidden" hearing loss revealed by measures of binaural detection. J Acoust Soc Am. 2016;140(5):3540. doi: 10.1121/1.4966113. PubMed PMID: 27908080.

97.   Bharadwaj HM, Masud S, Mehraei G, Verhulst S, Shinn-Cunningham BG. Individual differences reveal correlates of hidden hearing deficits. J Neurosci. 2015;35(5):2161-72. doi: 10.1523/JNEUROSCI.3915-14.2015. PubMed PMID: 25653371; PubMed Central PMCID: PMCPMC4402332.

98.   Eddins AC, Ozmeral EJ, Eddins DA. How aging impacts the encoding of binaural cues and the perception of auditory space. Hear Res. 2018;369:79-89. Epub 2018/05/05. doi: 10.1016/j.heares.2018.05.001. PubMed PMID: 29759684; PubMed Central PMCID: PMCPMC6196106.

99.   Furst M, Levine RA. Hearing disorders in multiple sclerosis. Handb Clin Neurol. 2015;129:649-65. doi: 10.1016/B978-0-444-62630-1.00036-6. PubMed PMID: 25726295.

100.   Rance G, Ryan MM, Carew P, Corben LA, Yiu E, Tan J, et al. Binaural speech processing in individuals with auditory neuropathy. Neuroscience. 2012;226:227-35. Epub 2012/09/13. doi: 10.1016/j.neuroscience.2012.08.054. PubMed PMID: 22982232.

101.   Oertel D. Encoding of Timing in the Brain Stem Auditory Nuclei of Vertebrates,. Neuron1997. p. 959-62.

102.   Encke J, Hemmert W. Extraction of Inter-Aural Time Differences Using a Spiking Neuron Network Model of the Medial Superior Olive. Front Neurosci. 2018;12:140. Epub 2018/03/06. doi: 10.3389/fnins.2018.00140. PubMed PMID: 29559886; PubMed Central PMCID: PMCPMC5845713.

103.   Goldberg JM, Brown PB. Response of binaural neurons of dog superior olivary complex to dichotic tonal stimuli: some physiological mechanisms of sound localization. J Neurophysiol. 1969;32(4):613-36. doi: 10.1152/jn.1969.32.4.613. PubMed PMID: 5810617.

104.   Grothe B, Park TJ. Sensitivity to interaural time differences in the medial superior olive of a small mammal, the Mexican free-tailed bat. J Neurosci. 1998;18(16):6608-22. PubMed PMID: 9698347; PubMed Central PMCID: PMCPMC6793185.